

COLD CATHODES FOR APPLICATIONS IN POOR VACUUM AND LOW
PRESSURE GAS ENVIRONMENTS: CARBON NANOTUBES
VERSUS ZINC OXIDE NANONEEDLES

Except where reference is made to the work of others, the work described in this thesis is my own or was done in collaboration with my advisory committee. This thesis does not include proprietary or classified information.

An-jen Cheng

Certificate of Approval:

Richard C. Jaeger
Distinguished University Professor
Electrical and Computer Engineering

Yonhua Tzeng, Chair
Professor
Electrical and Computer Engineering

Minseo Park
Assistant Professor
Physics

Stephen L. McFarland
Acting Dean
Graduate School

COLD CATHODES FOR APPLICATIONS IN POOR VACUUM AND LOW
PRESSURE GAS ENVIRONMENTS: CARBON NANOTUBES
VERSUS ZINC OXIDE NANONEEDLES

An-jen Cheng

A Thesis

Submitted to

the Graduate Faculty of

Auburn University

in Partial Fulfillment of the

Requirement for the

Degree of

Master of Science

Auburn, Alabama
May 11, 2006

COLD CATHODES FOR APPLICATIONS IN POOR VACUUM AND LOW
PRESSURE GAS ENVIRONMENTS: CARBON NANOTUBES
VERSUS ZINC OXIDE NANONEEDLES

An-jen Cheng

Permission is granted to Auburn University to make copies of this thesis at its direction,
upon the request of individuals or institutions and at their expense. The author reserves
all the publication rights

Signature of Author

Date of Graduation

VITA

An-jen Cheng, son of En-Jer Jang (Cheng) and Chin-hua Chen, was born on April 26, 1980, in Tainan, Republic of China, Taiwan. He entered Physics Department, Chun-Yuan Christian University in September, 1999, and graduate with the degree of Bachelor of Science in June, 2003. He entered the graduate program in the Electrical and Computer Engineering Department in Auburn University in January, 2004.

THESIS ABSTRACT

COLD CATHODES FOR APPLICATIONS IN POOR VACUUM AND LOW
PRESSURE GAS ENVIRONMENTS: CARBON NANOTUBES
VERSUS ZINC OXIDE NANONEEDLES

An-jen Cheng

Master of Science, May 11, 2006
(B.S. Chun-Yuan Christian University, R.O.C Taiwan, June 2003)

131 Typed Pages

Directed by Yonhua Tzeng

Effects of gas pressure on the electron field emission (FE) properties of zinc oxide (ZnO) nanoneedles and carbon nanotubes (CNTs) were investigated. The FE properties for ZnO nanoneedles almost fully recovered after being subjected to FE tests in poor vacuum and low pressure gas environments and then characterized again in better vacuum around 1×10^{-6} Torr. In the contrast, the FE properties for CNTs did not recover after being subjected to FE tests in poor vacuum and low pressure gas environments. Reversibility and sensitivity of the FE of ZnO and CNTs to air pressures were studied for potential applications to field emission display (FED) and vacuum microelectronic devices. The pressure-dependent, time-dependent, and pressure-time-dependent field emission behaviors of ZnO nanoneedles and CNTs will be compared and discussed.

ACKNOWLEDGEMENTS

The author would like to extend his deepest thanks to Dr. Yonhua Tzeng for his supervising this thesis and being a great academic advisor during the author's graduate study in Auburn University.

The author would like to express his appreciation to Mr. Yan-Kang Liu, Mr. Chao Liu, Mr. Dake Wang, Ms. Hee Won Seo, Dr. Minseo Park, and Dr. An-Ban Chen for their great help and discussion.

Finally the author would like to thanks his family, especially his mother Chin-hua Chen, for their love, encouragement, dedication, and support.

Style manual or journal used: Bibliography conforms to those of the transactions of the Institute of Electrical and Electronics Engineers

Computer software used: Microsoft Word 2000 for Windows

TABLE OF CONTENTS

LIST OF FIGURES.....	xi
LIST OF TABLES.....	xv
CHAPTER 1 INTRODUCTION.....	1
1.1 Introduction of carbon nanotubes.....	1
1.2 Introduction of a functional oxide-zinc oxide.....	6
1.3 Purpose of research.....	9
CHAPTER 2 LITERATURE REVIEW.....	10
2.1 Structure and material properties of carbon nanotubes.....	10
2.1.1 Basic structure concept of carbon nanotubes.....	10
2.1.2 Electrical properties of carbon nanotube.....	16
2.1.3 Mechanical properties of carbon nanotubes.....	22
2.1.4 Magnetic properties of carbon nanotubes.....	24
2.1.5 Chemical properties of carbon nanotubes.....	25
2.2 Growth techniques of carbon nanotube.....	27
2.2.1 Carbon nanotubes growth by arc discharge.....	27
.....	27
2.2.2 Carbon nanotubes growth by laser ablation.....	32
2.2.3 Carbon nanotubes growth by chemical vapor deposition.....	36
2.2.4 Carbon nanotubes growth mechanisms.....	39

2.3 Structure and material properties of zinc oxide nanostructure.....	43
2.3.1 Structure of ZnO.....	43
2.3.2 Electrical properties of ZnO.....	49
2.3.3 Optical properties of ZnO.....	53
2.3.4 Other properties of ZnO.....	57
2.4 Growth techniques of ZnO.....	59
2.4.1 ZnO synthesis by metal organic chemical vapor deposition.....	59
2.4.2 ZnO synthesis by laser ablation.....	62
2.4.3 ZnO synthesis by vapor transport.....	64
2.5 Field Emission of Electrons from Solid Surface.....	68
2.5.1 Field Emission form metal surface.....	68
2.5.2 Field emission form semiconductor surface.....	70
2.5.3 Field emission form carbon nanotubes.....	72
2.5.4 I-V instabilities and arcing protection.....	75
CHAPTER 3 SPECIMEN PREPARATIONS AND CHARACTERIZATION.....	77
3.1 Growth process.....	77
3.1.1 ZnO nanostructures growth.....	77
3.1.2 Carbon nanotubes growth.....	80
3.2 Electron field emission measurement and setup.....	82
CHAPTER 4 RESULTS AND DISCUSSION.....	85
4.1 Growth of carbon nanotube and its field emission.....	85
4.1.1 Growth and field emission property of multi-walled carbon nanotubes.....	85

4.1.2 Growth and field emission property of single-walled carbon nanotubes.....	88
4.2 Growth of ZnO and its field emission.....	91
4.3 Field emission measurements under diverse pressures.....	97
4.3.1 ZnO nanoneedles field emission measurement under diverse pressures.....	98
4.3.2 SWCNT & MWCNTs field emission measurement under diverse pressures.....	100
4.3.3 Field emission pressure effect of ZnO nanoneedles and CNTs.....	103
4.4.4 Low and high pressure current stability of ZnO and CNTs.....	105
CHAPTER 5 SUMMARY AND FUTURE DIRECTION.....	109
BIBLIOGRAPHY.....	112

LIST OF FIGURES

1.1 Schematic diagram of the formation of a single-walled carbon nanotube. (a) The projection of C_{140} molecule on a hexagonal lattice. (b) A C_{140} molecule. (c) A carbon nanotube one layer in thickness.	2
1.2 Bonding structures of diamond, graphite, nanotubes, and fullerenes: when a graphite sheet is rolled over to form a nanotube, the sp^2 hybrid orbital is deformed for rehybridization of sp^2 toward sp^3 orbital or σ - π bond mixing. This rehybridization structural feature, together with π electron confinement, gives nanotubes unique, extraordinary electronic, mechanical, chemical, thermal, magnetic, and optical properties.	5
2.1 Chiral vectors (n, m) of a carbon nanotube which can be indexed by a planar honeycomb graphite sheet. The location and the length of the lattice vector are used to determine the chirality, electrical properties, and diameter of a nanotube. \mathbf{a}_1 and \mathbf{a}_2 are the real space unit vector of the hexagonal matrix network.....	12
2.2 Since a graphite sheet can be folded in different directions, typically two special genres of nanotubes can be obtained: (1) zigzag $(n, 0)$, and (2) armchair (m, m) , the rest of them are classified as chiral (n, m) nanotubes where $n>m>0$ by definition.....	14
2.3 Schematic of sectional hexagonal lattice network of a graphite sheet with its real space unit vector.....	16
2.4 The two types of orbital are represented by red (orbital 1) and blue (orbital 2) in the schematic diagram above, where one orbital is neighbored by three orbitals of the other type.....	19
2.5 Schematic diagram of the arc discharge apparatus where carbon nanotubes are formed from the plasma between the two black carbon rods. All the arrows indicate for the vacuum and the He lines are water-cooling system.....	29
2.6 Schematic of laser ablation setup for carbon nanotubes growth.....	33
2.7 Schematic of commonly used laser ablation reactor for SWCNTs growth.....	35
2.8 Schematic diagram of a PECVD setup for carbon nanotubes growth.....	38

2.9 Schematic of tip and base carbon nanotubes growth mechanisms. On the left hand side, the nanoparticle is detached from the substrate on the tip of nanotube, catalyzing growth and preventing nanotubes closure. On the right hand side, the nanoparticle remains on the substrate, severing as an initial template for nanotubes nucleation. Figure (a) shows the nanoparticle is saturated by carbon species (b) stage of nanotubes nucleation (c) post-nucleation growth.....	42
2.10 The wurtzite structure model of ZnO. The tetrahedral coordination of Zn-O is shown.....	45
2.11 ((a), (b)) SEM images of the hierarchical ZnO nanowire junction arrays, (c) the growth model of the hierarchical structure.....	47
2.12 Typical growth morphologies of one-dimensional ZnO nanostructures and the corresponding facets.....	48
2.13 (a) Schematic of ZnO nanowire transistor, a single ZnO nanowire is connects to the two electrodes (source and drain) (b) I_{SD} - V_{SD} characteristics at different gate voltages as V_{SD} varies from 0 to 2V. (c) transfer characteristics as V_G varies from -20 V to 20 V at $V_{SD}=2V$ (d) Change of the transfer characteristics of two nanowires grown at the same time but different locations. Nanowire A has a mobility of $80 \text{ cm}^2/Vs$ and carrier concentration $\sim 10^6 \text{ cm}^{-3}$; and nanowire B has a mobility of $22 \text{ cm}^2/Vs$ and carrier concentration $\sim 10^7 \text{ cm}^{-3}$	52
2.14 Schematic illustration of utilizing MOCVD for ZnO growth.....	60
2.15 SEM cross section images of ZnO grown at various growth temperature (a) $T_g \leq 200^\circ C$, (b) $200^\circ C < T_g \leq 260^\circ C$, (c) $260^\circ C < T_g \leq 320^\circ C$ (d) $320^\circ C < T_g \leq 380^\circ C$, and (e) $T_g > 380^\circ C$. The ZnO morphologies grown at those temperature regimes are schematically described.....	61
2.16 Growth model of NAPLD (a) at low substrate temperature (b) at high substrate temperature.....	64
2.17 Schematic of different ZnO nanostructures growth at different temperature zone.....	65
2.18 Schematic of ZnO nanowire growth by VLS process.....	67
2.19 (a) Schematic diagram of the band bending neat the semiconductor surface by strong electric field (b) An internal barrier generated by an internal retarding field.....	71
3.1 Schematic diagram for thermal CVD ZnO nanostructures growth.....	79
3.2 Figure 3.2: Schematic diagram for thermal CVD carbon nanotubes growth.....	81

3.3 Schematic diagram for the field emission measurement setup.....	84
4.1 SEM image crosssectional view of the side wall of multi-walled carbon nanotubes.....	86
4.2 TEM photograph of multi-walled carbon nanotubes on silicon with e-beam evaporation of Ti/Fe/Si metal catalysts. The magnification is 100k.....	87
4.3 Field emission measurement of multi-walled carbon nanotubes.....	88
4.4 (a) Cross section SEM image of SWCNT bundles (b) Top view of SWCNT.....	89
4.5 Field emission measurement of single-walled carbon nanotubes.....	90
4.6 (a) higher resolution of SEM image for ZnO nanoneedles. Image size: 6×6 μm (b) lower resolution of SEM image for ZnO nanoneedles. Image size: 20×20 μm.....	91
4.7 SEM images of ZnO nanostructure grow on Si (111) wafer, (a) is the magnification of 10K (image size 5×5 μm), (b) is the magnification of 20K (image size 2.5×2.5 μm) and (c) is the edge view of the sample with the magnification of 10K (image size 6×6 μm).....	93
4.8 SEM images of ZnO nanostructure grow on Si (100) wafer, (a) is the magnification of 10K (image size 5×5 μm) and (b) is the magnification of 5K (image size 10×10 μm).....	94
4.9 PL spectrum measured at room temperature, (a) is the PL spectrum of Si (111) sample, which shows no green emission and (b) is the PL spectrum of Si (100) sample, which shows strong green emission at 510nm.....	95
4.10 Field emission measurement of ZnO nanoneedles.....	96
4.11 Fowler-Nordheim plot of ZnO.....	96
4.12 I-E curves of field emission of ZnO nanoneedles measurement at varied air pressures: (a) 1×10 ⁻⁶ Torr, with the cross marks (b) 0.5mTorr, with the asterisk marks (c) 3.5 mTorr, with the plus marks, (d) 30mTorr, with the diamond marks (e) 60mTorr, which is the curve that overlapped with curve (d) up to 3V/μm.....	100
4.13 I-E curves of field emission of MWCNTs measurements at varied pressures (a) 1×10 ⁻⁶ Torr, with the cross marks (b) 0.5mTorr, with the asterisk marks (c) 3.5 mTorr, with the plus marks, (d) 30mTorr, with the diamond marks (e) 60mTorr, with the dark circles.....	102

4.14 I-E curves of electron field emission of SWCNTs measured at varied pressures (a) 1×10^{-6} Torr, with the cross marks (b) 0.5mTorr, with the asterisk marks (c) 3.5 mTorr, with the plus marks, (d) 30mTorr, with the diamond marks (e) 60mTorr, with the dark circles.....	102
4.15 I-E curves of field emission measurements for ZnO nanoneedles at low pressure before (a) and after (b) measurements carried out at higher pressures.....	104
4.16 I-E curves of field emission measurements for MWCNTs at low pressure before (a) and after (b) measurements carried out at higher pressures.....	104
4.17 I-E curves for Field emission measurements for SWCNTs at low pressure before (a) and after (b) measurements carried out at high pressures.....	105
4.18 Stability measurements for both MWCNTs and ZnO nanoneedles in vacuum at 1×10^{-6} Torr and a higher pressure at 0.5mTorr at a constant applied electric field of $4V/\mu\text{m}$:(a) MWCNTs stability test in vacuum (b) MWCNTs stability test at 0.5 mTorr (c) ZnO nanoneedles stability test in vacuum (d) ZnO nanoneedles stability test at 0.5 mTorr.....	108

LIST OF TABLES

2.1 Isomers made of carbon.....	11
2.2 Classification of carbon nanotubes.....	14
2.3 Mechanical properties of carbon nanotubes.....	24
2.4 Parameters of the MWCNT arc synthesis with 6-mm diameter anode rods.....	30
2.5 Metals and metal compounds catalysts for SWCNT synthesis (Modified from ref. [82]).....	31
2.6 Physical properties of wurtzite ZnO.....	44
2.7 Electron density and mobility measurement under diverse oxygen pressures.....	49
2.8 Lattice parameter of several epitaxy substrates.....	67
2.9 Emission threshold electric fields for various emitter materials.....	73

CHAPTER 1

INTRODUCTION

1.1 Introduction of carbon nanotubes

Carbon-based nanostructured materials, such as nano-crystalline diamond, fullerenes (by Kroto et al. in 1985) [1], carbon nanotubes (by Iijima in 1991) [2], as well as II-VI metal oxide or III-V compound metal oxide nanostructures have attracted considerable attention due to their unique structural and electrical properties. Carbon nanotubes (CNTs) are quasi-one-dimensional (Q1D) cylindrical structure with a typical diameter ranging from 1 nanometer (nm) to several nanometers and length of up to tens of micrometers, and with properties close to those of an ideal graphite fiber. There are two main factors when the uniqueness of the nanotubes structure is characterized. One is *helicity*, which is defined by symmetry and the tube diameter. Another one is *topology*, which is defined by the uniformity of the tube in each layers through growing process [2]. The change in helicity introduces a significant change in the electric density of states, providing unique electrical characters for the nanotubes. The topology, on the other hand, has a profound effect on physical properties.

Among the carbon nanotubular structures, two categories exist with different appearances, structures, and graphitizations. One is single-walled carbon nanotubes (SWCNTs), the other is multi-walled carbon nanotubes (MWCNTs). It is simple to image

a single-walled carbon nanotube. Ideally, it is suitable to consider it as a perfect graphene sheet, in which a graphene being the same polyaromatic mono-atomic layer made of a hexagonal network of sp^2 hybridized carbon atoms that genuine graphite is built up with, to roll it into a cylinder. The hexagonal rings put in contact join coherently. Then the two ends are closed by two caps. The caps are hemi-fullerenes with an appropriate diameter (Figure 1.1). The number of cylindrical layers could be more than one; hence forming so called multi-walled carbon nanotubes.

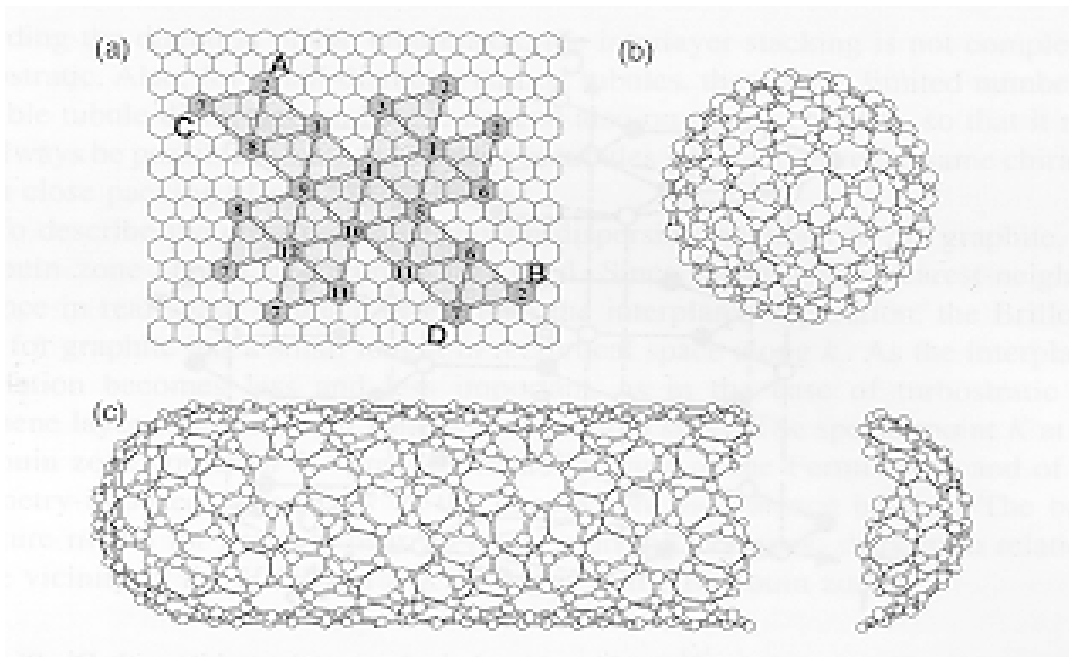


Figure 1.1: Schematic diagram of the formation of a single-walled carbon nanotube. (a) The projection of C_{140} molecule on a hexagonal lattice. (b) A C_{140} molecule. (c) A carbon nanotube one layer in thickness. [3]

The ideal structure of CNTs, in terms of bonding of carbon atoms (sp^2) and hybridization of orbital, is essentially graphitic (Figure 1.2). The feature of this structure is an inside hollow tubular surrounded by the basal plane(s) (002) of graphite, which curved symmetrically geometry and remaining parallel to the tube axis. The formation of the tubular morphology of CNTs is that the free energy of the basal plane in graphite is exceptionally low and stable. The free energy required for nanotubes growth is minimized when the outer surface is a curved basal plane rather than precipitated a highly strained prismatic plane.

However, the circular curvature of CNT causes quantum confinement and σ - π rehybridization in which three σ bonds are slightly out of the plane; for compensation, the π orbital is more delocalized outside the tube. This makes nanotubes mechanically stronger, electrically and thermally more conductive, and chemically and biologically more active than graphite. In addition, they allow topological defects such as pentagons and heptagons to be incorporated into the hexagonal network to form capped, bent, toroidal and helical nanotubes, whereas electrons can be localized in pentagons and heptagons because of the redistribution of π electrons. Theoretically, a nanotubes is defect free if it is of a perfect hexagonal network and defective if it contains topological defects such as pentagon and heptagon or other chemical and structural defects [8].

There are several mechanisms for the growth of CNTs; however, the growth mechanism is still a far way from well known. One reason is that the growth conditions allowing carbon filaments to growth are very diverse, which means that related growth mechanisms are many and not controllable. The other reason is that the phenomena are quite fast and instantaneously and it is difficult to be observed in situ. It is generally

agreed that the growth should occur so that the number of dangling bonds is limited, for energetic reasons. The growth method of CNTs is usually assisted or driven by pyrolyzing hydrocarbon gas mixture, such as acetylene and methane, with selected metal particles serve as catalyst during the growing process.

Several methods for growing CNTs have been achieved, including carbon arc discharge method [4], laser ablation [5], DC-arc plasma jet [6], thermal chemical vapor deposition [7], and plasma-enhanced chemical vapor deposition (PECVD) [8]. Under certain circumstances, bundles of nanotubes with diameters up to 50 μ m are formed with individual nanotubes arranged semi-parallel to each other. The smallest bundle is called a microbundle, which is composed of 10 to 100 nanotubes [3].

Carbon nanotubes exhibit outstanding electrical, mechanical, and chemical properties. They have great potential in small device applications since their dimensions have been shrunken down to nanometer scale region, which cause quantum confinement and unusual physical and electrical phenomena. Carbon nanotubes possess small radius of curvature that allows electrons to be extracted into vacuum by a relatively low external electric field, which makes them suitable for applications such as field emission flat panel display (FED), etc... Moreover, CNTs have fairly low turn-on electric field and high current density, which is mainly due to the high field enhancement factor (β) caused by their extreme high aspect ratio and small curvature.

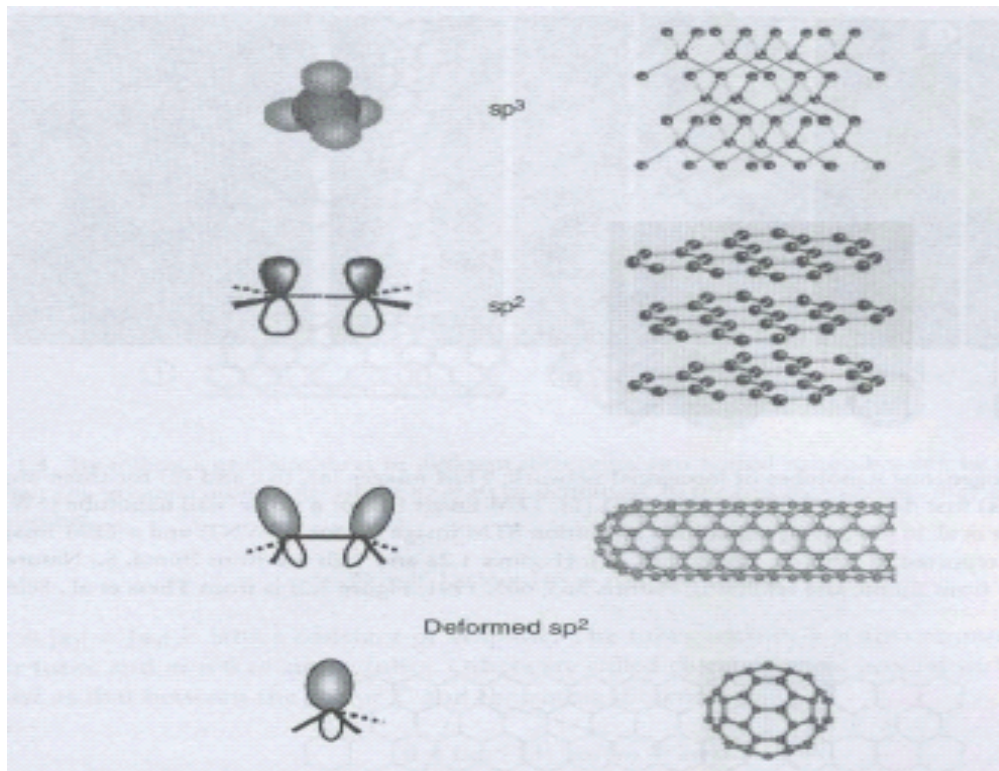


Figure 1.2 Bonding structures of diamond, graphite, nanotubes, and fullerenes: when a graphite sheet is rolled over to form a nanotube, the sp^2 hybrid orbital is deformed for rehybridization of sp^2 toward sp^3 orbital or σ - π bond mixing. This rehybridization structural feature, together with π electron confinement, gives nanotubes unique, extraordinary electronic, mechanical, chemical, thermal, magnetic, and optical properties [8].

1.2 Introduction of a functional oxide-zinc oxide

A widely accepted definition of a nanostructure is that the structure has least one dimension less than 100nm [9], typically including layer-like, wire-like, and particle-like structures. Quantum effects due to the size confinement in nanostructured materials occurs when the characteristic size of the object is comparable with the critical lengths (1-10nm, typically) of the corresponding physical processes, such as mean free path of electrons, the coherence length, or the screening length [9]. Two-dimensional (2D) quantum wells, one-dimensional quantum wires, and zero-dimensional quantum dots are the typical structural forms.

Functional oxides of several novel nanostructures such as nanobelts, nanowires, nanoneedles, nanosheets, and nanohelices are the fundamental of smart devices. Many metal oxide materials such as ZnO, SnO₂, In₂O₃, Ga₂O₃ and PbO₂ have been investigated and synthesized. Zinc oxide (ZnO), a key technological material, is the metal oxide that will be focused in this study.

Oxides are the basis of smart and functional materials. Synthesis and potential device applications using functional oxides have attracted great attention due to the physical properties of these oxides can be tuned. Functional oxides have two structural characteristics: cations with mixed valence states, and anions with deficiencies (vacancies) [10]. By adjusting either or both of these characteristics, the electrical, optical, magnetic, and chemical properties can be tuned, giving the possibility of fabricating smart devices. The structures of functional oxides are very diverse and varied, and there are everlasting new phenomena and applications. According to such unique characteristics make oxides

one of the most diverse classes materials, covering various of the application fields such as semiconductor, superconductor, ferroelectrics, and magnetics.

Wurtzite ZnO, a wide bandgap (3.37eV) *II-V* compound semiconductor, has a hexagonal structure. The structure of ZnO can be simply described as a number of alternating planes composed of tetrahedrally coordinated O^{2-} and Zn^{2+} ions, heaped alternatively along the c-axis [11-12]. The tetrahedral coordination in ZnO leads to a non-central symmetric structure, which is one of the most important structural characteristics of wurtzite nanostructured materials. ZnO shows strong electromechanical coupling due to its unique structure, resulting in strong piezoelectric and pyroelectric properties. The other important structure characteristic of ZnO is polar surfaces. The most common polar surface is the basal plane. Finally, ZnO is also a bio-safe and biocompatible material, which can be used for biomedical applications without further coating.

ZnO has attracted intensive research efforts due to its unique properties and versatile applications in transparent electronics, ultraviolet (UV) light emitters, piezoelectric devices, chemical sensors, and spin electronics. Invisible thin film transistors (TFTs) using ZnO as an active channel have achieved much higher field effect mobility than amorphous silicon TFTs [13-15]. These transistors can be widely used for display applications. ZnO has been proposed as a more promising candidate for UV emitting than GaN because of its larger exciton binding energy (60meV). This leads to the reduction of UV lasing threshold and the increment of UV emitting efficiency at room temperature [16].

Geometrical morphology of metal oxide nanostructured materials, a diverse nanostructures have been synthesized basically by chemical vapor deposition, can be

classified into: tubes [2, 17-23], cages [24, 25], cylindrical wires [26-33] and rods [34-36], co-axial and bi-axial cables, ribbons or belts, sheets [37, 38], and diskettes.

The synthetic methods can be generally classified into several categories: (1) vapor-phase growth, which included thermal evaporation, chemical vapor-phase deposition, metal-organic chemical vapor-phase deposition, arc-discharge, laser ablation, etc. (2) solution-phase growth, (3) sol-gel, (4) templated-based methods, etc. Among these methods, thermal evaporation is the most commonly used method in the investigation of oxide nanostructures. Different kinds of nanostructures can be synthesized using thermal evaporation technique by adjusting the processing parameters, such as pressure, growth temperature, carrier and reactant gases flow rate, and substrates.

1.3 Purpose of Research

CNTs show prominent electrical and mechanical properties for many potential applications due to their unique structures and physical dimensions, but several different kinds of ZnO nanostructures also manifest outstanding electrical, mechanical, and optical properties. One of the most potential applications for these kinds of nanostructured materials, regardless of CNTs or ZnO, is the application in field emission flat panel display, which nanostructured materials can serve as the cold cathode field electron emission sources. Due to the small physical dimensions of the nanostructures, electrons can be easily tunneled through the tips of the CNTs and ZnO at a relatively low external electric field into vacuum. Moreover, it is fairly easily and inexpensive for depositing large area CNTs and ZnO nanostructures.

Even though CNT seems to be the most promising candidate for field emission display (FED), because of its high aspect ratio that allows a high field for large electron emission to be carried out[40, 41]. However, the field emission of CNTs undergoes an irreversible degradation under oxygen and air ambient [42, 43]. The degradation of cold cathode emitters demonstrated one of the most important hurdles for realizing the successful commercialization of FEDs [44].

The purpose of this research is to characterize the field emission properties of different as-deposited ZnO nanostructured materials and CNTs. Furthermore, it is to find out an inexpensive, convenient, and well-controlled method for growing CNTs and ZnO nanostructured material as field electron emission sources.

CHAPTER 2

LITERATURE REVIEW

2.1 Structure and Material Properties of Carbon Nanotubes

2.1.1 Structural Concept of Carbon Nanotubes

Carbon nanotube is a new nanostructured material made of carbon atoms with the bond length of 1.42\AA between each adjacent carbon-carbon bonds. The structure of carbon nanotube is the orientation of the six-membered carbon bonds (called hexagonal) in the honeycomb periodic lattice along the axis of the nanotube. One advantage of carbon-based material is related to the many possible configurations of the electronic states of a carbon atom, which is known as the hybridization of atomic orbitals. Each carbon atom has six electrons occupying $1s^2$, $2s^2$, and $2p^2$ atomic orbitals. The $1s^2$ orbital possesses two strongly bounded electrons, which is known as core electrons. The other four electrons occupy in either the $2s^2$, or $2p^2$ orbitals, and these more weakly bonded electrons are called valence electrons. Since the energy difference between the energy level of upper $2p$ orbital and that of lower $2s$ orbital in carbon is relatively small compared to the binding energy of the chemical bonds; therefore, the electric wave functions for these four weakly bounded electrons can be easily mixed with each other. The phenomenon of mixing bounds between $2s$ and $2p$ atomic orbital is so called *hybridization*. Moreover, carbon is the only element in

the periodic table that has isomers from 0 dimensions (0D) to 3 dimensions (3D), as shown in table2.1 [45].

Table 2.1: Isomers made of carbon [45].

Dimension	0-D	1-D	2-D	3-D
isomer	C ₆₀ fullerene	nanotube	Graphite	diamond
		carbyne	fiber	amorphous
hybridization	sp ²	sp ² (sp)	sp ²	sp ³
density(g/cm ³)	1.72	1.2-2.0	2.26	3.515
		2.68-3.13	~2	2-3
bond length (Å)	1.40 (C=C) 1.46(C-C)	1.44(C=C)	1.42(C=C) 1.44(C=C)	1.54(C-C)
Electronic properties	semiconductor E _g =1.9eV	metal or semiconductor	semimetal	insulating E _g =5.47eV

A carbon nanotube can be visualized as rolling a graphene sheet into a hollow cylinder with both ends capping with a half of the carbon fullerene bulky ball. Thus, the structure is in one dimensional with axial symmetry, and, generally, exhibiting a spiral conformation so called *chirality*. Dresselhaus et al. generated a notation of specifying the structure of an individual tube [46]. By Dresselhaus notation, the position of each carbon atom, which is used to construct a single-walled nanotube, can be specified by the chiral vector. A chiral vector, which is generally labeled C_h, joins two equivalent points on the original graphene lattice (Figure 2.1). Chiral vector can be expressed by the real space unit vector **a**₁ and **a**₂, which is the unit cell base vector of the graphite sheet. And $a_1=a_2=\sqrt{3} d_{c-c}$ with indicating the c-c bond length of 0.142nm, typically. The chiral vector and real space unit vector **a**₁ and **a**₂ can be related by:

$$\mathbf{C}_h = n\mathbf{a}_1 + m\mathbf{a}_2, \quad (0 \leq |m| \leq n) \quad (2.1)$$

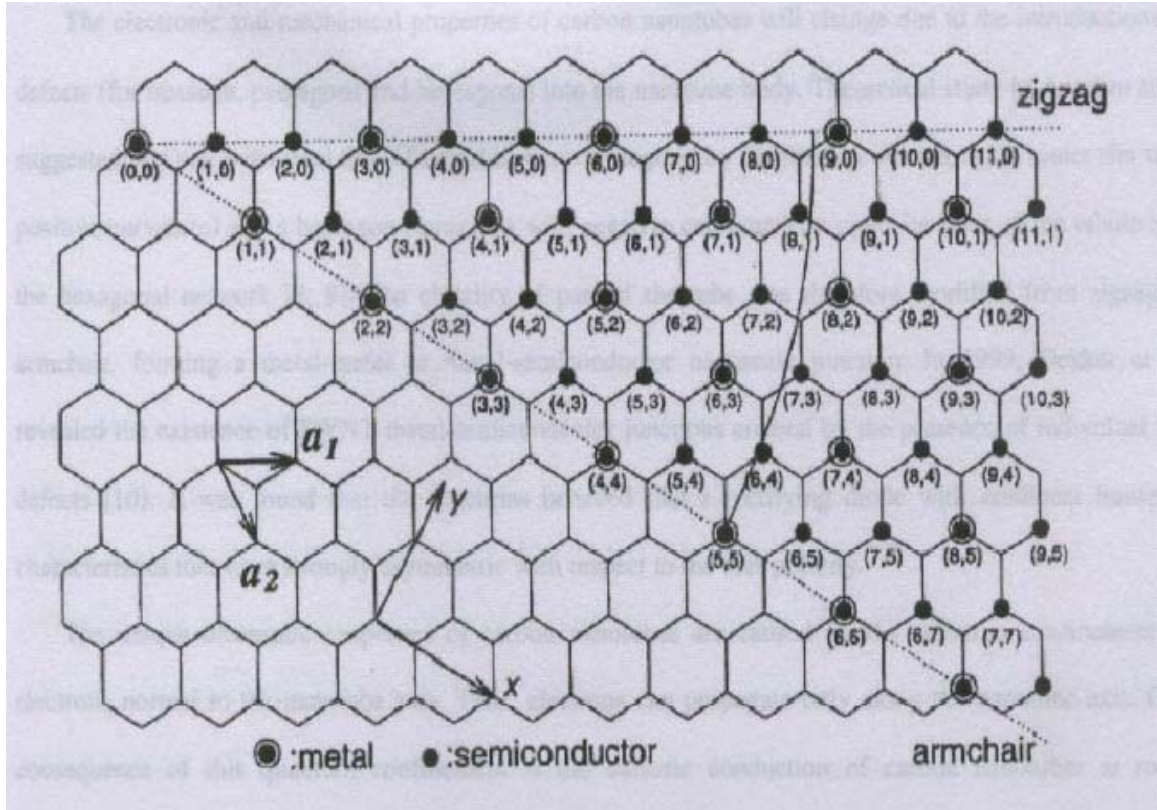


Figure 2.1: Chiral vectors (n, m) of a carbon nanotube which can be indexed by a planar honeycomb graphite sheet. The location and the length of the lattice vector are used to determine the chirality, electrical properties, and diameter of a nanotube. \mathbf{a}_1 and \mathbf{a}_2 are the real space unit vector of the hexagonal matrix network. [3]

The diameter of the carbon nanotube, d_t , is then evaluated by dividing the absolute value of the chiral vector by π ; as:

$$d_t = \frac{a\sqrt{n^2 + m^2 + nm}}{\pi}, \quad a = |\mathbf{a}_1| = |\mathbf{a}_2| = 0.246\text{nm} \quad (2.2)$$

The chiral angle, θ , is defined by the angle between the vectors \mathbf{C}_h and \mathbf{a}_1 with values of θ in the range of $0 \leq |\theta| \leq 30^\circ$. The chiral angle θ is physically expressed as the tilting angle of the

hexagons with respect to the direction of the nanotube axis, and it specifies the spiral symmetry. The chiral angle is expressed as:

$$\theta = \cos^{-1} \frac{2n + m}{2\sqrt{n^2 + m^2 + nm}}, \quad 0 \leq \theta \leq \pi/6 \quad (2.3)$$

Carbon nanotubes can be classified into two groups structure wise, achiral and chiral. An achiral carbon nanotube is defined by a carbon nanotube whose mirror image has an identical structure to the original one. There are two kinds of achiral nanotubes, one is armchair and the other one is zigzag nanotubes. The tubes with $n=m$ are commonly denoted as armchair tubes, and with $m=0$ is implied as zigzag tubes. Chiral nanotubes show spiral symmetry whose mirror image cannot be superposed on to the original one (Figure 2.2) [8]. Table 2.2 is a classification of carbon nanotubes [45].

The lattice constant and intertube spacing are the two main parameters in constructing a SWCNTs, SWCNT bundles, and MWCNTs. These two parameters are also a function of tubes diameter and radial direction. The structural model is of special interest to study the influence of tube chirality (n, m) from simple structural relation to experimentally measurable geometry (D, θ). The chirality (n, m) has many correlations with electric, optical, magnetic, and other properties of a nanotube.

Simply, the spacing between any two coaxial neighboring zigzag tubes ($n, 0$), and ($m, 0$) is $\frac{\Delta D}{2} = (0.123/\pi) (n-m)$ from equation (2.2) and $a=0.246$. Therefore, the spacing between two coaxial MWCNTs cannot be closer than 0.34 nm regardless of value of integer n and m [8]. The most important feature of tube chirality (n, m) is that it is directly related to the electric properties of a nanotube.

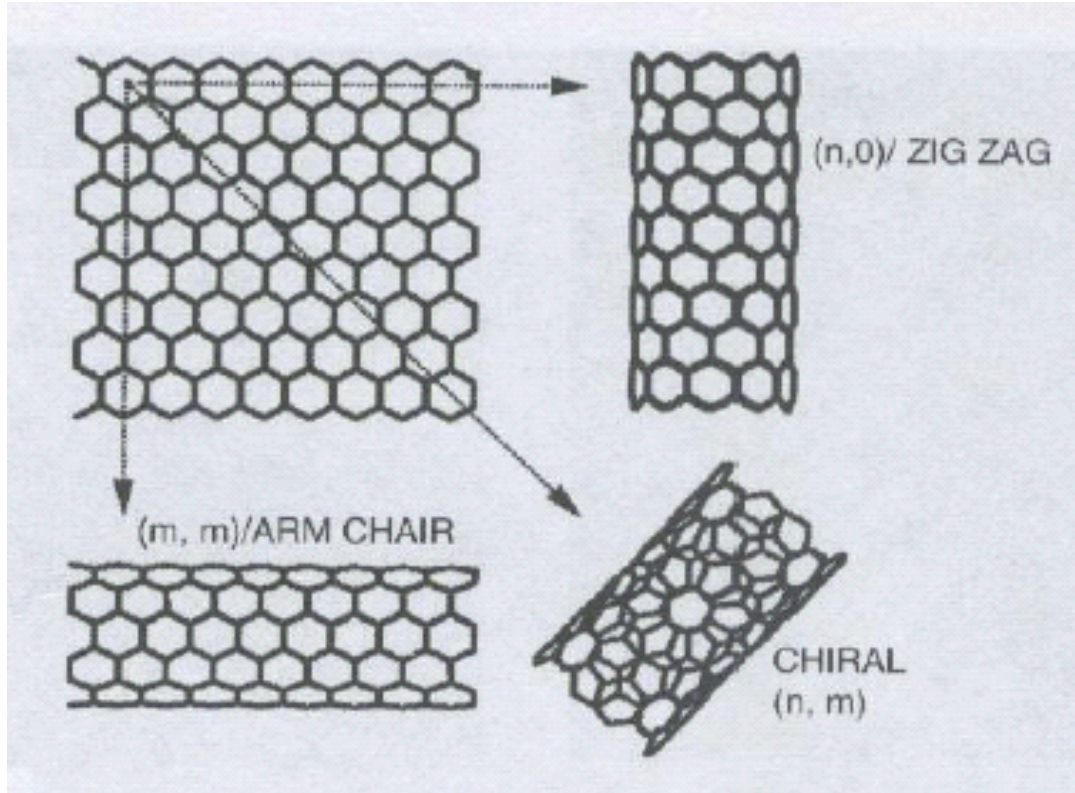


Figure 2.2: Since a graphite sheet can be folded in different directions, typically two special genres of nanotubes can be obtained: (1) zigzag $(n, 0)$, and (2) armchair (m, m) , the rest of them are classified as chiral (n, m) nanotubes where $n > m > 0$ by definition [8].

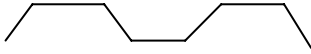
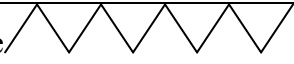
type	θ	C_h	Shape of cross section
armchair	30°	(n, n)	cis-type 
zigzag	0°	$(n, 0)$	Trans-type 
chiral	$0^\circ < \theta < 30^\circ$	(n, m)	Mixture of cis and trans.

Table 2.2: Classification of carbon nanotubes [45]

Experimentally observed carbon nanotubes are defective nanotubes. They often present in capped, bent, branched (L, Y, and T), and helical MWCNTs and SWCNTs form. Most of these defective structures are recognized to have topological defects such as pentagons and heptagons incorporated in the hexagonal matrix of the nanotubes. The pentagon defects are mostly located in the zenith regions of the tips during the formation of fullerene-like caps. The closure of an open cylindrical surface necessarily involves topological defects, at atomic level, that would introduce positive Gaussian curvature. For a nanotube, the surface lattice is composed by a network of six-membered rings. The introduction of positive curvature is achieved by introducing a positive wedged disclination [47, 48], or rings with fewer than six members. In carbon nanotubes, the structural defects are often in pentagonal rings form, and rings with fewer than five members have never been found. The pentagons in the hexagonal lattice can be thought of defects in a sp^2 bonding configuration. A heptagon defect, which produces negative Gaussian curvature, can be created in the hexagonal carbon lattice by introducing a seven-membered ring (-60° disclination) or by cutting and inserting an extra 60° segment into the lattice. The heptagons defects can sometimes be observed, but are destroyed in most tubes what is according to the general restriction of helical arrangement of the hexagonal network [3, 49]. Pentagon-heptagon pairs are believed to be the major topological defects, which are the basic structure for constructing different bending junction of carbon nanotubes conformations [3]. In order to achieve topological enclosure for any single tube, the total number of the pentagons (P) and heptagons (S) should obey the relation of $P=S+12$.

Scanning tunneling microscopy (STM) and Raman spectrum are commonly used in characterizing the tube geometry (d_t, θ), which can be used to calculate (n, m) . In addition, high-resolution transmission electron microscopy (HRTEM) is also used in studying the structures, defects, and arrangement of CNTs in details.

2.1.2 Electrical Properties of Carbon Nanotubes

Electrical transport properties of carbon nanotubes are strongly depended on the chirality and morphology of the nanotubes. A SWCNT is formed by folding a sheet of graphite, which is composed of hexagonal network; therefore, the electrical properties of a SWCNT can be either metallic or semiconducting depending on the angle which the graphite sheet has been folded. Since graphite sheet consists of periodic hexagonal network that the location of each carbon atom can be easily pointed out by utilizing the real space unit vector \mathbf{a}_1 and \mathbf{a}_2 (Figure 2.3). Corresponding to real space unit vector, the reciprocal lattice vector \mathbf{g}_1 and \mathbf{g}_2 can be related as follow:

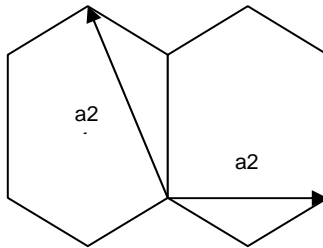


Figure 2.3: Schematic of sectional hexagonal lattice network of a graphite sheet with its real space unit vector.

$$\mathbf{a}_1 = (a, 0), \mathbf{a}_2 = \left(-\frac{1}{2}a, \frac{\sqrt{3}}{2}a\right) \quad (2.4)$$

$$\mathbf{g}_1 = \left(1, \frac{1}{\sqrt{3}}\right) \frac{2\pi}{a}, \mathbf{g}_2 = \left(0, \frac{2}{\sqrt{3}}\right) \frac{2\pi}{a} \quad (2.5)$$

The band structure of carbon nanotubes is usually modeled by a zone folding approximation of the graphene π and π^* electron states obtaining from tight-binding Hamiltonian [50], which is related to chiral vector. Due to the fact that the σ states of the carbon-carbon bonds are fully saturated sp^2 bonds, the main contribution to the valence band and conduction band are from the π -states which are perpendicular to the plane. Therefore, one orbital (π) per atom model can be used to describe the qualitative nature of the band structure.

For a total N unit cells and m atomic orbitals in each cell of a periodic lattice structure the Bloch function χ_j for each atomic orbital j can be written as:

$$\chi_j(k) = \frac{1}{\sqrt{N}} \sum_{l=1}^N e^{ikR_l} \phi_j(R_l) \quad (2.6)$$

where $\phi_j(R_l)$ is the wave function of the atomic orbital j in the l th unit cell. These wave functions that satisfy the Schrödinger equation (2.7) can be written as a linear combination of all m orbitals (2.8).

:

$$\hat{H} \varphi_n(k) = E_n(k) \varphi_n(k) \quad (2.7)$$

$$\varphi_n(k) = \sum_{j=1}^m c_j(k) \chi_j(k) \quad (2.8)$$

As the linear combination of all m orbitals wave functions is substituted into the Schrödinger equation, the equation of (2.7) can be written as:

$$\sum_{j=1}^m c_j(k) \hat{H} \chi_j(k) = E_n(k) \sum_{j=1}^m c_j(k) \chi_j(k) \quad (2.9)$$

Equation (2.9) can also be written in matrix form as:

$$\begin{pmatrix} H_{11} & & & H_{1m} \\ & & & \\ & & & \\ & & & \\ H_{m1} & & & H_{mm} \end{pmatrix} \begin{pmatrix} c_{n1} \\ \\ \\ c_{nm} \end{pmatrix} = E_n \begin{pmatrix} c_{n1} \\ \\ \\ c_{nm} \end{pmatrix} \quad (2.10)$$

where the matrix element $H_{jj'}$ is the Hamiltonian between two orbitals:

$\langle \chi_{j'}(k') | \hat{H} | \chi_j(k) \rangle$, which can also be expressed as:

$$\begin{aligned} H_{jj'} &= \frac{1}{N} \sum_{R_{j'}} \sum_{R_l} e^{-ik'R_{l'}} e^{ikR_l} \int dr \phi_{j'}^*(r - R_{l'}) H(r) \phi_j(r - R_l) \\ &= \delta_{kk'} \sum_{R_l} e^{ik(R_l - R_{l'})} \int dr \phi_{j'}^*(r - R_{l'}) H(r) \phi_j(r - R_l) \end{aligned} \quad (2.11)$$

By solving (2.9), we can get m different energy E_n . Thus, the number of energy band is determined by the total number of atomic orbital in each unit cell.

In the case of graphite, there are two atoms in one unit cell. Each atom contributes one orbital so that there are two orbitals in each unit cell. Therefore, it has two energy levels. The two types of orbital are denoted in red (triangle) (orbital 1) and blue (diamond) (orbital 2) color in the schematic diagram 2.4, where one orbital is neighbored by three orbitals of the other type.

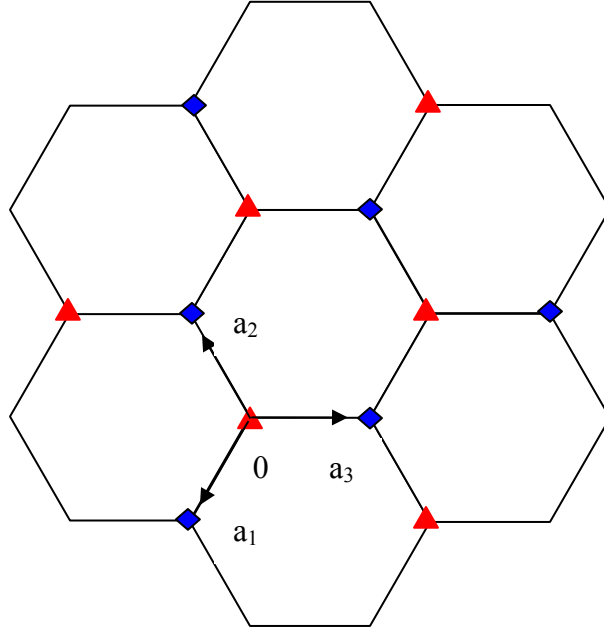


Figure 2.4: The two types of orbital are represented by triangle (orbital 1) and diamond (orbital 2) in the schematic diagram above, where one orbital is neighbored by three orbitals of the other type.

H_{11} can be calculated by substituting the wave functions made of type 1 orbital into (2.11) as:

$$H_{11} = \sum_{R_l} e^{ik(R_l - R_l')} \int dr \phi_1^*(r - R_l') H(r) \phi_1(r - R_l) \quad (2.12)$$

Let's choose the position of atom 0 as R_l' and then sum up all the other orbitals in red (triangle). Notice that all the other red orbitals except atom 0 itself are at distance more than one neighbor away from atom 0, so they are not counted in the nearest neighbor approximation:

$$H_{11} = \int dr \phi_1^*(r - R_l') H(r) \phi_1(r - R_l') = \varepsilon_0 \quad (2.13)$$

For the same approach:

$$H_{22} = \int dr \phi_2^*(r - R_{l'}) H(r) \phi_2(r - R_{l'}) = \varepsilon_0 \quad (2.14)$$

And for H_{12} :

$$H_{12} = \sum_{R_{l'}} e^{ik(R_l - R_{l'})} \int dr \phi_1^*(r - R_{l'}) H(r) \phi_2(r - R_{l'}) \quad (2.15) \text{ If}$$

we chose atom 0 as $R_{l'}$, then there are three type 2 orbitals which are the nearest neighbors,

so we have:

$$\begin{aligned} H_{12} &= (e^{ik a_1} + e^{ik a_2} + e^{ik a_3}) \int dr \phi_1^*(r - R_{l'}) H(r) \phi_2(r - R_{l'}) \\ &= t (e^{ik a_1} + e^{ik a_2} + e^{ik a_3}) \end{aligned} \quad (2.16)$$

a_1 , a_2 , and a_3 represent the real space vector positions for the three nearest neighbors of atom 0 and k is the reciprocal lattice vector that consists of \mathbf{g}_1 and \mathbf{g}_2 .

For H_{21} , we have:

$$H_{21} = H_{12}^* \quad (2.17)$$

Finally the band energy E is then determined by

$$\det \begin{vmatrix} H_{11} - E & H_{21} \\ H_{12} & H_{22} - E \end{vmatrix} = 0 \quad (2.18)$$

Equation (2.18) can be written as:

$$(\varepsilon_0 - E)^2 = \left| t (e^{ik a_1} + e^{ik a_2} + e^{ik a_3}) \right|^2 \quad (2.19)$$

By applying the tight bonding model calculated above, the electrical band of a seamless

SWCNT can be derived from the dispersion relation of a graphite sheet as

$$E(\alpha, \beta) = \pm |t| (3 + 2 \cos(2\pi\beta) + 2 \cos(2\pi\alpha) + 4 \cos(\alpha + \beta)2\pi)^{\frac{1}{2}} \quad (2.20)$$

$$e^{i\vec{k}\cdot\vec{C}_h} = 1$$

where $t=2.5-3.2$ eV is the nearest neighbor-hopping parameter. The vector \mathbf{k} ($\mathbf{k}=\alpha\mathbf{g}_1+\beta\mathbf{g}_2$) is composed of the reciprocal lattice unit vector \mathbf{g}_1 and \mathbf{g}_2 , which are derived from the real space unit vector \mathbf{a}_1 and \mathbf{a}_2 . The periodic boundary condition is confined along the tube circumference and the \mathbf{C}_h vector; therefore, the two-dimensional wave vector has to satisfy the boundary condition of $(\frac{2e^2}{h}) e^{i\vec{k}\cdot\vec{C}_h}$. This means that it needs to be conformed by the equation as followed:

$$2\pi(\alpha n + \beta m) = M 2\pi \quad (M=\text{integer})$$

Explicitly, there is no bandgap, when $E(\alpha, \beta) = 0$, only if the electron states are located among the six corners of the first Brillouin zone. This results in the creation of metallic conductance nanotube where:

$$(n-m)=3M \quad (M=\text{integer})$$

The rest of the nanotubes which do not follow the above equation will be semiconducting, and all armchair nanotubes are metallic.

It has been experimentally confirmed that SWCNTs [51], SWCNT bundles [52], or MWCNTs [53] behave like a quantum wires intrinsically due to the quantum confinement which leads to the ballistic transportation condition of carbon nanotubes. The confinement of the electrons is along the direction of the tube circumference. The conductance for a nanotube is given by $G=G_0M= (\frac{2e^2}{h})M$, where $G_0=(\frac{2e^2}{h})= (12.9 \text{ k}\Omega)^{-1}$ is quantized conductance. M is an apparent number of conducting channel. The experimentally

measured conductance is much lower than the theoretical value. The measured resistance for a single SWCNT is ~ 10 k Ω , as compared with the 6.45 k Ω predicted for the ideal SWCNT [54].

2.1.3 Mechanical Properties of carbon nanotubes

Carbon nanotubes have distinguished mechanical properties due to their high strength-to-weight ratio. Since σ bonding is the strongest bonding in nature; hence, a nanotube that is structured with all σ bonding is regarded as the ultimate fiber with the strength in its tube axis. Both experimental measurement and theoretical calculations approve that a nanotube is as stiff as or stiffer than diamond with the highest Young's modulus and tensile strength. Table 2.3 is the Young's modulus and tensile strength of nanotube comparing with other materials [8]. Young's modulus is independent of tube chirality, but depends on tube diameter. Defect free nanotubes are stronger than graphite because the axial component of σ bonding is greatly increased when a graphite sheet is rolled to form a seamless cylindrical shape structure or a SWCNT. The highest value is from tube with diameter between 1 and 2 nm, about 1 TPa. For a coaxial MWCNT which consists of different diameter of SWCNTs, the Young's modulus will take the highest value of a SWCNT plus contributions from coaxial intertube coupling or van der Waals force. Therefore, the Young's modulus for MWCNT is higher than a SWCNT, typically 1.1 to 1.3 TPa.

When nanotubes are bent, they buckle up together as reported by Despres et al [55]. The number of buckles depends on the degree of curvature and the diameter of the tubes. After

releasing from the bending force, CNTs straightened out without any damage, indicating that nanotubes are not only flexible, but also extremely elastic. A giant elastic response occurs when a nanotube is to be deformed. Macroscopically, the stiffest materials fail with a strain of approximately 1% because of dislocations and defects. On the other hand, CNTs can sustain up to 15% tensile strain before fracture [56]. Thus, the tensile strength of an individual nanotube can be as high as 150 GPa, assuming 1 TPa for Young's modulus. The flexibility and elasticity of carbon nanotubes is related to the in-plane flexibility of planar graphite sheet and the rehybridization ability of sp^2 - sp^3 of carbon atoms, where the degree of sp^2 - sp^3 rehybridization depends on the degree of curvature. Such a high elastic strain for several deformation modes of carbon nanotubes is originated from sp^2 rehybridization in nanotubes through which the high strain gets released.

However, sp^2 rehybridization will lead to a change in electrical properties of a nanotube. In asymmetric tubes ($0 < \theta < 30^\circ$), strain will cause asymmetric σ - π rehybridization and therefore the change in electric properties. The armchair nanotubes are intrinsically metallic and open a band gap under torsional strain, and the zigzag metallic nanotubes open a band gap under tensile strain, not torsional strain [57, 58].

	Young's modulus (GPa)	Tensile strength (GPa)	Density (g/cm ³)
MWCNT	1200	~150	2.6
SWCNT	1054	75	1.3
SWCNT bundle	563	~150	1.3
Graphite (in plane)	350	2.5	2.6
Steel	208	0.4	7.8

Table 2.3: Mechanical properties of carbon nanotubes [8].

2.1.4 Magnetic Properties of Carbon Nanotubes

Dauids et al. reported that carbon nanotubes should exhibit a paramagnetic- to diamagnetic-ordering transition when the radius of nanotubes increases above a critical value which estimated to be 6.4 \AA [59]. Magnetic properties such as anisotropic g-factor and susceptibility of nanotubes are expected to be similar to those for graphite while some unusual properties may exist for nanotubes. The magnetic properties can be measured by electron spin resonance (ESR). The average observed g-value is 2.012 [60] and spin susceptibility is $7 \times 10^{-9} \text{ emu/g}$ in MWCNT, which are slightly lower than those in graphite (2.018 and $2 \times 10^{-8} \text{ emu/g}$, respectively).

An interesting electrical response of the carbon nanotubes under a certain external magnetic field is expected. Ajiki et al. have considered the effect on the electronic states near the Fermi level of magnetic fields both perpendicular and parallel to the nanotube axis

[61, 62]. For magnetic field oriented parallel to the nanotube axis, the magnetic moment was found to oscillate as a function of magnetic flux. For metallic nanotubes, their results indicate that for small flux, the magnetic moment is in the same direction as the flux. For the semiconducting nanotubes, the magnetic flux and magnetic moment are in the opposing direction. Lu has reported that a metal-insulator transition and a band gap change occur for semiconducting tubes under magnetic field parallel to the tube axis [63]. A similar electrical response can also be found when magnetic field is perpendicular to the tube axis.

The major magnetic character of carbon nanotube is that the band gap change is oscillatory; therefore, the semiconducting and metallic nature of nanotubes can be tuned by applying an external magnetic field, which is so called Aharonov-Bohm effect. The oscillatory behavior is confirmed by experimental measurements of resistance change in MWCNTs with the tube axis parallel to magnetic field [64].

2.1.5 Chemical Properties of Carbon Nanotubes

Carbon nanotubes have unique properties of small diameter, large surface area, and σ - π rehybridization. These make carbon nanotubes very attractive in chemical and biological applications. The chemical properties of carbon nanotubes such as opening, wetting, filling, absorption, charge transfer, doping, and intercalation have been studied. Carbon nanotubes are highly graphitized carbonaceous materials, which result in low chemical reactivity. One important chemical reaction is their oxidation at raised temperature. Ajayan et al. found that by increasing the temperature above 750°C, the nanotubes start to oxidize from

the tip inward, layer by layer, which results eventually in open and thinner tubes [65, 3]. The increase reactivity of the tip must be due to the strain associated with very high curvature. Hui et al. confirmed that the oxidation process covers the nanotubes surface with three different oxides: carboxylic (-COOH), carbonyl (-CO), and hydroxylic (-COH) groups. These external functional groups in turn improve the chemical reactivity of the nanotubes and modify their wetting properties [66]. While nanotubes are able to oxidize in a controllable way, nanotubes can exhibit to be very sensitive to chemical reduction.

Ebbesen et al. introduced alkali metals into nanotubes, and found that the nanotubes doped with alkali metals are gradually degraded upon mild heat treatment. It is believed that the alkali metals are able to intercalate by entering through dislocations in graphite sheet or they react with defects such as 5,7 pairs, which may be much sensitive to reduction than oxidation [3, 67].

Enhanced molecular absorption and charge transfer are also the unique properties of carbon nanotubes. The gas adsorption and charge transfer capability are functions of sites and gas molecules. The site where a gas molecule can be absorbed included interstitial in tube bundles, groove above the gap between either two closest tubes, nanopore inside a tube, and surface of a single tube [68]. A conductance change presents as the gas molecules are introduced to contact with nanotubes. O₂ has been studied to be dominantly absorbed on the surface of as-grown carbon nanotubes, resulting in a p-type behavior whereas it has been argued that water is the major reason [69]. Features of electrical response of carbon nanotubes to chemical absorption make them useful for chemical applications and gas detection sensor applications.

2.2 Growth Techniques of Carbon Nanotubs

2.2.1 Carbon nanotubes growth by arc discharge

MWCNTs were first found on the cathode surface by Iijima [2], which were produced by carbon arc discharge. The carbon arc discharge is a convenient method to produce diverse structures of carbon materials due to the high temperature of plasma, which approaches 3700° C [70]. Previously, carbon arc has been used to generate structures such as carbon whiskers, soot, and fullerenes [71, 72]. Although it is convenient for generating different sizes of structures, one of the critical parameters that determines the structures is the type and pressure of the gas surrounding the arc.

Basically, arc discharge carbon nanotubes growth can be divided into non-catalyst growth and catalyst assisted growth. The shape and the cross section of the cathode which has nanotubes deposit on it closely mimic the shape of the consumed anode. For instance, if an anode rod with a circle cross section creates a cathode deposit with a similar cross section and a circle core. Such cylindrical deposition consists of a hard gray outer shell and a soft fibrous black core. During synthesizing MWCNTs, the main by-products are multiwall polyhedral particles, and various kinds of graphitic nanoparticles.

The dc arc discharge method was first optimized by Ebbesen et al. [73]. It becomes a common method for synthesizing MWCNTs. A schematic diagram of the arc discharge operating apparatus is shown in Figure 2.5 [3]. A long cylindrical-shaped deposit on the front of the cathode surface contained gram quantity of MWCNTs, which is produced by evaporating anode. The direct current arc, which is usually generated at 20V and 500 Torr,

operates in a 1- to 4- mm wide gap between two graphite electrodes that are installed in a water-cooled chamber filled with helium gas at subatmospheric pressure. The cylindrical deposit grows at a rate of about 1 to 2 mm/min. In order to stabilize the discharge, one electrode needs to be moved in such way that the gap distance between two electrodes remains the same, which can be monitored by the current value. The current is experimentally optimized at approximate 150 A/cm^2 at 20V (i.e. $\sim 50\text{A}$ for a 6mm diameter electrode) [3].

The arc is basically dynamic and the regions where the plasma is generated moved over to the electrode surface; therefore, a temperature gradient exists in the plasma which results in the size variation of CNTs. Carbon nanotubes are not found to be anywhere in the chamber after using carbon arc discharge, for instance, they are absent in the soot where fullerenes condense. This indicates that the deposition of nanotubes is only found where the current is flowing. It is reported that too much current results in harden materials and fewer free nanotubes [70]. On the other hand, lower the current results in a better yield of nanotubes deposition [74].

Carbon nanotubes produced from carbon vapor generated by arc discharge and laser ablation of graphite generally have fewer structural defects than those produced by the other techniques. This is due to the higher temperature growth that ensures perfect annealing of defects in tubular graphite sheet. High quality of MWCNTs can be obtained by arc discharge method, but obtaining high yields of carbon nanotubes is the major concern for using this method. Controlling helium gas and dc current are the most important parameters to optimize yield. Therefore, a stable and high yield arc process requires a constant feed rate and arc current during the synthesis. Among the various inert

gases, helium gives the best result probably because of its low ionization energy. Table 2.4 shows the effect of gas pressure [8].

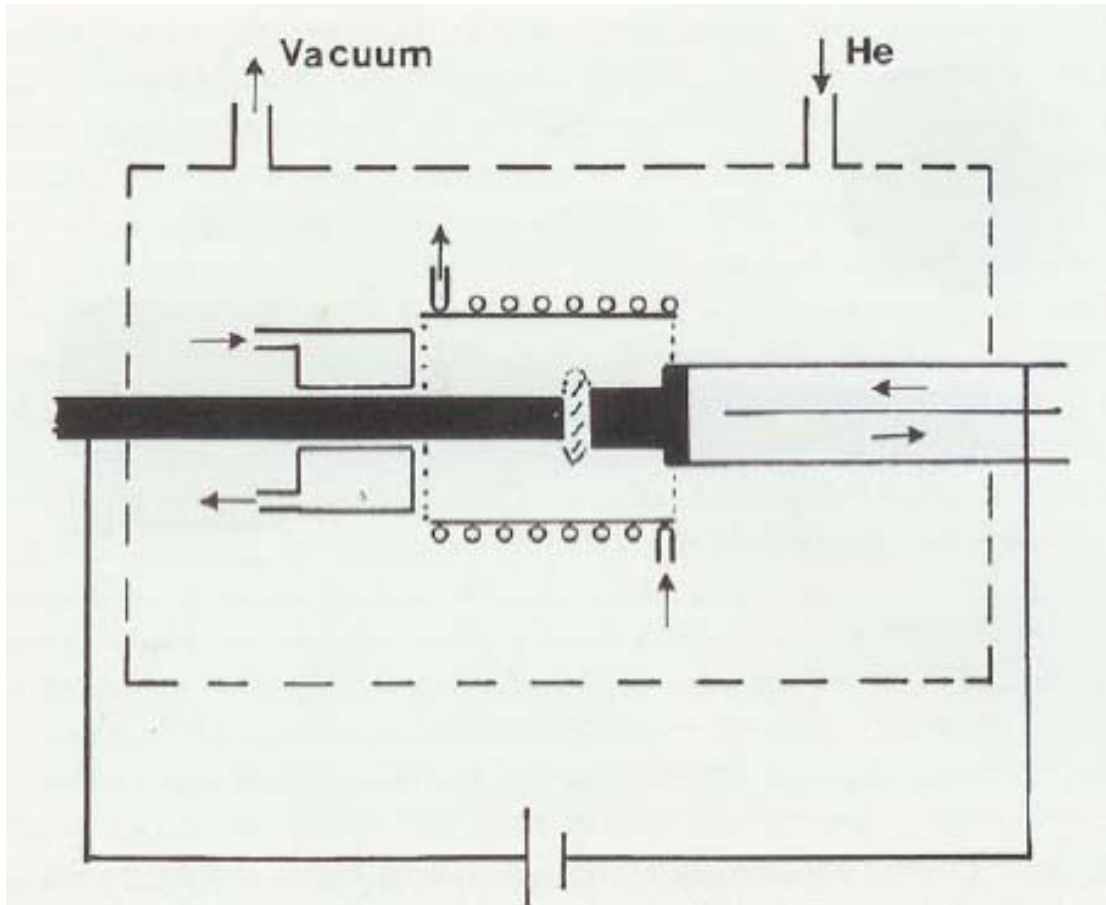


Figure 2.5: Schematic diagram of the arc discharge apparatus where carbon nanotubes are formed from the plasma between the two black carbon rods. All the arrows indicate for the vacuum and the He lines are water-cooling system [3].

N	He, (Torr)	I, (A)	Feed rate (mm/min)	Gap (mm)	Deposit diameter (mm)	Growth rate (mg/min)	MWCNT amount (%)	MWCNT diameter (nm)
1	100	80	4	3.9	7.8	115	5	8-20
2	200	65	4	2.2	6.5	170	10	8-22
3	700	55	4	0.5	7.4	260	20	8-23
4	500	65	8	0.4	8.0	350	20	5-29
5	500	65	2.5	3.5	7.6	90	30	5-46
6	1500	65	1.4	4.2	5.5	20	35	4-60
7	2000	65	1.4	3.3	5.5	22	30	4-60
8 ^a	500	160	0.65	0.8	11.6	160	30	5-50
9 ^b	500	132	1.0	1.7	10.9	195	30	5-50

Table 2.4: Parameters of the MWCNT arc synthesis with 6-mm diameter anode rods [8].

SWCNTs can also be synthesized by arc discharge process utilizing co-evaporation of graphite and metal in a composite anode. The anode is commonly made by drilling an axial hole in the graphite rod, and densely packing it with a mixture of metal and graphite powders [75, 76]. The amount of catalyst depends on the type of catalyst, but there is clear evidence that more nanotubes are formed in the presence of larger amounts of catalysts [81]. Several pure elements and mixtures have been used to fill the axial hole of the rod, including Fe, Ni, Co, Cu, Pt, Y, Zn, Fe/Ni, Co/Ni, Co/Pt, Ni/Y, and Ni/Ti [8, 77-80].

Among these mixtures, Ni/Y, and Co/Ni catalysts are commonly used in SWCNTs synthesis. The metal compounds used as the catalyst in electric arc method at 500 Torr He are listed in Table 2.5 [82].

Metals/compounds	Location of SWNT	Density of SWNT
Fe	Soot	Low
Ni	Soot	Low
Co	Soot	High
	Weblike	High
Fe/Ni	Soot	Very high
	Weblike	Very high
Fe/Co	Soot	High
	Weblike	Very high
Ni/Co	Soot	Very high
	Weblike	Very high
Ni/Cu	Soot	Low
Ni/Ti	Soot	Very low
Cu/Co	Soot	Low
Mg/Ni	Soot	Low
Y ₂ O ₃ /Co	Soot	Low, radial
YC-2	Soot	High, radial

Table 2.5: Metals and metal compounds catalysts for SWCNT synthesis (Modified from ref. [82]).

The mixed carbon and metal vapor, which escapes from the gap, condenses into several products. Subsequently, these products are traveled to the reactor surfaces and deposited. The major products are divided into three distinct structures, depending on the coating locations. (1) Spongy soft belts called collaret, which contains more SWCNTs and metal catalysts than other components of products, are formed around the cylindrical deposit, (2)

clothlike soot on the chamber walls, and (3) some weblike structure suspended in the chamber volume between cathode and walls [8]. All three locations contain different amount of SWCNTs, fullerenes, amorphous carbon, and so on.

SWCNTs are mostly organized in bundles that consist of a few dozen tubes, tightly bonded in a honeycomb lattice. The bundles are covered with an amorphous carbon layer, which contains embedded fullerenes. The majority of tubes have diameter in the range of 1.2 to 1.5 nm and the length up to tens of micrometers. The diameter of SWCNT depends on the temperature of the catalytic site where the deposition occurs. The temperature is regulated by many factors including heating of the reactive zone with an external controlled heat source. Takizawa et al. found out that the average diameter of SWCNTs increase as the environment temperature increases; moreover, the environment temperature also affects the yield of SWCNTs [83, 84].

2.2.2 Carbon nanotubes growth by laser ablation

Carbon nanotubes can also be synthesized by laser vaporization apparatus with an ablated pure graphite target located in an oven. It was found that closed-ended MWCNTs were produced in the gas phase through homogeneous carbon-vapor condensation in a hot argon/or helium atmosphere [85]. MWCNTs synthesized by laser ablation are relatively short (~300 nm) compare to those by arc discharge. The number of layers deposited by laser ablation is ranging between 4 and 24. The inner diameter deposited varies from 1.5 to 3.5 nm. The yield and quality of MWCNTs degrade when the oven temperature is below 1200°C, and no nanotubes are observed at 200°C.

Laser system for synthesizing carbon nanotubes can be operated in either pulsed mode or continuous mode. Figure 2.6 shows a schematic diagram of the traditional laser ablation system for carbon nanotubes growth [86]. A graphite target is loaded in the center of a quartz tube furnace that is filled with inert gas. The operating temperature is set at 1200°C. The laser beam is focused at the graphite target in order to vaporize and sublime the graphite by uniformly bombarding its surface. The carbon species swept by a flow of neutral gas are thereafter coated as soot in different regimes: (1) on the conical water-cooled copper collector, (2) on the wall of quartz tube, and (3) on the backside of the target.

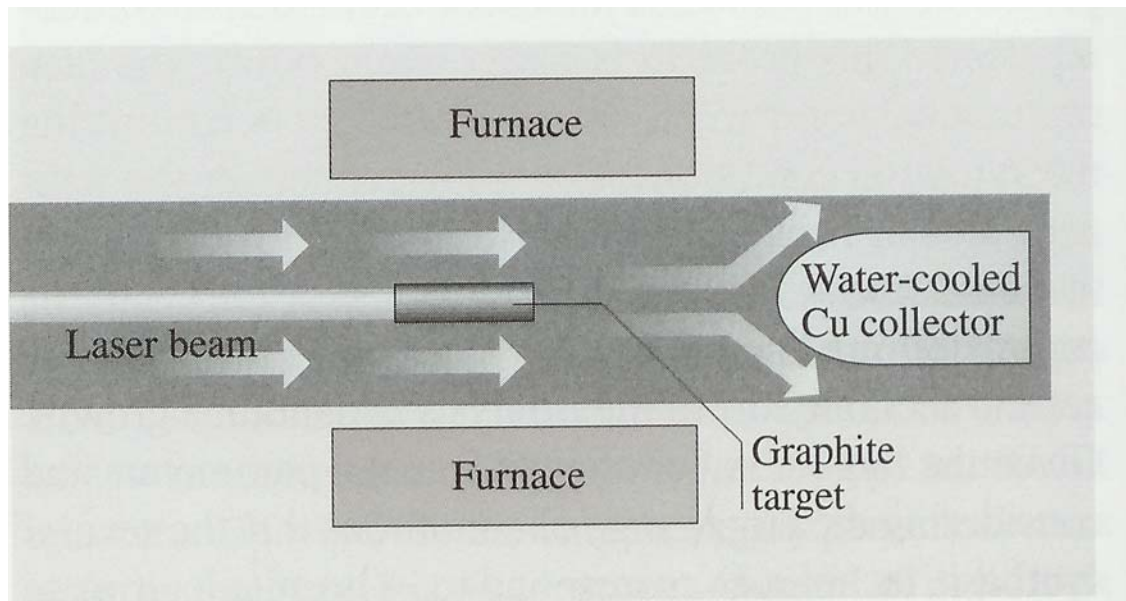


Figure 2.6: Schematic of laser ablation setup for carbon nanotubes growth [86].

Laser ablation is also an efficient route for synthesizing SWCNTs bundles with a narrow diameter discrepancy. In the early report of the laser ablation method, high yields with conversion of graphite to SWCNTs were reported in the condensing vapor of the heat flow tube ($>1200^{\circ}\text{C}$) [87]. Laser ablation can produce SWCNTs by evaporating metallic-contained graphite target as well.

Instead of using furnace-based laser vaporization system, a continuous CO_2 laser has been used. Figure 2.7 is a schematic sketch of a synthesis reactor based system [86]. The operating power can be tuned from 100W to 1600W, and the target temperature is measured by an optical pyrometer. The floating inert gas acts as a local furnace and creates an extended hot zone for enhancing the vaporization of carbon species. The gas was extracted through a silica pipe, and the solid products formed are carried away by the gas flow through the pipe and then collected on the filter. The synthesis yield can be controlled by: (1) the cooling rate of the medium, (2) the residence time, and (3) the temperature at which SWCNTs nucleate and grow [86]. The SWCNT yield and properties are reported to be relatively sensitive to the processing parameters such as light intensity, type of metal catalyst, process temperature, type of carrier gas, flowing dynamic and rate, etc. However, laser ablation is able to produce high yield and high quality carbon nanotubes due to sufficiently high temperature that rapidly anneal the imperfect fullerene structures into a closed form through the incorporation and rearrangement of pentagons [88]. The disadvantage of using laser ablation is the lack of large-scale production capability.

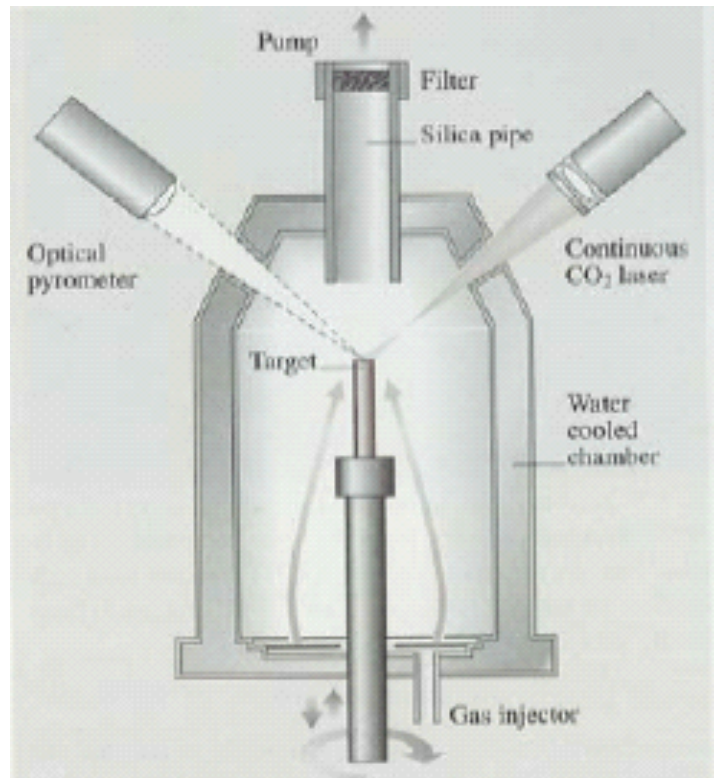


Figure 2.7: Schematic of commonly used laser ablation reactor for SWCNTs growth [86].

2.2.3 Carbon nanotubes growth by chemical vapor deposition

Using carbon nanotubes for nanoelectronics, field emission applications require more precisely controllable growth on patterned substrate at reasonable rates. This requirement can be satisfied by introducing chemical vapor deposition (CVD). One CVD method for CNTs growth is thermal chemical vapor deposition, in which a conventional heat source such as resistive or inductive heater, furnace or infrared (IR) lamp is used for heating up the environment temperature. Another CVD method is so-called plasma-enhanced chemical vapor deposition (PECVD), in which the plasma source is used to create a glow discharge which contains desirable radicals, electrons, and ions.

DC, RF (13.56 MHz), or microwave (2.45 GHz) sources can be used to generate plasma (Figure 2.8) [8]. A plasma reactor consists of a pair of electrodes in a grounded chamber with one grounded and the other connected to a power supply. A breakdown of feed gas occurs when a negative bias is applied ($>300\text{V}$) on the cathode. The resulting glow discharge composed of electrons, positive and negative ions, atoms, and radicals. The separation distance between two electrodes is determined by $Pd=\text{constant}$ where P is the pressure and d is the distance between two electrodes. This indicates that electrodes need to be pulled away further as the pressure is decreased in order to sustain the discharge.

The electrode holding the substrate needs a separate heat source in order to elevate the wafer temperature to a desired growth temperature, and to enhance the nucleation density. In carbon nanotubes growth by CVD, precursor dissociation in the gas phase is not necessary. However, dissociation at the catalytic particle surface appears to be the key point for nanotubes growth. It is necessary to maintain the growth temperature below the

pyrolysis temperature of the particular hydrocarbon in order to prevent excessive production of amorphous carbon [8]. Since the plasma can ionize the hydrocarbon gases that create a lot of reactive radicals, pure hydrocarbon feedstock in plasma reactors may result in substantial amorphous carbon deposition. It is necessary to dilute the hydrocarbon gases with argon, hydrogen, or ammonia. Typical reacting pressures of nanotubes deposition is in a range from 1 to 20 Torr. PECVD allows nanotubes to grow at a much lower temperature compares to other methods, which makes it attractive for integrating carbon nanotubes into the applications of semiconductor device fabrication. Moreover, the local electrical field generated between plasma and the substrate holder provides nanotubes to grow extremely vertical and high density growth. PECVD enable more vertically aligned carbon nanotubes structure growth than thermal CVD does. Whereas any marginal alignment nanotubes observed in thermal CVD samples are resulted from crowding effect, nanotubes supporting each other by van der Waals attraction. Thus, individual, free-standing and vertically oriented structures are possible with PECVD.

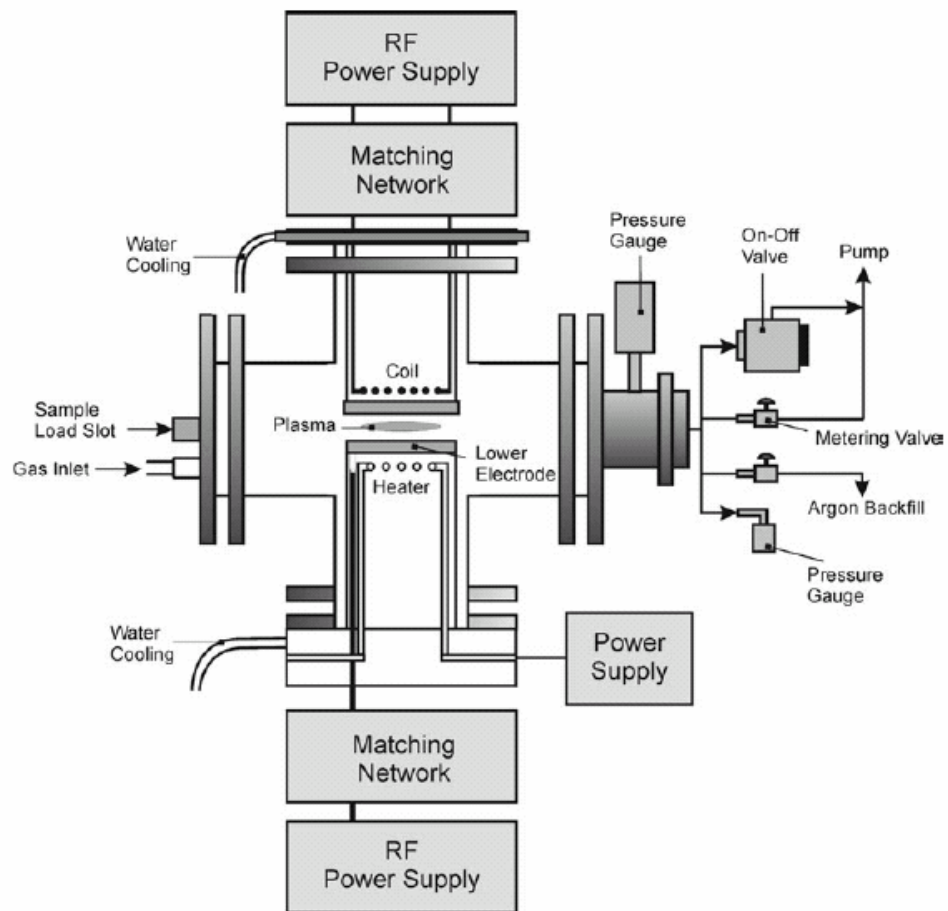


Figure 2.8: Schematic diagram of a PECVD setup for carbon nanotubes growth [8].

2.2.4 Carbon nanotubes growth mechanisms

Metal catalyst assisted carbon nanotubes growth can be divided into two sections, tip growth and base growth. Five major phenomena as followed need to be carefully concerned:

1. Precursors diffusion through a thin boundary layer of the substrate.
2. Reactive species adsorption at the particle surface.
3. Surface reactions results in nanotube structure and by-product of hydrocarbon gases.
4. Desorption of gaseous product species from the surface.
5. Outgassing species diffusion through the boundary layer into the bulk stream.

In nanotubes growth, the above steps may proceed differently in thermal CVD and in PECVD. For instance, thermal CVD reactor has only a few other species in the gas phase besides the feedstock hydrocarbon gases; however, PECVD is specified by a diversity of energetic radicals and atomic hydrogen, along with stable higher hydrocarbons and ions in the plasma. In low temperature PECVD growth, positive ion bombardment on the substrate may provide enough energy for steps (1) and (3) or in aid of desorption in step (4). In thermal CVD or PECVD methods, hydrocarbons or radicals get rid of their hydrogen atoms, and eventually breaking some of their C bonds which construct on the particle surface to form nanotubes. A hydrocarbon adsorbed on the catalytic particle releases carbon upon decomposition, which dissolve and diffuse into the metal particle. When a supersaturated state is reached, carbon precipitates in a crystalline tubular form. At this juncture two different situations are possible, one is tip growth and the other one is base growth. The growth and nucleation of carbon nanotubes strongly depend on the diffusion

process of carbon species through the catalytic metal particles. Louchev's model gives a good explanation of the top and base growth (Figure 2.9) [89]. Two characteristic times are defined as (1) the characteristics diffusion time of carbon through the metal nanoparticle to the other end, which is the nanotube growing point, given by,

$$\tau_d = R_p^2 / D_b$$

where R_p is the radius of catalytic metal particle and D_b is the diffusion coefficient, and (2) the surface saturation time of order

$$\tau_s = C^2 D_b / Q^2$$

where C is the saturation concentration of carbon and Q is the impinging carbon flux. The saturation condition of the metal catalytic surface is a function of the carbon species contain to the saturation concentration, kindling the carbon precipitation in the outer surface of the metal particle. If $\tau_d \ll \tau_s$, which means the rate of carbon species diffuses through the metal particle is much faster than that of the particle surface reaches the saturation value, carbon precipitates at the bottom of the catalytic particle, lifting the particle during the growing process, resulting in a tip-growth condition. On the other hand, if $\tau_d \gg \tau_s$, which means the rate that metal particle surface is saturated with carbon is much faster than that of carbon diffuses through the body of the particle, a precipitation of carbon on the catalytic particle surface occurs, providing a nucleation template for carbon nanotubes. Consequently, the nanotube grows out of the surface of the metal particle, and the particle remains at the root of the nanotube throughout the growth process, which is so-called base growth. In addition, the diffusion of carbon species also depends on the particle adherence to the surface. If the adherence is strong enough, base growth is often presented, and if the adherence is weaker, tip growth is mostly occurred.

Baker and coworkers [90] implied that carbon filament is formed by decomposing the hydrocarbon on the top surface of the metal catalyst. It then diffuses into the metal particle and finally precipitates at the other end of the particle. Mechanisms for carbon filament growth depend on the temperature, activation energy, and electron microscopy observations. It is generally agreed that carbon nanotube has the same growth mechanism as carbon filament due to the visual evidence of catalyst particles on the top or bottom end of nanotubes, as they are the case with filament studies.

Consequently, carbon nanotube growth strongly depends on the nucleation site, the size and adhesion of metal particles, and carbon diffusion parameter. The diffusion parameters are related to the size and adherence of the metal particles, growth temperature, feeding gases, and the character of the metal that is used as catalyst.

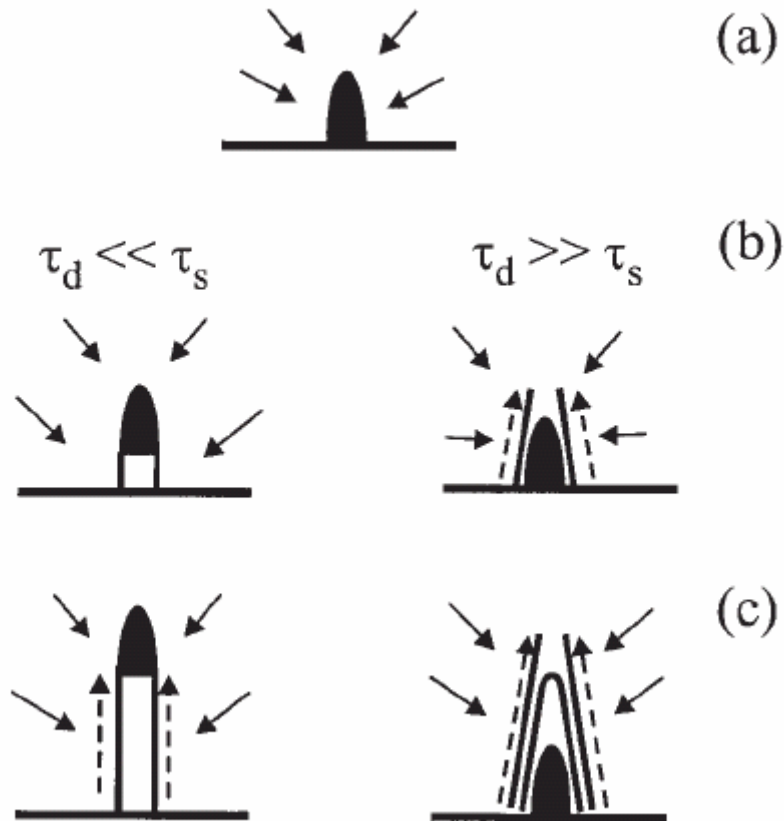


Figure 2.9: Schematic of tip and base carbon nanotubes growth mechanisms. On the left hand side, the nanoparticle is detached from the substrate on the tip of nanotube, catalyzing growth and preventing nanotubes closure. On the right hand side, the nanoparticle remains on the substrate, severing as an initial template for nanotubes nucleation. Figure (a) shows the nanoparticle is saturated by carbon species (b) stage of nanotubes nucleation (c) post-nucleation growth [89].

2.3 Structure and material properties of zinc oxide nanostructure

2.3.1 Structure of ZnO

ZnO is one of the attractive functional oxides, which is semitransparent. It is also an II-VI compound semiconductor. Wurtzite ZnO has a stable hexagonal structure (space group $C6mc$) with lattice spacing $a=0.325$ nm and $c=0.521$ nm (Figure 2.10) [12]. Two important characteristics of the wurtzite structure are the non-central symmetry and the polar surface. ZnO can be simply described as a number of alternating planes consisted of tetrahedral coordinated O^{2-} and Zn^{2+} ions, which are stacked alternately along the c -axis. ZnO is a wide band gap (3.37eV) compound semiconductor that is suitable for short wavelength optoelectronic applications. ZnO also possesses large exciton binding energy (60meV) that ensures efficient excitonic emission at room temperature. Room temperature ultraviolet (UV) luminescence has been reported in disordered ZnO nanoparticles and thin films. Table 2.6 lists the basic physical properties of bulk ZnO [91]. As the dimension of the semiconductor materials continuously shrinks down to nanometer or even smaller dimension, some of their physical properties undergo dramatic change known as the “quantum size confinement effect”. The quantum confinement effect leads to an increase of the band gap energy of Q1D ZnO, which has already been confirmed by photoluminescence [92]. Band gap of ZnO nanoparticles also reported to be size dependent [93]

Properties	Value
Lattice constants (T = 300 K)	
a_0	0.32469 nm
c_0	0.52069 nm
Density	5.606 g/cm ³
Melting point	2248 K
Relative dielectric constant	8.66
Gap Energy	3.4 eV, direct
Intrinsic carrier concentration	< 10 ⁶ cm ⁻³
Exciton binding Energy	60 meV
Electron effective mass	0.24
Electron mobility (T = 300 K)	200 cm ² /V s
Hole effective mass	0.59
Hole mobility (T = 300 K)	5-50 cm ² /V s

Table 2.6: Physical properties of wurtzite ZnO [91].

The tetrahedral coordination in ZnO leads to a non-central symmetric structure, which is one of the most important characteristics of wurtzite nanostructured materials. The lack of central of symmetry in wurtzite structure, combined with large electromechanical coupling, resulting in strong piezoelectric and pyroelectric properties. The other important structural characteristic of ZnO is the polar surfaces. The most common polar surface is the basal plane.

An internal charge of ZnO is created by positively charged Zn-(0001) and negatively charged O-(000 $\bar{1}$) surfaces, resulting in the creation of dipole moment and spontaneous polarization along the c-axis as well as a divergence in surface energy [11, 12]. To maintain a stable structure, the polar surfaces generally have facets or exhibit massive surface reconstructions, but ZnO \pm (0001) are exceptions: they are atomically flat, stable and

without reconstruction [12, 13]. The other two most commonly observed facets for ZnO are $\{2\bar{1}10\}$ and $\{0\bar{1}10\}$, which are non-polar surfaces and they have lower energy than the $\{0001\}$ facets (Figure 2.11).

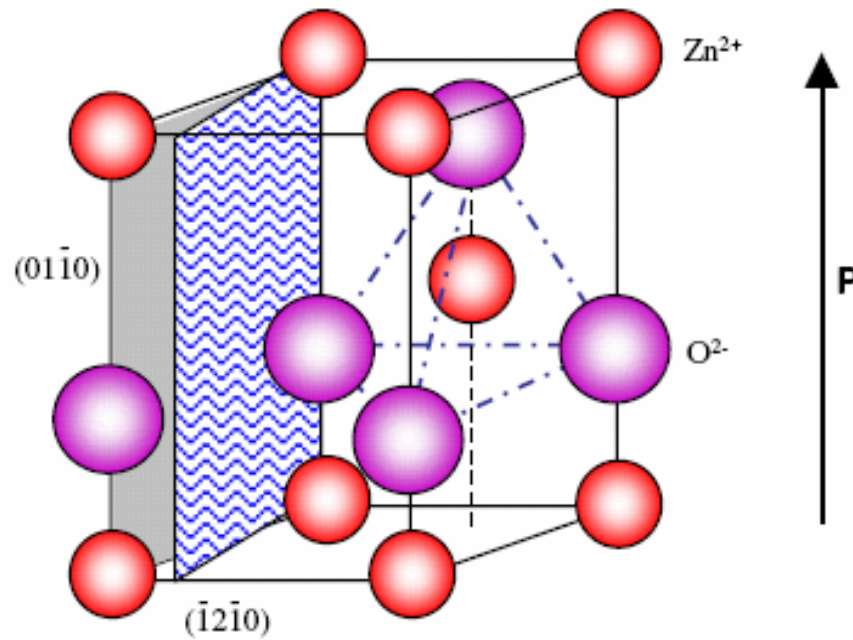


Figure 2.10: The wurtzite structure model of ZnO. The tetrahedral coordination of Zn-O is shown [12]

Structurally, ZnO has three types of growth directions: $\langle 2\bar{1}\bar{1}0 \rangle$, $\langle 01\bar{1}0 \rangle$, and $\pm[0001]$.

Figure 2.9 is the SEM image of the hierarchical ZnO structure [12]. All the growth orientations would aggregate together at the center $[0001]$ with the polar surface due to atomic terminations; ZnO displays a wide range of novel structures that can be grown by tuning the growth rates along these directions. One of the most profound factors determining the morphology involves the relative surface activities of various growth facets under given conditions. A crystal has different kinetic parameters for different crystal planes, which are emphasized under controllable growth conditions. Therefore, after an initial period of nucleation and incubation, a crystalline will commonly develop into a three dimensional structure with well defined, low index crystallographic faces. Figure 2.12 (a)-(c) show a few typical growth morphologies of 1D nanostructures for ZnO [12]. These structures lean to maximize the areas of the $\{2\bar{1}\bar{1}0\}$ and $\{01\bar{1}0\}$ facets due to the nature of energy minimization. The morphology shown in figure (d) is dominated by the polar surface, which can be grown by introducing planar defects parallel to the polar surfaces. Planar defects and twins are observed occasionally parallel to the (0001) plane, but dislocations are rarely seen [11-13].

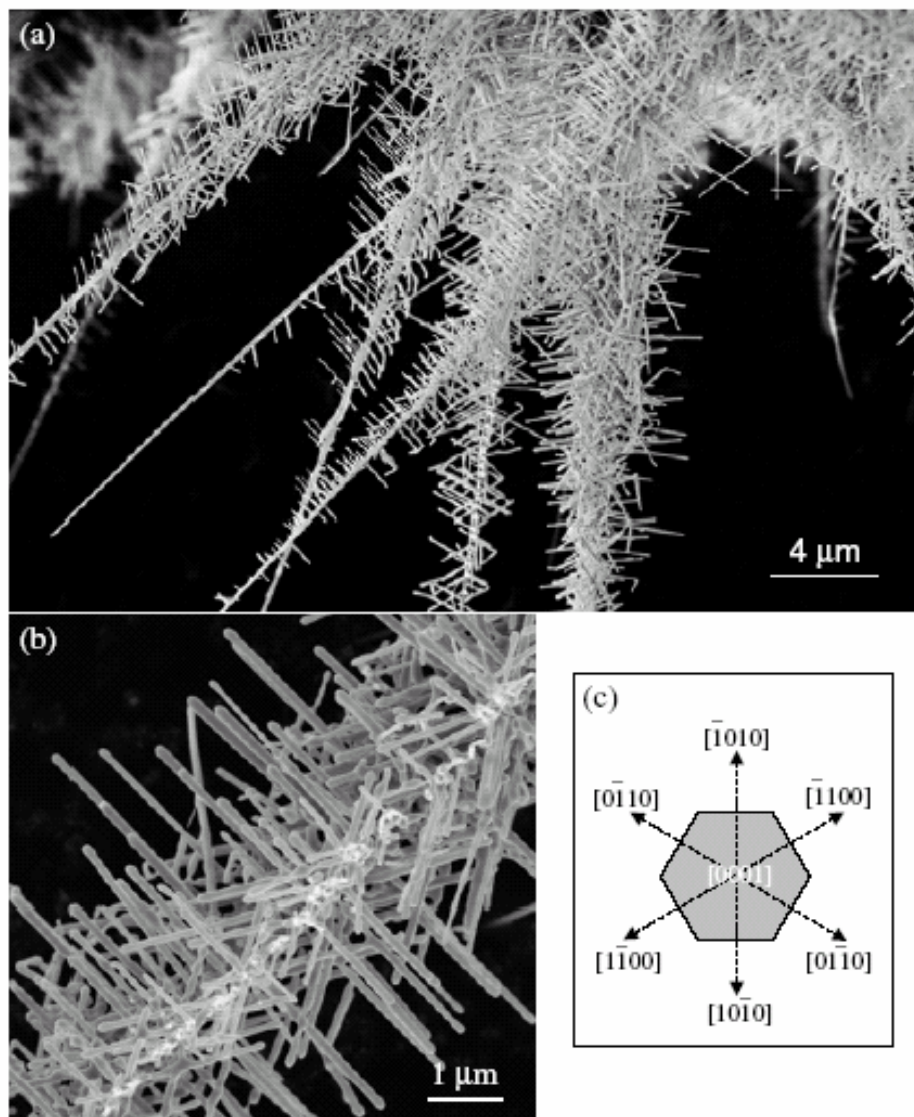


Figure 2.11: ((a), (b)) SEM images of the hierarchical ZnO nanowire junction arrays, (c) the growth model of the hierarchical structure [12].

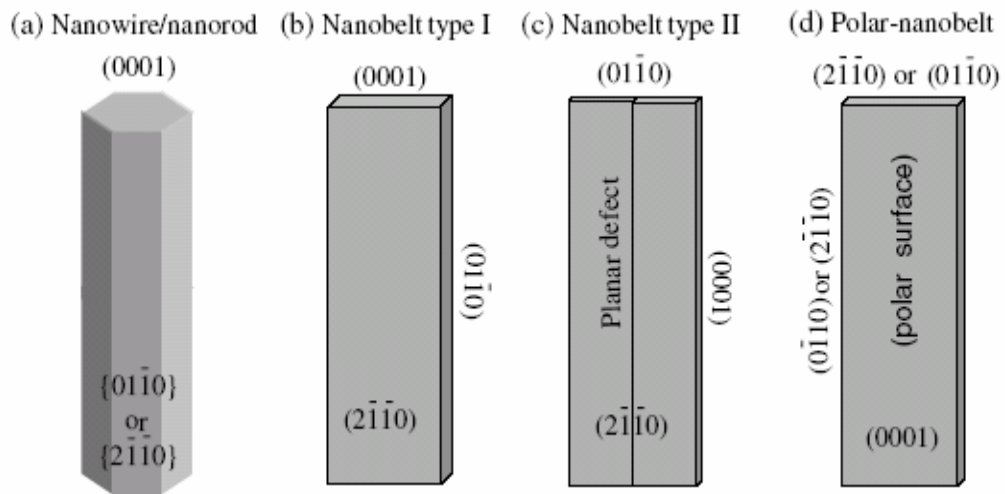


Figure 2.12: Typical growth morphologies of one-dimensional ZnO nanostructures and the corresponding facets [12].

2.3.2 Electrical properties of ZnO

Due to the native defects such as oxygen vacancies and zinc interstitials, ZnO nanostructured materials are reported to exhibit n-type semiconductor behavior. The electrical transport mechanism of ZnO nanowire is still far away from well known; however, measurements of electrical properties is in progress. Li et al. not only reported electrical transport measurement of individual nanowires and nanorods but also studied the I-V characteristics under diverse oxygen ambient [94-96]. First, ZnO nanowires were dispersed and deposited on SiO₂/Si substrate. Subsequently, photolithography was performed to pattern contact electrode arrays. I-V characteristics under different back gate voltages, carrier concentration, and mobility have been estimated (Figure 2.13 (a)). Finally, the source-drain I_{SD} versus source-drain V_{SD} characteristics are examined for one transistor at atmospheric condition (Figure 2.10(b)). As the Gate voltage, V_G, increases from -7V to 3V with 1V interval, current increased by 2-3 orders, and the conductivity at 0V of ZnO nanowire is calculated to be 2.5S/cm [95]. I_{DS} increases as V_G increases from -20 to 20V at a fixed V_{SD}=2V. This indicates that ZnO exhibits n-type semiconductor behavior (Figure 2.10(c)) [95]. Further decrease in V_G results in little impact on the change current. The origin of the n-type ZnO nanowire was related to the presence of the oxygen vacancies which demonstrates that a negative gate voltage effectively depletes the electrons in the ZnO nanowire and switches the device off [95]. These results indicate that a negative gate voltage effectively depletes the electrons in the ZnO nanowire and switches the device off.

Li et al. also demonstrate the I-V characteristics changed in diverse oxygen ambient, which indicates that the absorbed species affect the conductance of the individual ZnO

nanowire transistors [95]. Measurements were performed in vacuum (10^{-4} Pa), and then the oxygen was uniformly introduced into the system. The transfer characteristics were executed from -40 to 10 V at a fixed V_{SD} of 2V under different oxygen pressures. The results show that the current decreases and the threshold voltage (V_{th}) shifts positively as oxygen pressure increases. With increasing oxygen pressure, both carrier density and mobility decreased; however, the carrier density decreased more rapidly than the mobility (Table 2.7) [95]. These phenomena can be explained by the oxygen ions (O^- , O^{2-} , or O_2^-) which are formed by adsorbed oxygen molecules that deprived the electrons in the ZnO nanowire. Therefore, more electrons are captured by the oxygen when the oxygen pressure increases, which result in the decrease of the carrier density in the ZnO nanowire and the expansion of the depletion layer.

Oxygen pressure (Pa)	Electron density n_e (μm^{-3})	Mobility μ ($\text{cm}^2/\text{V s}$)
10^{-4}	12 400	8.2
920	9 300	5.9
63 000	4 900	3.7
10^5	1 500	3.0

Table 2.7 Electron density and mobility measurement under diverse oxygen pressures [95].

ZnO nanostructures grown by chemical vapor deposition are single crystalline, rendering them superior electrical properties than polycrystalline ZnO thin film. Generally, an electron field effect mobility of $7 \text{ cm}^2/\text{Vs}$ is regarded fairly high for ZnO thin film transistors; however, single crystalline ZnO nanowires show mobility as high as $80 \text{ cm}^2/\text{Vs}$ [14, 97]. A surprising result by Park et al. had reported an electron mobility of $1000 \text{ cm}^2/\text{Vs}$

after coating the ZnO nanowires with polyimide, which is used for reducing electron scattering and trapping at surface [98]. It is believed that ZnO nanostructures device can be operated at a faster speed than thin film does. P. Cheng et al. show that vapor trapping chemical vapor deposition for ZnO nanostructures growth provides high and tunable carrier concentration without incorporating impurities. The carrier concentration can be tuned by adjusting the location of ZnO deposition [97]. Depending on the growth location, the conductivities of single ZnO nanowires have been estimated to be $8.64\Omega^{-1}\text{cm}^{-1}$ and $1.02\Omega^{-1}\text{cm}^{-1}$, respectively (Figure 2.10(d)) [97]. Not only conductivities, but also carrier concentration and mobility show huge difference due to ZnO nanowires growth at different locations. Consequently, using a suitably and uniquely designed synthesis setup, one can adjust the carrier concentration and mobility of the ZnO nanowires.

The major obstacle for ZnO applications rests with the difficulty of p-type doping. Joseph et al. obtained low resistivity ($0.5\Omega\text{-cm}$) p-type ZnO thin film by using Ga and N co-doped method [100]. Look et al. reported nitrogen-doped p-type ZnO with a hole mobility of $2\text{cm}^2/\text{Vs}$ by using molecular beam epitaxy [101]. Successful doping of p-type ZnO broadens the application in nanoelectronics and optoelectronics. In addition, successful p-type ZnO nanowires can merge with n-type ZnO nanowires for p-n junction diodes and light emitting diodes applications. A great improvement of synthesize intramolecular p-n junction on ZnO nanowires was demonstrated by Liu et al [102]. Anodic aluminum membrane was used as a porous template, and a two step vapor transport growth was applied in which boron was introduced as the p-type dopant. Consequently, the I-V characteristics demonstrated rectifying behavior due to the formation of p-n junction within the nanowire [102].

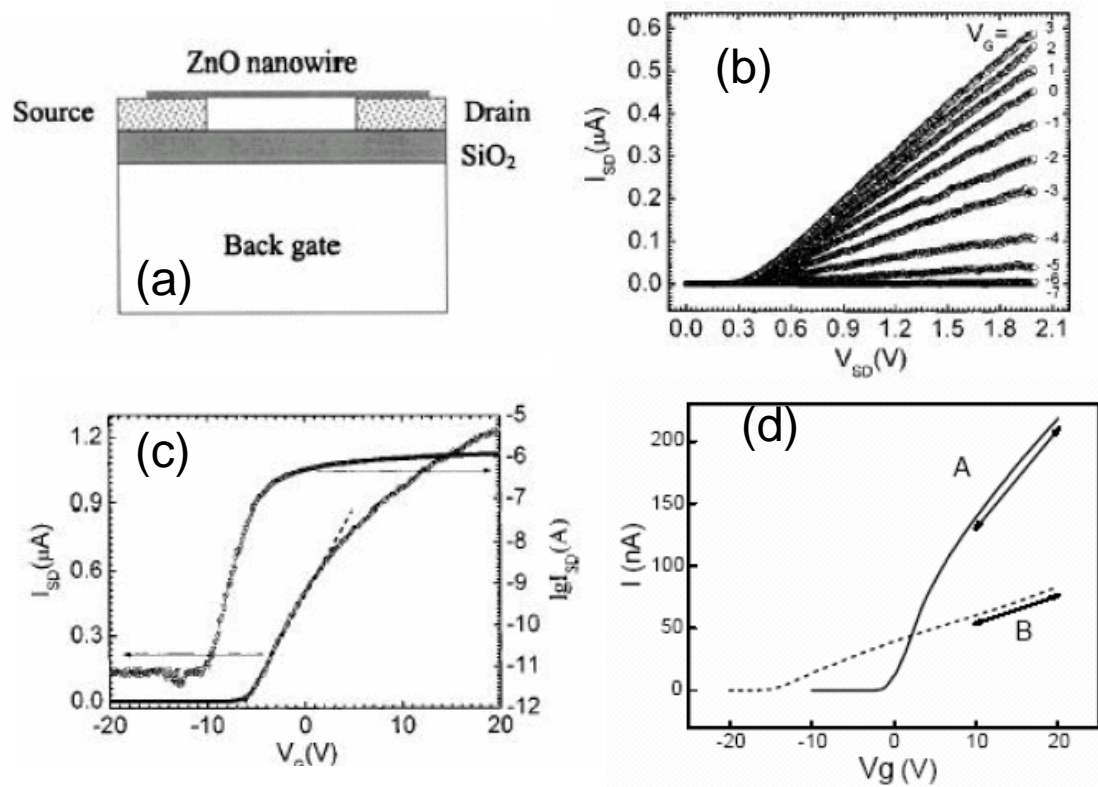


Figure 2.13: (a) Schematic of ZnO nanowire transistor, a single ZnO nanowire is connects to the two electrodes (source and drain) (b) I_{SD} - V_{SD} characteristics at different gate voltages as V_{SD} varies from 0 to 2V. (c) transfer characteristics as V_G varies from -20 V to 20 V at $V_{SD}=2\text{V}$ (d) Change of the transfer characteristics of two nanowires grown at the same time but different locations. Nanowire A has a mobility of $80\text{ cm}^2/\text{Vs}$ and carrier concentration $\sim 10^6\text{ cm}^{-3}$; and nanowire B has a mobility of $22\text{ cm}^2/\text{Vs}$ and carrier concentration $\sim 10^7\text{ cm}^{-3}$ [94, 95, 97, 99].

2.3.3 Optical properties of ZnO

ZnO exhibits a direct band gap of 3.37 eV at room temperature with a large exciton energy of 60meV. This exciton binding energy, which is much larger than that of GaN (25 meV), and the thermal energy at room temperature ($\sim 25\text{meV}$) can ensure an efficient exciton emission at room temperature under relatively low excitation energy. Especially, for wide band gap semiconductor materials, a high carrier concentration is usually required in order to reach an optical gain that is high enough for lasing action in an electron-hole plasma (EHP) process [103]. EHP is typically the key mechanism for conventional laser diode operation which needs high lasing threshold. However, an alternative to EHP is the excitonic recombination in semiconductors, which can facilitate a lower threshold stimulated emission. Due to the high density of free carrier trapping centers usually exist in wide-band-gapped semiconductors, the formation of electron-hole pair (exciton) allows more efficient radiative process [104, 105]. In order to form stable electron-hole pair at room temperature, the binding energy of the exciton must be larger than the thermal energy at room temperature, which is why ZnO is regarded as a good candidate for room temperature UV lasing. Indeed, when subject to the same excitation condition, the photoluminescence of ZnO is much more efficient than that of GaN at room temperature. Nanostructured materials are anticipated to further lower the lasing threshold since the quantum confinement effect will result in a substantial density of states at the band edges and enhance radiative recombination due to carrier confinement [16].

Photoluminescence (PL) spectra of ZnO nanostructures have been intensively studied. Park et al. have reported excitonic emission from the photoluminescence spectra of ZnO

nanorods [106]. Gu et al. studied the quantum confinement effect of one dimensional (1D) ZnO nanostructures, and shows that the binding energy of excitons in nanorods is significantly enhanced due to 1D confinement. The transition responsible for the “green band” often observed in ZnO is seems to be related to free holes [107]. Typical ZnO nanorods PL spectra shows fairly strong peak at 380 nm (3.26 eV) due to band-to-band transition, which is due to the near-band-edge free exciton emission (3.37 eV) of ZnO. Another green-red luminescence band centered at 650 nm (1.92 eV) is also observed, which is caused by native defect levels within the band gap, such as structural impurities, intrinsic defects due to interstitial Zn ions, ionized oxygen vacancies, and local levels composed by oxide antisite defect O_{Zn} . It has also been suggested that the green band emission is resulted from the singly ionized oxygen vacancy in ZnO and the recombination of a photogenerated hole with the singly ionized charge state of this defect [12]. The stronger the green luminescence, the more singly ionized oxygen vacancies exist in ZnO. Recently, red luminescence was also reported, which is contributed by doubly ionized oxygen vacancies [108]. Among those defect factors ionized oxygen vacancies is the most probably reason for causing the defects. Furthermore, the intensity of green emission increases with decreasing the diameter of the nanorods. This observation is contributed by the larger surface-to-volume ratio of thinner nanostructures favoring a higher level of defects and surface recombination [16,109]. Size reduction causes more atoms to be closer to the surface. Hence, as the diameter decreases, the surface approaches the bulk, providing a natural energy sink, where defects and impurities can be segregated. Below a certain size, the luminescence properties of ZnO nanostructures should be entirely dominated by the properties of the surface. In addition, as one of the characteristics of 1D nanostructure,

quantum confinement was observed to cause a blue shift in the near UV emission peak in ZnO nanobelts [110].

ZnO nanowires/nanorods photoresponse, photoresponse spectrum, and current-voltage (I-V) have also been studied for the investigation of photoconduction mechanism of ZnO. The photoresponse of the nanowires under the continuous illumination of light with above- or below-gap energies was slow, which suggests that photocurrent in the nanowires is surface-related rather than bulk-related [111]. The photoresponse spectrum represents the above- and below-gap absorption bands for the photocurrents. It is well known that ZnO films photoresponse shows a slow delay process in conduction which is controlled by surface effects. Since photoconduction of ZnO films is predominantly governed by adsorption and desorption of oxygen molecules.

The photoresponse measurement indicates that the creation of holes by the below-gap excitation as well as the above-gap excitation allows chemidesorption of oxygen to occur. Hence, the as-grown ZnO nanowires are connected between two electrodes for excited electrons to contribute to photoconduction. The photoconduction phenomenon in ZnO nanowires reveals that holes generated by both the above-gap and below-gap light discharge the negatively charged oxygen ions on the surface of the nanowires. The photoexcited electrons are trapped at some centers, and the electrons escaped from the centers transit to electrodes [111-113]. Keem et al. reported the photoresponse of the nanowires under the illumination modulated at different frequencies of 3, 10, and 30 Hz. The intensity of the photoresponse is independent of the illumination time, which indicates that the constant number of electrons arrive the electrodes per unit time during the illumination modulated at a fixed frequency [111].

Moreover, they also demonstrated that the intensity of the photoresponse is reduced with increased frequency, and no photoresponse was detected at frequencies higher than 100 Hz. This reveals that all electrons do not reach the electrodes within 1/100s after photoexcitation [111].

A comparison between photoresponse spectrum and photoluminescence spectrum of ZnO nanowires shows that the excitonic band is absent in the photoresponse spectrum even though the free-exciton PL peak is presented. This observation implies that excitons excited by the above-gap light in the ZnO nanowires do not contribute to the photoconduction, but the excitons participate in the recombination to emit the PL signal.

Keem et al. also shows that the I-V characteristics under the illumination of the above-gap light are ohmic, and the characteristics under the illumination of the below-gap are Schottky. This indicates that the above-gap light lowers the potential barrier built in the contact between the ZnO nanowire and electrodes, while the below-gap light does not. For ZnO film, the increase of electron density by photodesorption of oxygen adsorbed on the surface of the film narrows the width of the Schottky barrier formed between the film and contact electrodes. For ZnO crystallites, photodesorption of oxygens adsorbed on grain boundaries lowers the barrier height of the grain boundaries [112, 114]. The photodesorption of oxygens on the ZnO region contacting the metal may narrow the width of the Schottky barrier, or that the photodesorption may lower the height of the barrier. This can explain the ohmic behavior for the above-gap light; electrons may have a chance to tunnel through the narrowed width of the barrier. However, for the below-gap light, the efficiency of the photodesorption of oxygen is lower by four orders of magnitude compare

to the above-gap light. Consequently, the illumination of the below-gap shows Schottky characteristics [111].

2.3.4 Other properties of ZnO

Piezoelectricity is one of the important properties of ZnO that has been extensively studied for various applications such as acoustic wave resonators, force sensing, acousto-optic modulator, etc. The indigenoussness of the piezoelectricity lies in its crystal structure, in which the oxygen atoms and zinc atoms are tetrahedrally bonded. In such a non-centrosymmetric structure, the center of positive charge and negative charge can be displaced due to the lattice distortion induced by an external pressure. The displacement leads to originate local dipole moments; thus, macroscopic dipole moments appear over the whole crystal. Among the tetrahedral bonded semiconductors, ZnO has the highest piezoelectric tensor which provides a large eletro-mechanical coupling reponse[115]. Zhao et al. measured the piezoelectric coefficient of ZnO nanobelts by AFM conductive tips [116].

Another interesting phenomenon of the non-centrosymmetric ZnO structure is the spontaneous polarization and polar face dominated nanostructure. The tetrahedral bonds were stack at [0001] direction. Due to spontaneous polarization, the positive charge is displaced from that of negative charge and the direction of displacement is also [0001]. The net result of the spontaneous polarization is a charged (0001) ZnO surface; therefore, in order to achieve minimized energy, the charged (0001) surface results in unique nano-ring and nano-coil structure [117].

ZnO has also been found to be the promising host material for ferromagnetic doping. Ferromagnetism in ZnO nanowire was reported by Chang et al. Due to its wide band gap, ferromagnetic doped ZnO is recognized as an excellent material for short wavelength magneto-optical devices [118]. These investigations enable the use of magnetic ZnO nanowires as nanoscale spin-based device.

Functional metal oxide possess oxygen vacancies are electrically and chemically active. Oxygen vacancies serve as n-type donors which significantly increase the conductivity of oxide. Depends on the adsorption of charged accepting molecules at the vacancy sites, such as NO₂ and O₂, electrons are effectively depleted from the conduction band, which result in a decrease of surface conductivity. However, gases such as CO or H₂ would interact with surface oxygen and consequently remove it, leading to an increase of surface conductivity. Fan et al. reported the relationship between oxygen pressure and the performance of ZnO nanowire FET and showed that ZnO is relatively sensitive to O₂ [119]. The gas selectivity of NO₂ and NH₃ of the ZnO nanowire based FET was also been studied under the gate refresh process. Q1D ZnO nanostructures, such as nanorods and nanowires, have the small diameter comparable to the Debye length. Therefore, chemisorption induced surface states effectively affect the electrical structure of the entire channel, which leads the Q1D ZnO to be much more sensitive to chemical reaction, such as oxygen adsorption, than thin film [99]. The large surface-to-volume ratio of nanowires not only enhances their gas sensing performance, but also facilitates potential hydrogen storage property.

2.4 Growth techniques of ZnO

2.4.1 ZnO synthesis by metal organic vapor deposition

Metal organic chemical vapor deposition (MOCVD) is a widely used process for synthesizing semiconductor thin film, and has also been used for ZnO nanorod growth. Although ZnO thin film and quantum dots growth using MOCVD have been well-developed, MOCVD of ZnO nanorods was very recently developed. Yi and coworker used catalyst-free MOCVD for synthesizing nanorod and nanoneedle arrays [120]. MOCVD provides non-catalyst growth ZnO nanorods, which results in producing high purity ZnO nanorods and easy fabricated of nanorod quantum structures.

The catalyst free growth mechanism of ZnO nanorods has not been clearly investigated. The main reason for anisotropic growth is the anisotropic surface energy in ZnO. Moreover, high speed laminar gas flow in a certain growth condition may induce turbulent flow between the nanostructures, which results in adsorption of fresh reactant gases only on nanorod tips. Since more surface steps exist on nanorod tips, the nanorod growth rate is higher on nanorod tips than on side wall.

Figure 2.14 is the schematic of MOCVD setup. Diethylzinc (DEZn) is used as the zinc precursor and high-purity oxygen is used as the oxidizer [121]. DEZn is introduced into the reaction chamber using Ar carrier through a bubbling cylinder kept at constant temperature and pressure. Convective gas flow is suppressed by employing N₂ as the pushing gas forming an annular curtain gas flow around the reactor walls. DEZn and O₂ are separately introduced into the reactor through two nozzles and then mixed just above

the substrate surface to prevent possible gas phase reaction forming powdered by-products that may degrade the crystallinity of ZnO nanowires. The operating pressure is around 2-3.5 kPa and the substrate temperature needs to be held around 800-900K with a desirable growth duration.

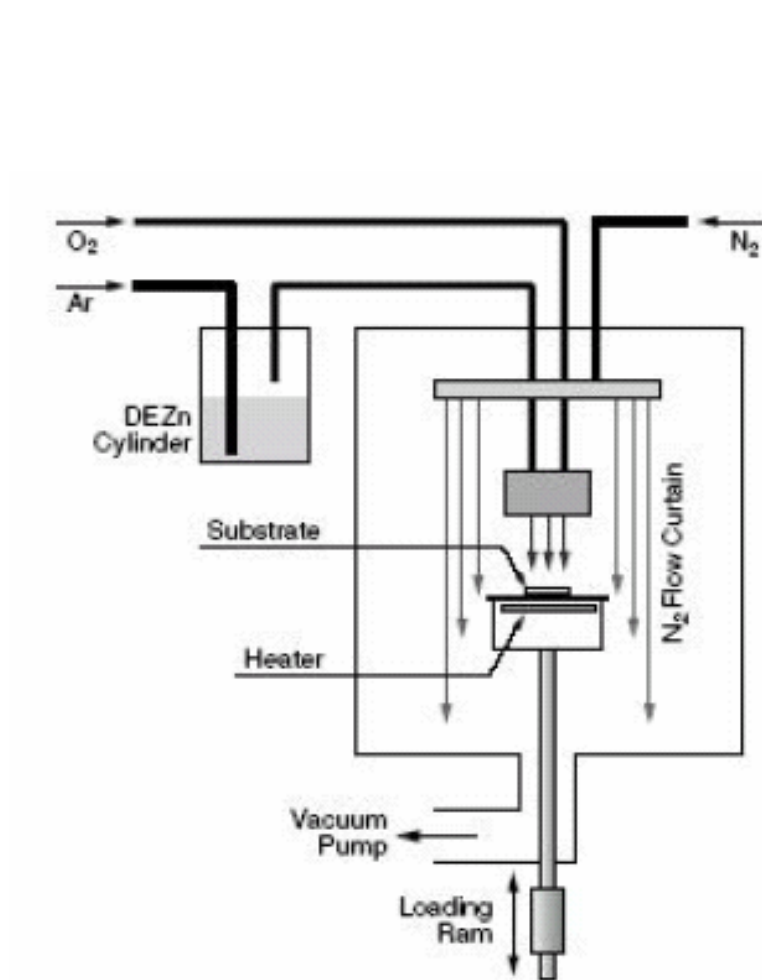


Figure 2.14: Schematic illustration of utilizing MOCVD for ZnO growth [121].

Park et al. have studied the morphology change with respect to the change of growth temperature (T_g) of MOCVD [122]. The morphology of ZnO change dramatically with T_g . At growth temperature lower than 200°C , no meaningful ZnO structure forms. At $200^\circ\text{C} \leq T_g \leq 260^\circ\text{C}$, columnar grained, textured ZnO films having a lot of crystalline defects grow. At higher growth temperature of $260^\circ\text{C} \leq T_g \leq 320^\circ\text{C}$, arrays of vertically well-aligned ZnO nanorods grow, and at further higher temperature of $320^\circ\text{C} \leq T_g \leq 380^\circ\text{C}$, ZnO of nanoneedle shape grows. Finally, at $T_g > 380^\circ\text{C}$, ZnO nanowire start to grow on top of a continuous ZnO layer. Figure 2.15 is the cross section SEM images of ZnO grown at different growth temperature [122]. T_g is one of the key processing parameters and it needs to be well-controlled in a narrow regime in order to grow desire ZnO nanostructures by MOCVD.

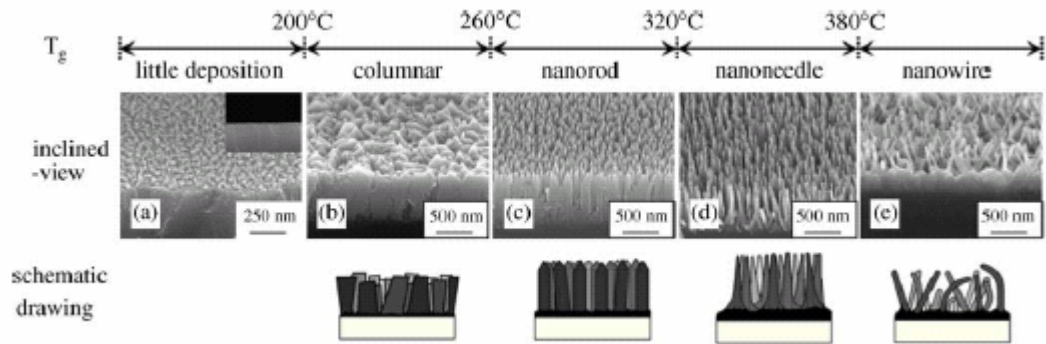


Figure 2.15: SEM cross section images of ZnO grown at various growth temperature (a) $T_g \leq 200^\circ\text{C}$, (b) $200^\circ\text{C} < T_g \leq 260^\circ\text{C}$, (c) $260^\circ\text{C} < T_g \leq 320^\circ\text{C}$ (d) $320^\circ\text{C} < T_g \leq 380^\circ\text{C}$, and (e) $T_g > 380^\circ\text{C}$. The ZnO morphologies grown at those temperature regimes are schematically described [122].

2.4.2 ZnO synthesis by pulsed-laser deposition

Pulsed-laser deposition (PLD) is a type of physical deposition, which is usually used for semiconductor thin film deposition. PLD have already been widely used for ZnO thin film deposition. Okada et al. reported a new method for synthesis ZnO nanorods by applying the basic idea of PLD, which is so-called nanoparticle-assisted pulsed-laser deposition (NAPLD) [123]. NAPLD, a non-catalyst growth method, is the method that the species created by laser ablation are firstly converted into nanoparticles by the condensation in the background gas. Then, formed nanoparticles are transported onto a heated substrate where nano-structured crystals are synthesized. Since the nanoparticles require a lower melting temperature than the same bulk form; therefore, the ZnO nanostructures can be synthesized at a relatively lower substrate temperature.

A sintered ZnO target or a metal Zn target, which serves as the source for ZnO deposition, was ablated using a KrF excimer laser. KrF excimer laser operates at a repetition rate of 20 Hz and a fluence of about 3 J/cm² in a chamber filled with oxygen background gas [124]. ZnO thin films have been successfully synthesized in an oxygen background gas at a relatively low pressure (approximately 0.1 Torr or less). However, for NAPLD, ZnO nanostructures are synthesized in oxygen or He background gas pressure in a range from 1 to 10 Torr. Figure 2.16 shows the schematic of the growth model of crystals by NAPLD which can briefly explain the initial growth condition of ZnO nanostructures [125].

As the nanoparticles formed by condensation of ablated species in gas phase try to deposit on a low temperature (~400°C) sapphire substrate, the film is made up of randomly

aggregated particles. It is suggested that these particles are the trace of the aggregated nano-particle in the background gas that can be obviously detected by Rayleigh scattering technique. If the nanoparticles were deposited on a high temperature ($\sim 700^{\circ}\text{C}$) substrate, hexagonal ZnO nanocrystal will be uniformly observed and there is no trace of particles. Moreover, if the substrate temperature was decreased down to 300°C after the deposition at high temperature, the particles were observed to be randomly stuck on the nanorods that are deposited at high temperature. Substrate temperature is a key parameter for growing nanostructures by NAPLD [123-125].

Not only substrate temperature, but also O_2 background gas pressure and target substrate distance affects the nanostructure growth. Micro-sized hexagonal crystals on a uniform film are often synthesized at the pressure below 0.1 Torr. At diverse O_2 pressure from 0.1 to 10 Torr while the substrate temperature was kept constant, the small size crystals have been found at a pressure of 1 Torr. The rod size becomes larger with the increasing pressure. When the pressure is increases above 10 Torr, rods fused each other and the top surfaces of the rods become flattened. The reason why the structure change with the changing background pressure has not been yet understood; however, it must be corresponded to the formation of nanoparticles in the gas phase. At a constant O_2 pressure, the rods become thinner as the substrate-target distance increases In summery, ZnO nanostructures can be tuned by suitably adjusting the O_2 pressure, substrate temperature, and substrate-target distance; however, the basic growth mechanisms have not been clarified yet [123-125].

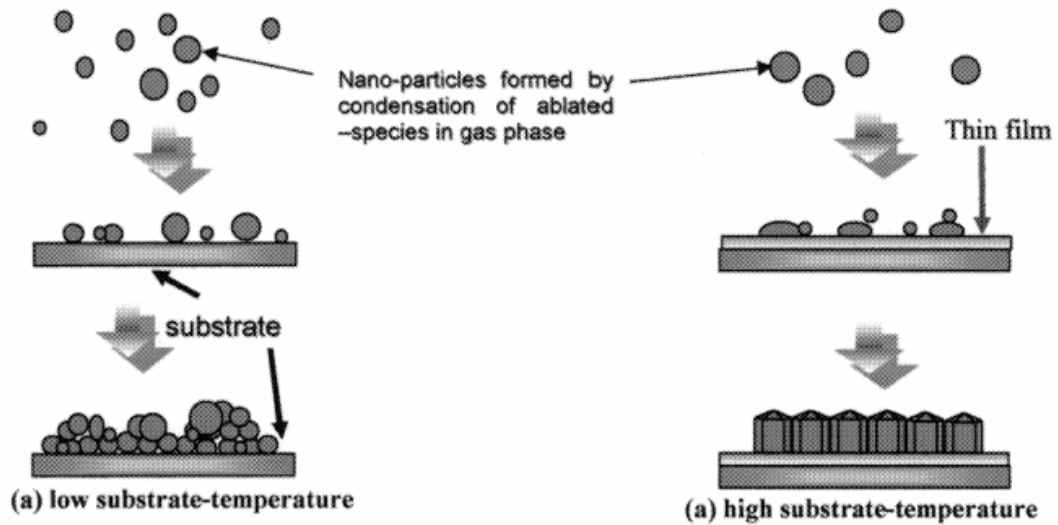


Figure 2.16: Growth model of NAPLD (a) at low substrate temperature (b) at high substrate temperature [125].

2.4.3 ZnO synthesis by vapor transport

The growth of ZnO nanostructured materials have been carried out by various approaches, such as chemical vapor deposition, physical vapor deposition, molecular beam epitaxy, and thermal evaporation. All these methods induce vapor transport and vapor-liquid-solid (VLS) mechanism for nanowire, in which a metal or oxide catalyst is necessary to dissolve feeding source atoms in the molten state to initiate the growth of nanostructured materials [126]. Vapor phase transport means that vapor species are first generated by elevated temperature, chemical reduction and gaseous reaction. These source species are subsequently transported and condensed onto the surface of a solid substrate

placed in a zone with a temperature lower than that of the source material. A large quantity of 1D nanostructures can be obtained by properly controlled over the supersaturation factor.

Vapor transport techniques can be divided into catalyst free vapor-solid (VS) process and catalyst assisted vapor-liquid-solid (VLS) process. VS process usually synthesizes a rich variety of nanostructures, including nanowires, nanorods, nanobelts and other complex structures [99]. In this process, ZnO powder was decomposed into Zn^{2+} and O^{2-} at $\sim 1350^\circ C$, the nanostructures are produced by condensing ZnO directly from vapor phase. Yao et al. demonstrated that temperature is a critical parameter for the formation of different morphologies of ZnO nanostructures by thermal evaporation methods [127]. Figure 2.17 is the result of different nanostructures carried out at different temperatures. Wan et al. reported a method of rapid heating zinc pallet at $900^\circ C$ in air ambient, which is typically generates tetrapods like ZnO structure [128, 129].

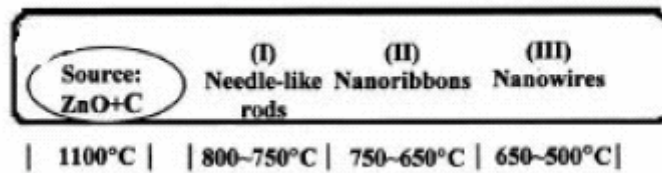


Figure 2.17: Schematic of different ZnO nanostructures growth at different temperature zone [127].

VS method obviously provides less geometry control, alignment and precise location of ZnO nanostructures. More controllable growth of ZnO nanostructures can be achieved by catalyst assisted VLS process. However, different kinds of substrates have different lattice

mismatch values, which is the key processing parameter for either VS or VLS growth. Table 2.8 lists the lattice mismatch of different substrates with respect to ZnO [99]. In VLS process, several nanoparticles have been used as catalyst, such as Au, Ni, Cu, and Sn, etc. Figure 2.18 shows the schematic of a typical VLS method [99]. The formation of eutectic alloy droplet occurs at each catalyst site, followed by the nucleation and growth of crystalline ZnO nanowire due to the supersaturation of the liquid droplet. Incremental growth of the nanowire taking place at the droplet interface constantly pushes the catalyst upwards. Such growth method inherently provides site-specific nucleation at each catalyst site. In a VLS synthesis process Zn powder is used as the source material. The substrate is coated with Au particles with diameters of tens of nanometers and located adjacent to the source. The source and substrate are heated up above the melting point of Zn powder (419°C) accompanied with appropriate low concentration of O₂ flow, resulting in the growth of high quality ZnO nanowires.

There are several controllable parameters such as temperature, pressure (environment pressure and wafer (local) pressure), carrier gas (gas species and its flow rate), substrate and evaporation time period, which can be controlled and need to be selected properly before and/or during the evaporation. The selection of source temperature depends on the volatility of the source material. The pressure is determined according to the evaporation rate or vapor pressure of the source material [12]. The substrate temperature usually drops with the increasing distance of its location from the position of the source material. The local temperature determines the types of product that are originated. Finally, oxygen concentration is also a key point for ZnO growth; oxygen affects not only the volatility of

the source material and the stoichiometry of the vapor phase, but also the formation of the products.

Material	ZnO	GaN	Sapphire	SiC	Si
Crystal structure	Wurtzite	Wurtzite	Hexagonal	Wurtzite	Diamond
Lattice constant (nm)	a=0.325 c=0.521	a=0.319 c=0.519	a=0.475 c=1.299	a=0.309 c=1.512	a=b=c =0.543
Epitaxial plane	(0001)	(0001)	(11 $\bar{2}$ 0)	(0001)	(100)
Lattice Mismatch	0	1.9% [70]	0.08% [70]	5.5% [47]	18.6% [67]

Table 2.8: Lattice parameter of several epitaxy substrates [99].

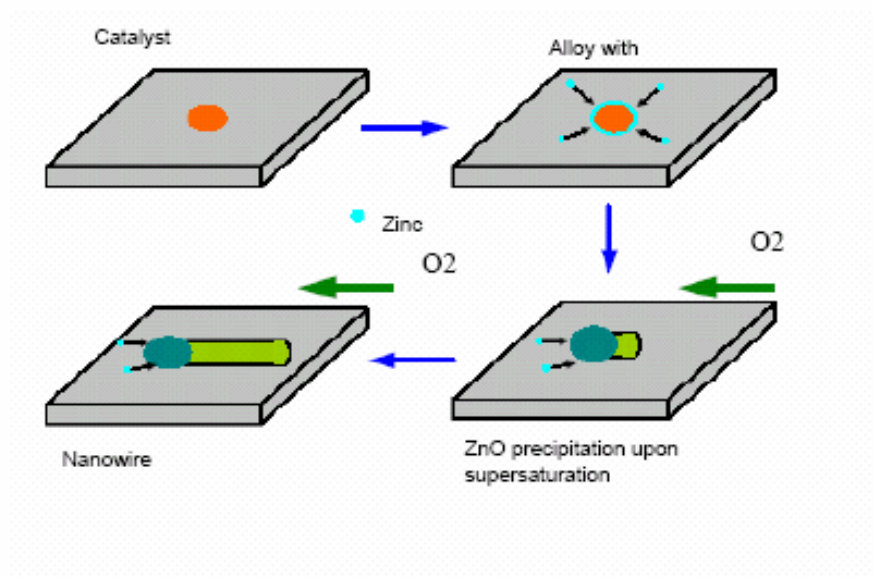


Figure 2.18: Schematic of ZnO nanowire growth by VLS process [99].

2.5 Field Emission of Electrons from Solid Surface

2.5.1 Field emission from metal surface

Electron field emission is defined by the electrons are extracted from a cold solid surface by overcome the surface potential barrier when a negative electric field is applied to the solid. Fowler and Nordheim succeeded in applying wave-mechanical methods to the basic theoretical considerations of electron emission from metals under the influence of an external electrical field [130]. There are some assumptions for this theoretical model, (1) A simple one-band electron distribution using Fermi-Dirac statistics; (2) A smooth, plane metal surface where irregularities of atomic dimensions are neglected; (3) A classical image force; (4) an uniform distribution of work function. The field emission current density can be derived based on the four assumptions, results in

$$J = A(F^2 / \phi) \exp(-B\phi^{3/2} / F) \quad (2.21)$$

where $A = 1.56 \times 10^{-10}$ (AV^{-2}eV), $B = 6.83 \times 10^3$ ($\text{VeV}^{-3/2}\mu\text{m}^{-1}$), ϕ is the work function of the barrier that has the unit of eV, F is the applied electric field (V/cm), and the current density J is in A/cm^2 . Theoretically, the Fowler-Nordheim theory is applicable only for $T=0\text{K}$. However, formula (2.21) is still valid even when $T>0\text{K}$, as long as $kT \ll \phi$. Since rarely of thermal excitation of electrons diffuses the Fermi level at room temperature; hence, formula (2.21) remains valid.

V is the potential difference applied between two planar electrodes separated by a gap distance of d . The macroscopic electric field is found to be $E=V/d$. However, if the

electrode surface is not ideally smooth, for example, for a sharp needle, the local electric field on the tip is much stronger than the macroscopic field by a factor of β , so-called the field enhancement factor. The local electric field at the emitter surface can be expressed as

$$F = \beta E = \frac{E}{kr} \quad (2.22)$$

where E is the macroscopic electric field between anode and cathode, β is a function of the geometrical shape (geometrical factor); r is the radius, and $k \sim 5$ at the acme of the emitter.

Equation (2.21) can be rewritten as

$$J = A(\beta^2 E^2 / \phi) \exp(-B\phi^{3/2} / \beta E) \quad (2.23)$$

when the local electric field is high enough such that the potential barrier is comparable to the wavelength in the solid, electron tunneling through the surface barrier become important. The emitted electrons are mostly come from the Fermi level and are affected by the work function of the solid ϕ . The total current I as a function of the macroscopic electric field can be derived out as

$$I \propto (\beta^2 E^2 / \phi) \exp(-B\phi^{3/2} / \beta E) \quad (2.24)$$

The relationship above is called the Fowler-Nordheim equation. When $\ln(I/E^2)$ is plotted versus $1/E$ (Fowler-Nordheim plot), a straight line with a slope s that depends on ϕ and β is obtained as

$$s = -B\phi^{3/2} / \beta \quad (2.25)$$

Therefore, the field enhancement factor β can be calculated from the slope if the work function of the tip is known.

2.5.2 Field emission from semiconductor surface

An internal electrical field complicates the problem of electron field emission of semiconductors. This can be explained by the penetration of an external electrical field into the semiconductor surface, by surface state, and by the field emission current through the emitter. Electric field penetrates into a semiconductor results in the indeterminacy of forces acting on an electron at the surface of the body, and downward bending of the energy bands at the surface of the body. The downward bending is prescribed by the particular polarity of the emission field (Figure 2.19a).

The existence of surface states in a semiconductor is usually accompanied by an internal retarding field, by an additional potential barrier at its surface (Figure 2.19 b). An internal barrier reduces the field emission because it decreases the concentration of electrons on the surface layer. In contrast with metal where electrons from conduction band are emitted, field emission of semiconductor is further complicated by the fact that electrons may be emitted from both the conduction and valence band.

At present, there is no complete theory of semiconductor field emission. Experimentally in most case, only $\log I$ vs. $1/V$ (I is the emitted current from the total emitting area, V is the voltage applied between the emitter and the anode) which is called Fowler-Nordheim plot, was usually plotted. Experimentally, Ge crystal with different doping concentration suggested that the emission from all n-type crystals leads to a linear slope in all cases of the plot of $\log I$ vs. $1/V$ [149]. The internal retarding field drop is relatively small compared to the anode voltage. However, above some particular field, which depends on temperature and illumination, the current becomes almost independent of the applied electric field.

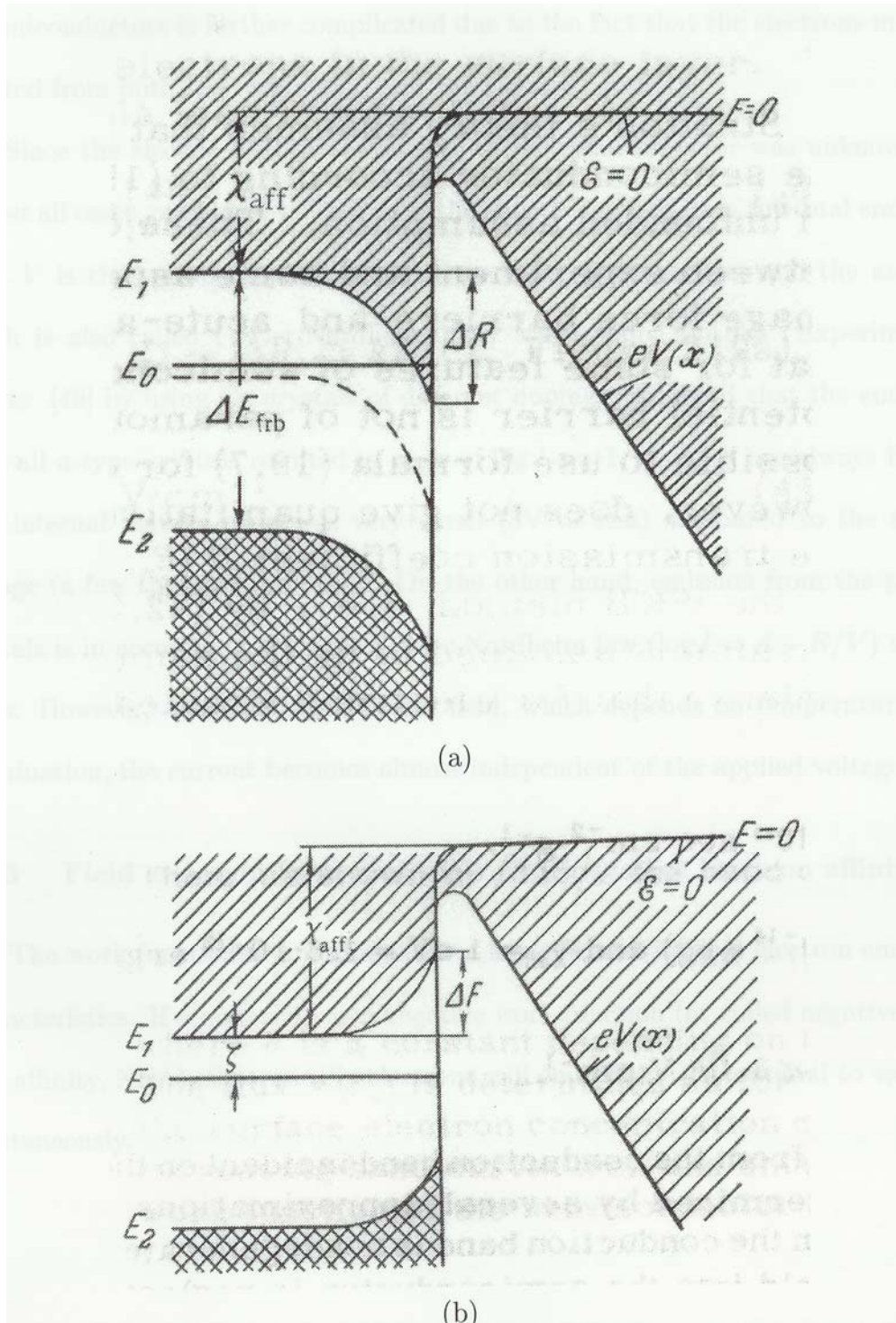


Figure 2.19: (a) Schematic diagram of the band bending near the semiconductor surface by strong electric field (b) An internal barrier generated by an internal retarding field. [142]

Electron field emission for display applications has better advantages over conventional thermionic electron emission. First, the field emitters that provide electron sources do not need to be heated. Therefore, it can eliminate the need for a heating source and circuitry. Second, the energy spreading of the electrons emitted from a field emitter is much smaller than that from a thermionic emitter. Finally, the emission currents from the field emitters can be precisely controlled with controlling the applied voltage.

2.5.3 Field emission from carbon nanotube

Carbon nanotubes have high conductivity and sharp tip with long and narrow shape which are useful for field emission. Recently, there have been growing interests on the development of field-emitting cathodes by carbon based material, for a versatility of potential microelectronic and display applications. Table 2.9 shows a summary of typical values of threshold electric field encountered in flat panel display application for several different materials [141]. The definition of threshold electric field, in the case of flat panel display application, is the electrical field needed to originate a current of $10\text{mA}/\text{cm}^2$.

So far, carbon nanotubes are reported to exhibit excellent behavior for electron field emission. . The field emission behavior of CNTs is observed at fields lower than $1\text{ V}/\mu\text{m}$. They have the turn-on electric field at $5\text{ V}/\mu\text{m}$, typically, and high current densities of over $1\text{A}/\text{cm}^2$. The emission current was also reported to be relatively stable, without any obvious degradation after a few hundred hours of aging in vacuum. Dean et al. reported a significant phenomenon that in most case, the electron emission was the resonant tunneling of electrons from the carbon nanotube through a molecule adsorbed on the tip [131]. The

adsorbate gives a lower on-set electric field, which indicates that carbon nanotube starts to emit electron more easily with the presence of adsorbate. However, adsorbate on nanotubes causes early emission current density saturation because of transmission through the adsorbate.

Single tube emission current is constrained due to its ultra small dimensions, but this problem can be surmounted by using a large area array of vertically aligned nanotubes or nanotube film. However, a high density of nanotubes at the substrate surface does not provide high emission site density during field emission. This can be realized in terms of the screening out of the electric field by too many nanotubes. Neighboring nanotubes screen the electric field of each other; therefore, the enhancement factor is reduced. The aspect ratio and tip sharpness are not the only factors that determine whether a carbon nanotube film will exhibit good emission characteristics. An important factor affecting the field emission properties is field screening.

Material	Threshold field ^a (V/ μ m)
Mo tips [1]	50–100
Si tips [1]	50–100
p-type semiconducting diamond [22]	160
Undoped, defective CVD diamond [22]	30–120
Amorphous diamond [6]	20–40
Cesium-coated diamond [27]	20–30
Graphite powders (< 1 μ m size) [28]	17
Nanostructured diamond particles [25]	
As-coated	Arcing-no emission
Heat-treated in hydrogen gas	Arcing-no emission
Heat treated in hydrogen plasma	3–5
Carbon nanotubes (both SWNTs and MWNTs)	1–5

Table 2.9: Emission threshold electric fields for various emitter materials [141].

Carbon nanotubes which are perpendicular to the substrate surface are considered to be the most optimum emitting sources. However, even in this configuration, the density of emitting tips ($\sim 10^5 \text{ cm}^{-2}$) is only a small fraction of the nanotube density (10^8 cm^{-2}) [132]. Only the tubes that are perpendicular to the substrate with sharp tips or those tubes protrude out of the surface emit efficiently. The emission of randomly oriented carbon nanotubes under low electric field is dominated by a certain amount of nanotubes that have perpendicular orientation to the surface of the film [133]. At high electric field, loops of nanotubes might also contribute to field emission. The emission site density increases with increasing electric field that applied due to the nanotubes with loose end intend to align each other by the outer strong electric field. Those tubes which are bent by the strong electric field will emit electrons from the loose end of the nanotubes, which are stick out of the surface. The typical field enhancement factor for SWCNT and MWCNT have been carried out by F-N slope experimentally. Base on the assumption that the work function is 5eV, for a single MWCNT the field enhancement factor is ranged form 30000 to 50000 and 1000 to 3000 for MWCNT film. The turn-on and threshold electric field are 2.6 V/ μm and 4.6 V/ μm , respectively, for a typical MWCNT film. For SWCNT film, it exhibits to have the field enhancement factor of 2500 to 10000, and the turn-on and threshold electric field are 1.5-4.5 V/ μm and 3.9-7.8 V/ μm , respectively [134, 135]. The field enhancement factor for SWCNT is significantly higher than MWCNT which is probably due to the smaller tip radius and the smaller curvature radius of SWCNTs.

Current stability and degradation are also very important factors for display applications. For nanotubes, regardless of SWCNTs or MWCNTs, a gradual degradation with time under high vacuum of the emission performance has been observed. The degradation is

probably caused by the ion bombardment of gas phase electron ionization or by ion desorption from the anode, both are induced by the emitted electrons. Generally, SWCNTs show faster degradation rate than MWCNTs [136]. The pressure during the emission test shows great effect on current stability and degradation due to the excess residual gas molecules in the chamber. The tips of nanotubes will be destroyed by the gas molecules that ionized during aging process. Therefore, emission is more stable under high vacuum.

Carbon nanotubes for electron field emission applications have also been reported recently. Carbon nanotubes for flat panel display were proposed in 1995 to be the most promising field emission display [132], and the group in Samsung produced a fully sealed 4.5 inch three color field emission display in 1999 [137]. Other application, such as using carbon nanotubes for lighting elements [138], microwave tubes [139], and X-ray tubes [137, 140] have already been demonstrated.

2.5.4 I-V instabilities and arcing protection

Field emission cold cathodes in low power applications are hurdle of obtaining stable and reproducible emission characteristics. The problems that cause the degradation and premature failure of field emission cold cathodes are ion bombardment due to the residual gas molecules ionization of poor vacuum, arcing, resistive heating of emission site, and surface migration. Arcing failure, which is the major obstruction for field emission to utilize in high current applications, has been recognized to be originated by ionization of gas molecules and/or desorbed contaminants.

Some efforts have been carried out to stabilize the I-V characterization of field emission such as passive resistor stabilization, active transistor cathode current limiting, and closed loop stabilization. Long life time of current stability has been greatly resolved for applications such as flat panel display by using integrated passive resistors that provide current limiting.

CHAPTER 3
SPECIMEN PREPARATION AND CHARACTERIZATION

3.1 Growth process

3.1.1 ZnO nanostructures growth

ZnO nanoneedles were synthesized by catalyst-assisted thermal evaporation method. Figure 3.1 shows the schematic diagram for the thermal CVD reactor used for synthesis ZnO nanoneedles. A resistive heater is used to heat the outer and inner quartz tubes and the substrate inside the inner quartz tube. A thermocouple is located closed to the inner quartz tube in order to precisely measure the reaction temperature. The pressure in the quartz can be controlled by a manually throttle valve or a exhaust valve controller, which is connected to a mechanical pump, and a manometer pressure gauge. Ar (carrier gas) and O₂ (reactant gas) are introduced into the tube precisely by using mass flow controllers to control the amount of flow rate.

Different kinds of ZnO nanostructures were obtained by adjusting the thermal CVD conditions, such as gas pressure, furnace temperature, gas flow rate, reaction period, wafer (local) pressure etc.

A n-type <100> silicon (Si) wafer was cleaned by the RCA wafer cleaning process, dipped in deionized water (DI) for 15 min, and then dried by flowing nitrogen. After the

cleaning procedures, a few drops of liquid catalyst solution would be placed on the surface of the Si wafer. The wafer was left in air ambient to dry. The liquid catalyst solution consisted of nickel chloride hexahydrate (99.9999%, $\text{NiCl}_2 \cdot 6\text{H}_2\text{O}$) diluted in ethanol with a weight ratio of 1:100. An alumina boat, $10 \times 1.5 \times 1 \text{ cm}^3$ in size, was used to load the Si wafer. A small amount of Zinc (Zn) powder (99.998%) was put underneath the Si wafer with a 0.5cm gap distance between the Zinc powder and the silicon wafer at the bottom of the alumina boat. The alumina boat was then loaded into the center of a quartz tube furnace. The Si sample was heated up to 550°C with a constant flow of 500 sccm argon. The reaction time was 30 min at 1 atmosphere gas pressure. After the deposition completed and the furnace was cooled down, the sample was unloaded from the quartz tube with a white wax-like material deposited on it.

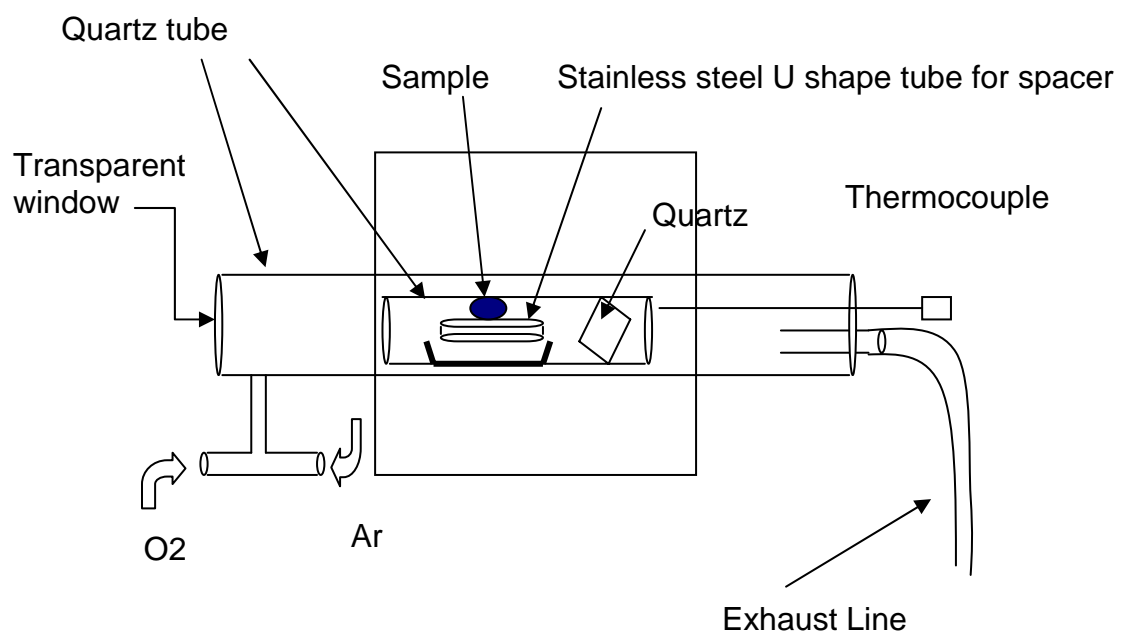


Figure 3.1: Schematic diagram for thermal CVD ZnO nanostructures growth.

3.1.2 Carbon nanotubes growth

Vertically aligned MWCNTs were synthesized by means of thermal chemical vapor deposition. The Si substrate was cleaned by the same procedures described above. The Si substrate was sputter deposited with titanium (Ti), Si, and iron (Fe) sequentially using electron beam evaporation or DC sputtering [143]. The Ti layer provides good adhesion of the metal coating on the substrate. A few nanometers thick of silicon layer was deposited on top of the titanium before an iron thin coating was deposited on top of titanium. The substrate was loaded into the furnace, heated to 700°C and stay there for 10min with the feed gas mixture of acetylene (C₂H₂) and argon (Ar) at a constant gas pressure of 75 Torr inside the quartz tube (Figure 3.2).

Vertically aligned SWCNTs were grown by the same method as MWCNTs but with different catalyst layer preparation processes. The catalyst layers for SWCNTs [144] were composed of Al (aluminum)/Fe/Al. The first layer of 5nm thick Al was deposited by electron beam evaporation. The first layer Al was oxidized for 12 hrs at 75°C on a hot plate in air in order to generate uniform and dense nucleation sites. The oxidation process was to allow the aluminum to form aluminum oxide as a support for the subsequently deposited iron catalyst thin coating. A Fe layer was sputter deposited by a DC-magnetron sputtering gun at a low power level of about 20W~40W to obtain an ultra thin layer of Fe (approximately 0.5nm) to be used as the catalyst for SWCNTs growth. The third layer of Al was also deposited using a DC-magnetron sputtering gun to obtain an ultra-thin layer for catalyst support. The growth process and parameters for SWCNTs are the same as that for growing MWCNTs.

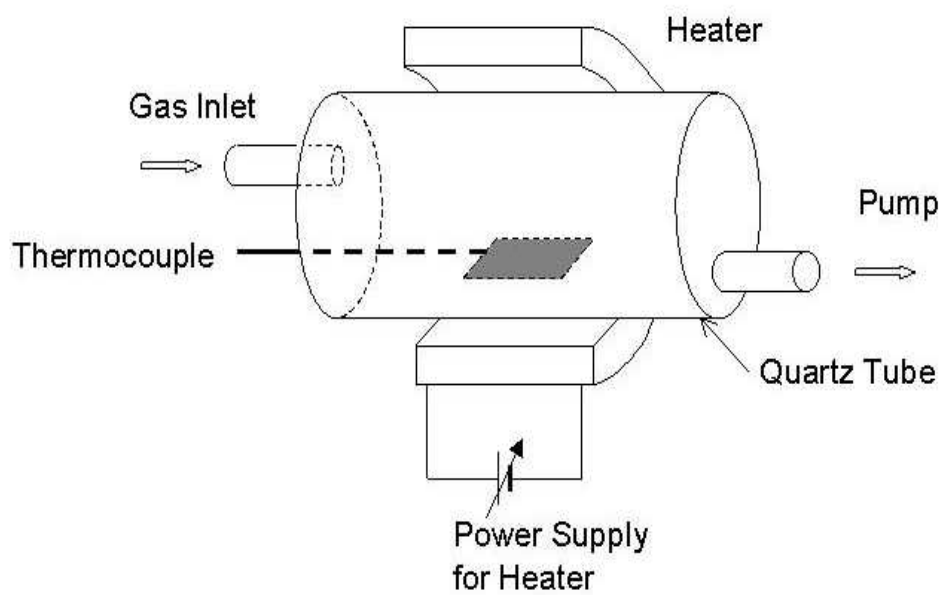


Figure 3.2: Schematic diagram for thermal CVD carbon nanotubes growth [143].

3.2 Electron field emission measurement and setup

The samples are loaded into a high vacuum chamber in which the electron field emission characterizations of the samples are measured. The chamber is first pumped by rotary mechanical pump to the pressure of several mTorr, the turbomolecular pump is turn on after the pressure reach mTorr range. The field emissions perform when the chamber pressure was lower than 1×10^{-6} Torr. Alumina oxide disks of 60 μm thick served as spacers between the anode and the cathode. The gap spacing used for ZnO nanoneedle measurements was 120 μm (two alumina oxide disks) and that for CNT measurement was 60 μm , respectfully.

The anode used for collecting electron field emission current was inserted inside an electrically insulating machinable ceramic block with the surface of the anode aligned with the surface of the ceramic block. The area of the anode is 1cm in diameter. A tungsten rod with hemispherical is attach on the top surface of the anode block in order to more precisely align and fix the anode. Spacers are placed between the cathode and the electrically insulating ceramic block so that in case the side walls of the spacers are coated with conducting materials, there will not be leakage current between the anode and the cathode through the conductive side walls of the spacers.

Initial FE measurements were done with a background pressure of $\sim 1 \times 10^{-6}$ Torr at room temperature. Ambient air was leaked intentionally and under control into the chamber up to a pressure of 60 mTorr by means of a needle-valve and an air leak valve. The air was leaked into the chamber step by step from low pressure ($< 2 \times 10^{-6}$ Torr) to allow FE measurement at different air pressures. After all the measurements were done with

leaked air, the test chamber was evacuated to the initial vacuum level to examine whether the FE properties could recovery to the original level measured in good vacuum.

A digital dc power supply (Stanford Research Systems PS235) is used to apply a voltage between the anode and cathode. A Keithley 485 picoammeter is used to measure the emission current. By using a GPIB card, the power supply and the ammeter can be controlled by a desktop computer, by which voltage and current is recorded for further evaluations (Figure 3.3).

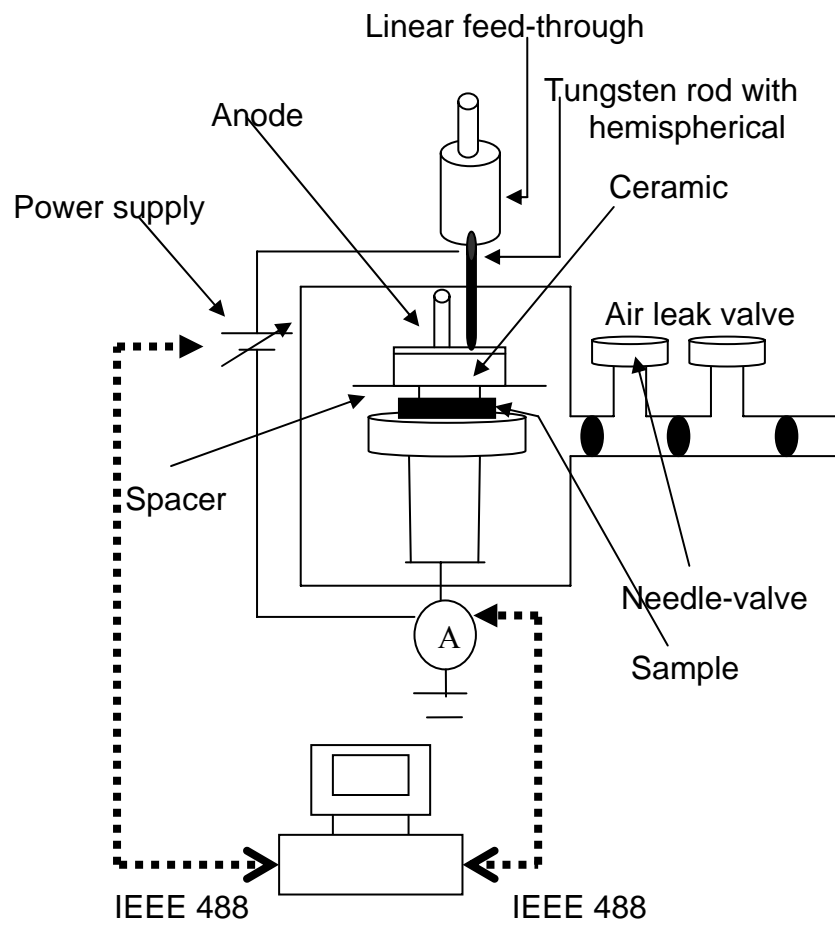


Figure 3.3: Schematic diagram for the field emission measurement setup.

CHAPER 4

RESULTS AND DISCUSSION

Vertically aligned single-walled and multi-walled carbon nanotubes were successfully deposited on silicon substrate by thermal CVD. Several ZnO nanostructures were also prepared by tuning the processing parameters during thermal evaporation. The field emission characterizations of carbon nanotubes and ZnO nanoneedles samples were performed and analyzed.

Effects of gas pressure on the electron field emission (FE) properties of ZnO nanoneedles and carbon nanotubes were investigated. Reversibility and sensitivity of the FE of ZnO and CNTs to air pressures were studied for potential applications such as field emission display (FED) and vacuum microelectronic devices. The pressure-dependant, time-dependant, and pressure-time-dependant field emission behaviors of ZnO nanoneedles and CNTs will be compared and discussed.

4.1 Growth of carbon nanotube and its field emission

4.1.1 Growth and field emission property of multi-walled carbon nanotubes

Since the surface of polysilicon (~400 μ m thick) is too rough that is relatively difficult to synthesize high-density or well-aligned carbon nanotubes on top of it. Hence,

transition metal catalyst thin film is deposited directly onto the polysilicon surface to solve the surface roughness and lattice mismatch problems. Moreover, the adhesion of nanotubes to polysilicon is poor. On the other hand, with the improvement of Ti adhesion promotion layer and the silicon buffer layer, high density carbon nanotubes can be easily grown on the polysilicon surface. Figure 4.1 is the SEM picture of vertically aligned high density multi-walled carbon nanotubes [143].

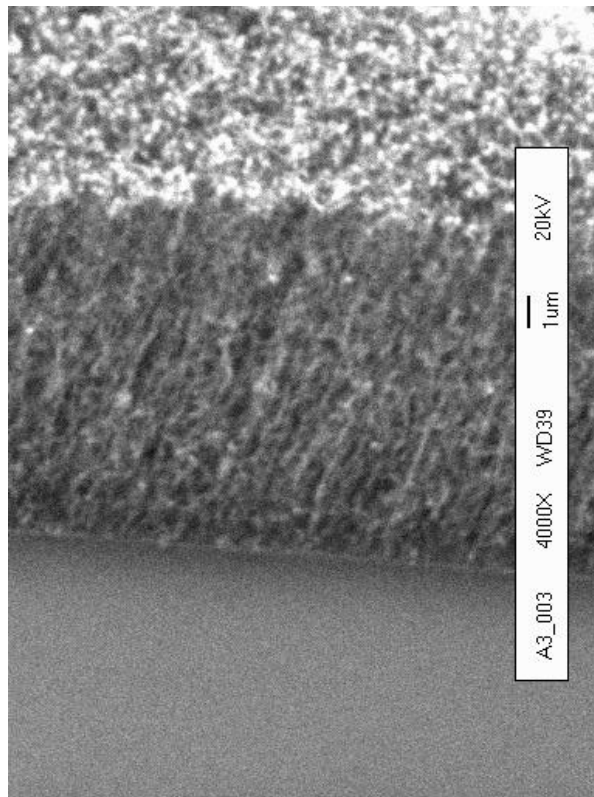


Figure 4.1 SEM image crosssectional view of the side wall of multi-walled carbon nanotubes [143].

The length of MWCNTs was approximately $60\mu\text{m}$. The sample was densely covered with MWCNTs. Figure 4.2 is the transmission electron microscopy (TEM) image for this MWCNTs sample. The TEM image shows that a few nanotubes attach to the same large particle with a diameter of $\sim 80\text{ nm}$, which is believed to be a piece of titanium layer that peeled off from the substrate. This indicated that the roots of carbon nanotubes bond strongly with the Ti layer underneath them.

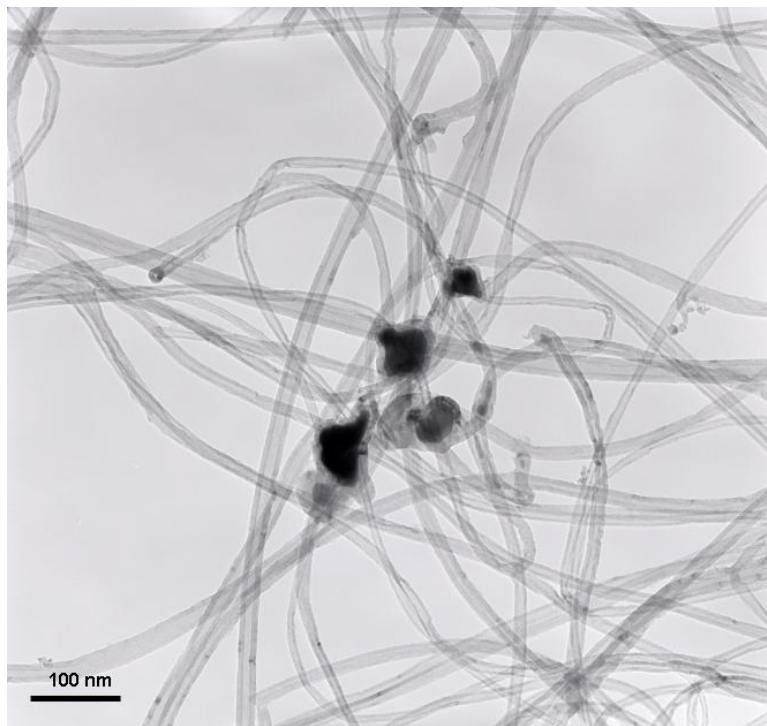


Figure 4.2 TEM photograph of multi-walled carbon nanotubes on silicon with e-beam evaporation of Ti/Fe/Si metal catalysts. The magnification is 100k [143].

Field emission measurement of multi-walled carbon nanotubes was first performed at 2×10^{-6} Torr with the gap spacing of $60\mu\text{m}$. Figure 4.3 shows the typical field emission of multi-walled carbon nanotubes under high vacuum with the voltage scanned from 0 to 600V. The electron started to emit at the electric field about $1.2\text{ V}/\mu\text{m}$. The turn-on

voltage is determined at the current reaches 10^{-7} A, which indicated the turn-on voltage of multi-walled carbon nanotubes is about 2 V/ μm . Therefore, these nanotubes are very efficient for cold cathode electron emission.

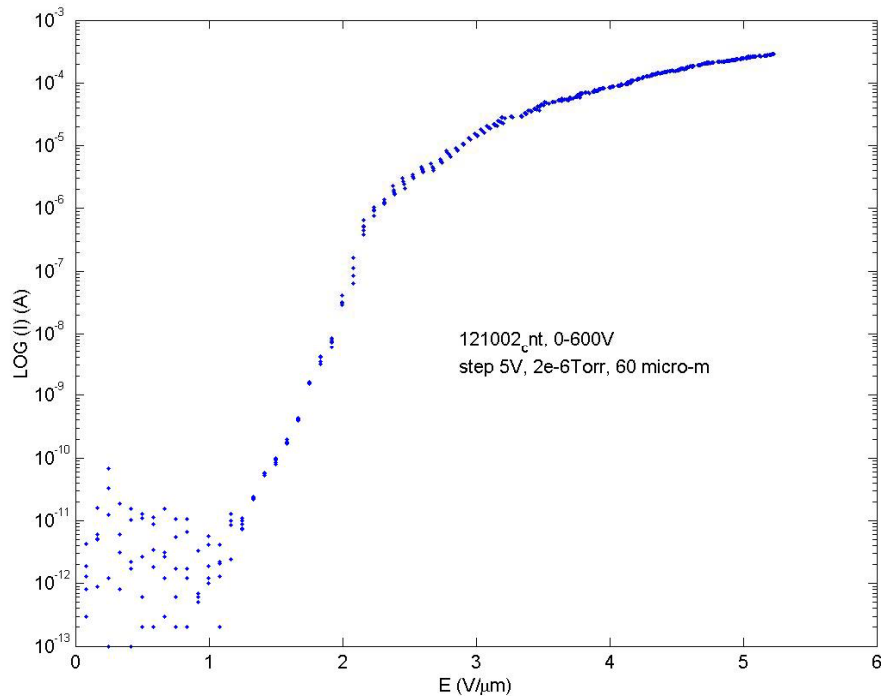


Figure 4.3: Field emission measurement of multi-walled carbon nanotubes.

4.1.2 Growth and field emission property of single-walled carbon nanotubes

The catalyst layer for SWCNTs is a sandwich structure, Al/Fe/Al. Since Al was first deposited on the silicon substrate with further oxidation in air, which allows the Al thin film ($\sim 5\text{nm}$) to separate into small pieces of islands, is the adhesion and support layer for Fe catalyst to be deposit on top of it. An ultra-thin layer of Fe ($\sim 5\text{\AA}$) was deposited on top of the Al oxide layer, which is anticipated that SWCNTs or SWCNTs bundles would be

grew due to the ultra small size of catalyst. After depositing the Fe layer, an ultra-thin layer of Al ($\leq 5\text{\AA}$) was deposited on top of the Fe layer in order to confine the Fe nanoparticles and also confine the growth direction. Figure 4.4 (a) shows the cross-sectional image of SWCNTs taken by scanning electron microscopy (SEM). A silicon substrate was densely and uniformly covered by vertically aligned SWCNTs of lengths approximately equal to $40\mu\text{m}$. The very high density of SWCNTs affected the electron field emission current density because of the field screening effect. Raman spectra (not shown) indicated that the sample contained single-wall carbon nanotubes with diameters about 1.2nm based on the radial breathing mode signal at 190 cm^{-1} , the D-band at 1360 cm^{-1} , and the G-band at 1585 cm^{-1} . Figure 4.4 (b) is the top view of the SWCNTs sample that shows the high density of the CNTs covered the Si substrate with several SWCNTs bundles.

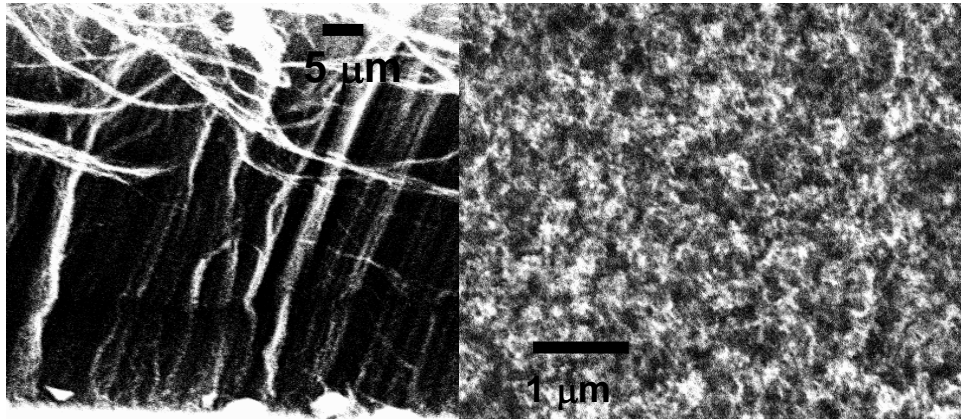


Figure 4.4: (a) Cross section SEM image of SWCNT bundles (b) Top view of SWCNT

Field emission measurement of single-walled carbon nanotubes was first performed at 2×10^{-6} Torr with the gap spacing of $60 \mu\text{m}$. Figure 4.5 shows the typical field emission of single-walled carbon nanotubes under high vacuum with the voltage scanned from 0 to 600V. The electron started to emit at the electric field lower than $1 \text{V}/\mu\text{m}$, and the turn-on of the SWCNT is approximately $1.5 \text{ V}/\mu\text{m}$, which indicates that single-walled carbon nanotubes are more denser and more easily to emit electron than multi-walled carbon nanotubes.

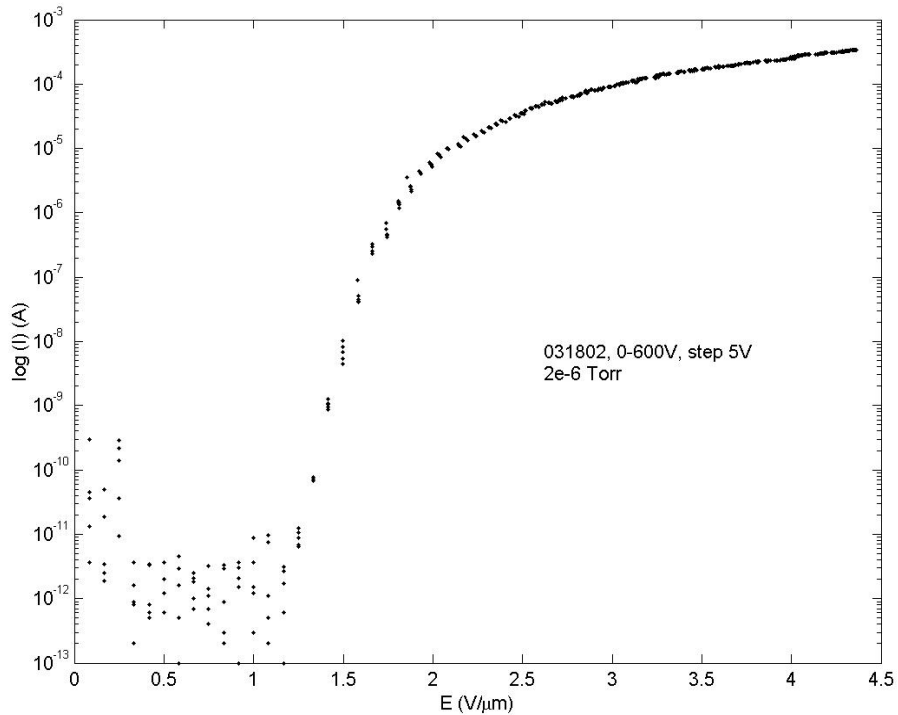


Figure 4.5: Field emission measurement of single-walled carbon nanotubes.

4.2 Growth of ZnO and its field emission

ZnO nanostructures growth is more complicate than CNTs growth and the growth mechanisms are not clear now. Several processing parameters need to concern such as growth temperature, substrate, lattice mismatch, catalyst, growth time, gas flow rate, kinetic energy, environment pressure and wafer (local) pressure. Figure 4.6 (a) and (b) show two SEM images of ZnO nanoneedles which were grown on Si (100) with Au liquid catalyst deposit on it. ZnO were grown at 550°C for 60 min with constant Ar flow rate. There does not have additional oxygen feed into the tube since the quartz tube is not perfectly leak tight, which provides enough oxygen for ZnO growth. As the SEM images show that ZnO nanoneedles spread out in a cactus-like morphology with many sharp tips (~100nm) at their ends, which are relatively easy to generate high local electric field between the emitters and the anode. Even though this kind of experiment setup can produce ZnO nanostructres but the reproducibility is poor and the structure size is larger than we expect, which indicates there are still many processing parameters need to be more precisely controlled.

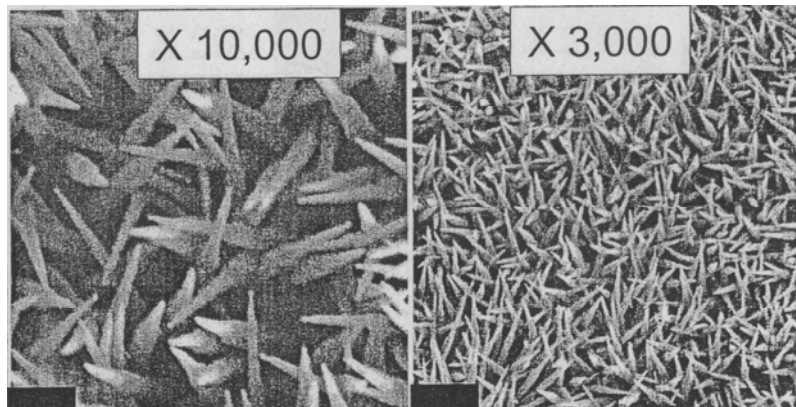


Figure 4.6: (a) higher resolution of SEM image for ZnO nanoneedles. Image size: 6×6 μm (b) lower resolution of SEM image for ZnO nanoneedles. Image size: 20×20 μm

In order to more precisely control the growth condition, the quartz tube was change to a both ends O-ring sealed leak tight quartz tube. The tube is first pumped down to 60 mTorr, which can guarantee how much reactive oxygen is fed in the tube during growth. Argon gas was fed as the furnace was turned on, but oxygen gas was only fed when the desire temperature was reached. If oxygen is fed at the same time as argon gas was fed, the Zn powder would be oxidized during elevating the quartz tube temperature instead of sublimating to vapor.

ZnO nanostructures dramatically change as we change the Si (100) wafer to Si (111). Si (111) does not need any catalyst solution deposit on it, which can greatly improve the catalyst contamination problem of Si (100). Figure 4.7 shows the SEM images of ZnO grow on Si (111) under 500 sccm of Ar and 15 sccm of O₂ at 650°C for 30 min. As the SEM images show, there have lots of ZnO nanoneedles (nanotips) spreading out form a small ZnO single crystal. The average size of the nanoneedles was smaller than 30nm, which is much smaller than the one show in Figure 4.6. Figure 4.7 (c) is the image taken at the corner of the sample which exhibits the corner also have the same structure as the center of the sample. Therefore, the ZnO was deposit very uniformly onto the Si wafer. Moreover, at figure (c) also shows some spring-like structure with lots of ZnO nanotips stand on top of it.

Figure 4.8 shows the ZnO grew on Si (100) with Au liquid solution coated on top it. Both samples that show in Figure 4.7 and 4.8 were grew on the same time and the growth conditions. As we can see that the structures of these two samples are dramatically different, the one synthesis on Si (100) shows lots of individual nanoneedles interacts with each other and the growth direction was much more regular than the one grew on Si

(111), but the size of the tip is approximately 2 times larger than the one grown on Si (111). However, the one grown on Si (111) shows smaller tip size and all the tips are grown on top of a small ZnO single crystal instead of growing individually. This indicates that even the same kind of material is used as the substrate, but different lattice conformations cause significant change of the ZnO nanostructures.

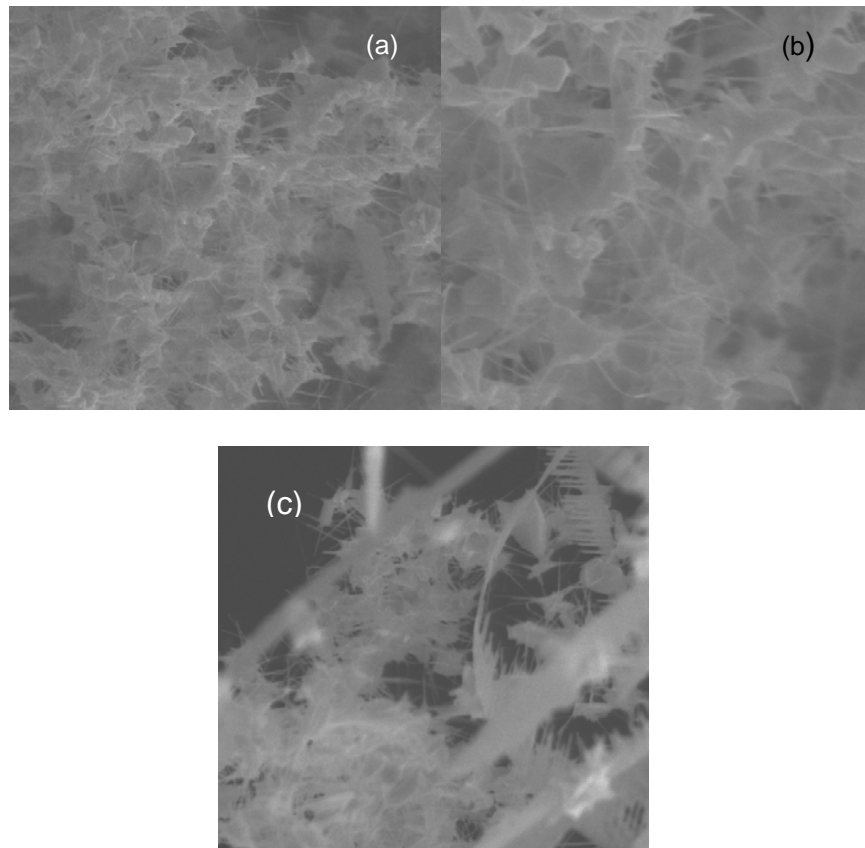


Figure 4.7 SEM images of ZnO nanostructure grown on Si (111) wafer, (a) is the magnification of 10K (image size $5 \times 5 \mu\text{m}$), (b) is the magnification of 20K (image size $2.5 \times 2.5 \mu\text{m}$) and (c) is the edge view of the sample with the magnification of 10K (image size $6 \times 6 \mu\text{m}$).

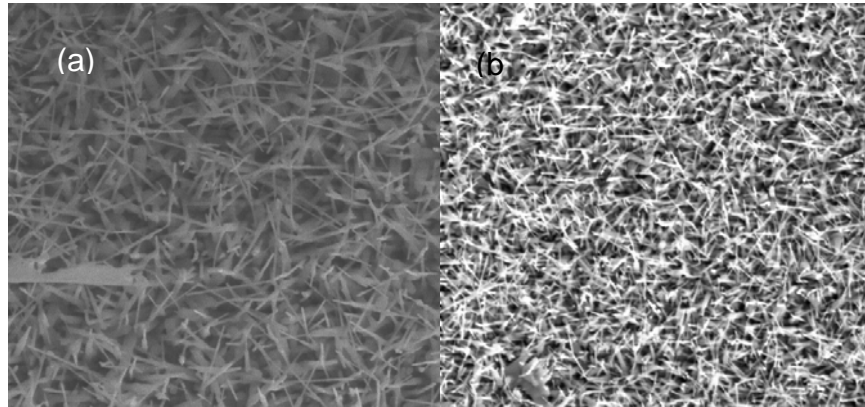


Figure 4.8 SEM images of ZnO nanostructure grow on Si (100) wafer, (a) is the magnification of 10K (image size $5\times 5\ \mu\text{m}$) and (b) is the magnification of 5K (image size $10\times 10\ \mu\text{m}$)

As mentioned in chapter 2 that ZnO has a strong UV peak at 380nm and a broad green band emission around 510nm, Figure 4.9 shows the photoluminescence (PL) spectra for both Si (100) (Figure 4.8) and Si (111) (Figure 4.7) samples. PL spectra of the as-grown samples were measured at room temperature. As shown in Figure 4.9, both samples show a strong and sharp UV emission at 380 nm (3.26eV), which is attributed to the near band edge emission of the wide band gap ZnO. The difference is that Si (111) sample shows no green emission at 510nm (2.34 eV) while Si (100) sample shows a relatively strong green emission at 510nm. The reason for the vanished green emission of Si (111) is still unknown, but it is a great improvement that the non-green emission ZnO with relatively small structure can be synthesized in a certain given growth condition.

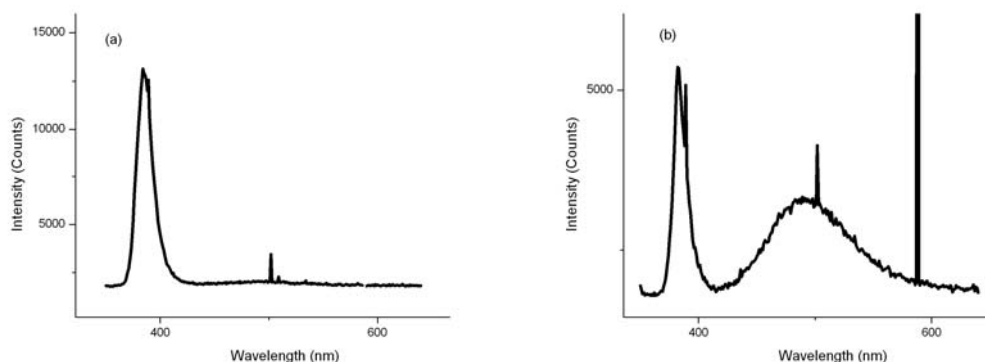


Figure 4.9 PL spectrum measured at room temperature, (a) is the PL spectrum of Si (111) sample, which shows no green emission and (b) is the PL spectrum of Si (100) sample, which shows strong green emission at 510nm.

Field emission measurement of ZnO nanoneedles (sample of Figure 4.6) was first performed at 2×10^{-6} Torr with the gap spacing of $120 \mu\text{m}$. Figure 4.10 shows the typical field emission of ZnO nanoneedles with the voltage scanned from 0 to 600V. The voltage step is 5V for this scan. Figure 4.10 shows that the electron started to emit at the electric field much lower than $1 \text{V}/\mu\text{m}$, and the turn-on of the ZnO nanoneedles is approximately $2.5 \text{ V}/\mu\text{m}$, which indicates that ZnO also possesses good electron emitter properties that can comparable of carbon nanotubes. The current density for this ZnO sample is lower than that of SWCNTs and MWCNTs, which can be explained by the field emission sites of the ZnO. As the SEM images shows above that there are less ZnO nanoneedles at a certain area compare to the highly dense carbon nanotubes samples, which results in a smaller current density. Figure 4.11 is the Fowler-Nordheim plot of figure 4.10, the work function for ZnO is 5.3 eV; therefore, the field enhancement factor β can be calculated out as 1050.

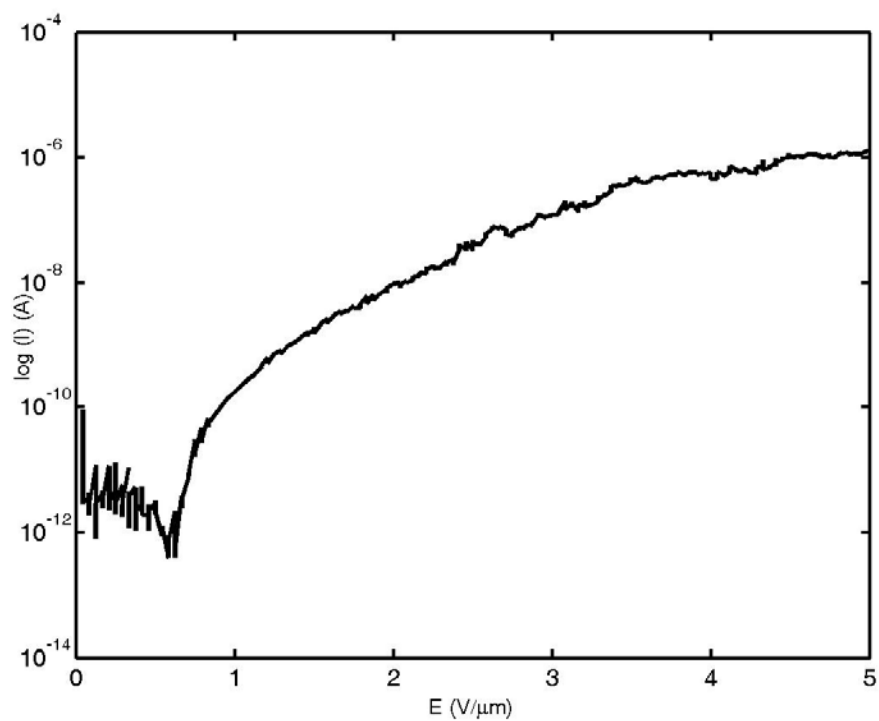


Figure 4.10: Field emission measurement of ZnO nanoneedles.

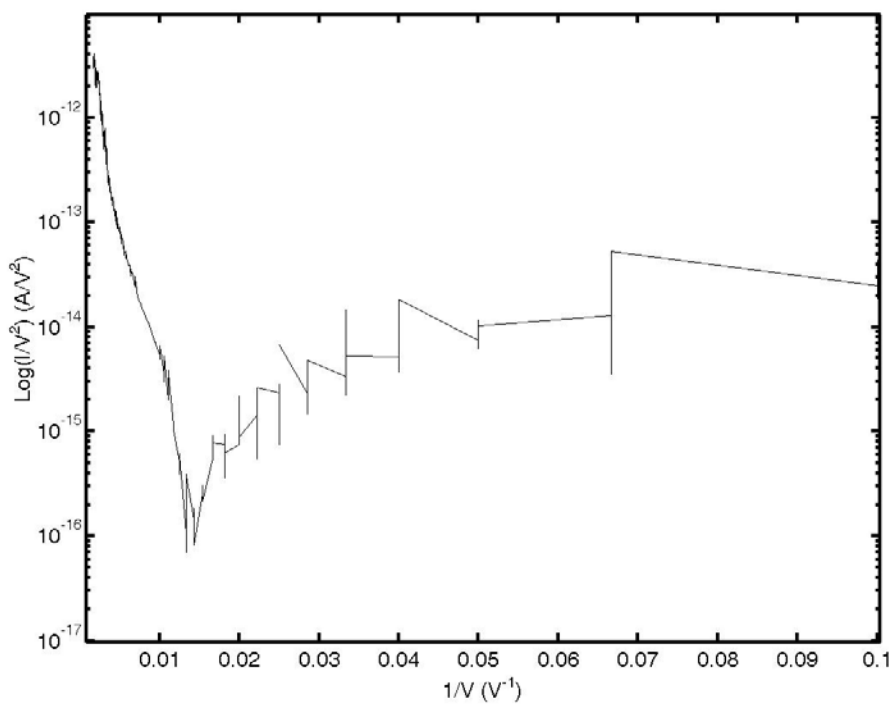


Figure 4.11: Fowler-Nordheim plot of ZnO.

4.3 Field emission measurements under diverse pressures

A variety of nanostructured materials have been considered for use as an efficient field emitter for field emission displays (FEDs) and related vacuum microelectronics applications. Carbon nanotubes are considered to be the most promising candidate for field emission display (FED) applications because they are small in diameters and large in length leading to a very large field enhancement at the tips of the nanotubes. The field enhancement allows high electron field emission current density at low electrical fields. A relatively simple fabrication process using screen printing of CNTs paste or chemical vapor deposition of CNTs on glass substrates have been reported to have superior properties as compared to molybdenum (Mo) micro-tip arrays [145,146]. However, field emission for single-wall carbon nanotubes (SWCNTs) and multi-wall carbon nanotubes exhibit a permanent decrease in FE current density and an increase in the turn-on electrical field in oxygen environments [147]. This degradation phenomenon greatly impacts CNTs application in FED under poor vacuum or low-pressure gas filled environments. Besides the geometric factor (aspect ratio), thermal stability, and ambient insensitivity are also important factors for choosing a material for applications as cold cathode electron field emitters

An FED is assembled using hundreds of micrometre spacers as supports between the anode and cathode plate and must be sealed using fritted glass under vacuum. The vacuum level normally deteriorates from an initial evacuated pressure of $\sim 10^{-7}$ Torr to 10^{-6} – 10^{-5} Torr due to outgassing from device components and the phosphor during the vacuum-sealing process. The residual gas or gas liberated by electron bombardment of

FED components interacts with field emitters and has a negative effect on device properties during display operation, showing a decrease in emission current and an increase in turn-on field, resulting in a decay of luminance of the FED. Environmental stability is one of the main requirements for field emitters in FED applications.

Field emission measurements of ZnO nanoneedles have already been reported to be a valuable candidate for field emission application in high vacuum [148]. Therefore, ZnO were executed in this research due to the degradation phenomenon of CNTs under poor vacuum. Moreover, ZnO has a relatively high melting point (1975°C) and is believed to have a more stable phase under oxygen ambient as compared to carbon nanotubes. The electron field emission current density depends on the nanostructures of ZnO. The shapes especially affect the aspect ratios and in turn the field enhancement at the electron emission sites. ZnO electron field emission properties have been measured in a fairly large gas pressures range and its electron field emission properties are characterized and compared with both MWCNTs and SWCNTs in the same experimental conditions.

4.3.1 ZnO nanoneedles field emission measurement under diverse pressures

FE measurement of ZnO nanoneedles was initially performed at 1×10^{-6} Torr with applied voltage being scanned from 0 to 800V. The gap spacing between the anode and the cathode was 120 μ m. The electron field emission current shown in Figure 4.8 curve (a) was 5.8×10^{-7} A that is much smaller than that for both MWCNTs and SWCNTs at the same applied electric field of 4V/ μ m as shown in Figure 4.9 and 4.10. ZnO nanoneedles and MWCNTs have approximately the same turn on voltage but the current was higher

for MWCNTs since MWCNTs has the higher aspect ratio and much more electron field emission sites than the ZnO sample as shown in the SEM figures given above. Shown in Figure 4.12 were data taken when the chamber pressure was adjusted from 1×10^{-6} Torr (curve (a)) to 0.5mTorr (curve (b)), 3.5mTorr (curve (c)), 30mTorr (curve (d)), and then 60 mTorr sequentially. After measuring the FE with intentional air leaks, the chamber was pumped to 1×10^{-6} Torr again to study the pressure effects on the recovery of the FE properties.

The FE test results shown in Figure 4.8 for ZnO nanoneedles under different gas pressures, show that the electron emission currents decreased with the increasing turn-on voltage when the air leak increased. At a fixed applied electric field of $4 \text{V}/\mu\text{m}$ (see Figure 4.12) the emission current for curve (b) (0.5mTorr) is smaller than curve (a) by more than 60% and that the emission current shown by curve (d) (30mTorr) is about 10 times smaller than that shown by curve (a). This indicates that the electron field emission current was approximately 10 times smaller for the air pressure of 30mTorr compared to that measured at a low pressure of 1×10^{-6} Torr. The curve (e) shown in Figure 4.12 represent data measured at 60mTorr with applied voltage being scanned from 0V to 380V. Gas breakdown of the gas occurred when the applied voltage was greater than 400V. The larger gap spacing used for ZnO due to its long needles and surface morphology also contributed to the premature breakdown at a lower voltage, too, because the probability for emitted electrons to cause impact ionization of air molecules was higher with a larger gap spacing.

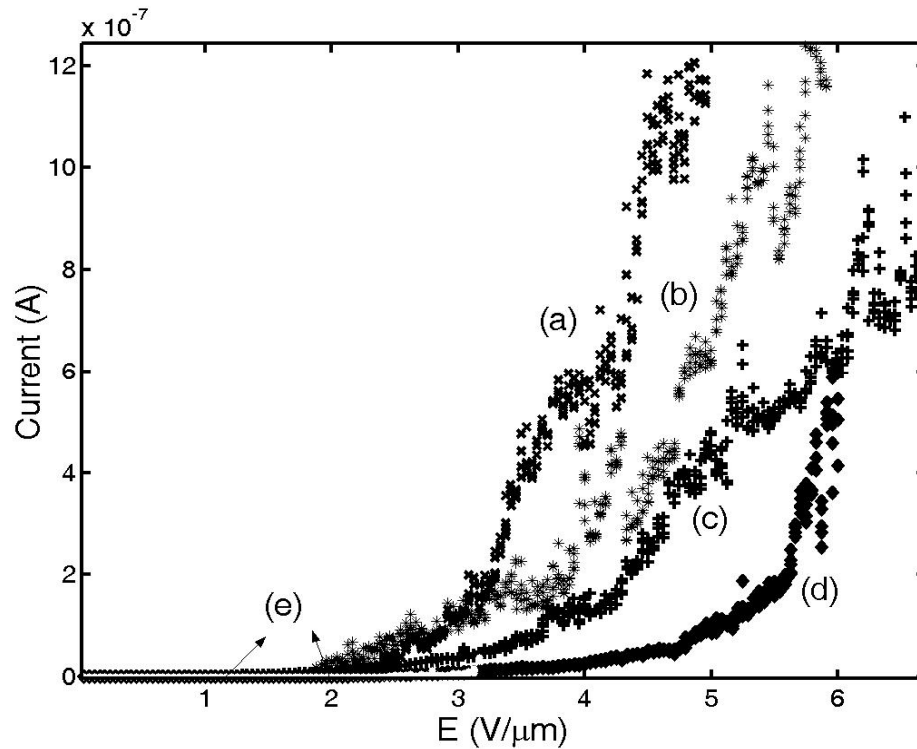


Figure 4.12 I-E curves of field emission of ZnO nanoneedles measurement at varied air pressures: (a) 1×10^{-6} Torr, with the cross marks (b) 0.5mTorr, with the asterisk marks (c) 3.5 mtorr, with the plus marks, (d) 30mTorr, with the diamond marks (e) 60mTorr, which is the curve that overlapped with curve (d) up to $3 \text{ V}/\mu\text{m}$

4.3.2 SWCNT & MWCNTs field emission measurement under diverse pressures

Figure 4.13 and 4.14 are the FE measurements at different gas pressures for MWCNTs and SWCNTs. The experimental procedure followed that used for ZnO nanoneedles. Figure 4.13 shows that when gas pressure increased from 1×10^{-6} Torr to 60mTorr, the turn-on voltage of MWCNTs increased from $2 \text{ V}/\mu\text{m}$ to $5 \text{ V}/\mu\text{m}$ with greatly decreased electron field emission current. Electron field emission current measured in vacuum at 1×10^{-6} Torr was 3 orders of magnitude higher than that measured at 60mTorr under the

same applied electric field of $3\text{V}/\mu\text{m}$, which indicated that MWCNTs were damaged during measuring under air leakage. Figure 4.14 shows a more apparent result of the SWCNTs emission current that decreased as the gas pressure increased while the turn-on voltage increased greatly due to the increasing of air leakage. For example, as shown in Figure 4.14, the turn-on voltage was 0.8V and emission current was $1 \times 10^{-5}\text{A}$ (at $E=3\text{V}/\mu\text{m}$) when measurement was done in vacuum at $1 \times 10^{-6}\text{Torr}$. The turn-on voltage increased to greater than $6\text{V}/\mu\text{m}$ for measurements done at 60mTorr . It also indicates that there was practically no emission current ($<1 \times 10^{-12}\text{A}$) at the applied electric field of $3\text{V}/\mu\text{m}$. The faster increase in the turn-on voltage for SWCNTs than MWCNTs when the measurements were done under increasing air leakage and therefore increasing air pressure suggested that FE measurements at high pressures caused the ionized gas molecules to accelerate and collide more frequently with carbon nanotubes resulting to more damages to the tips of carbon nanotubes.

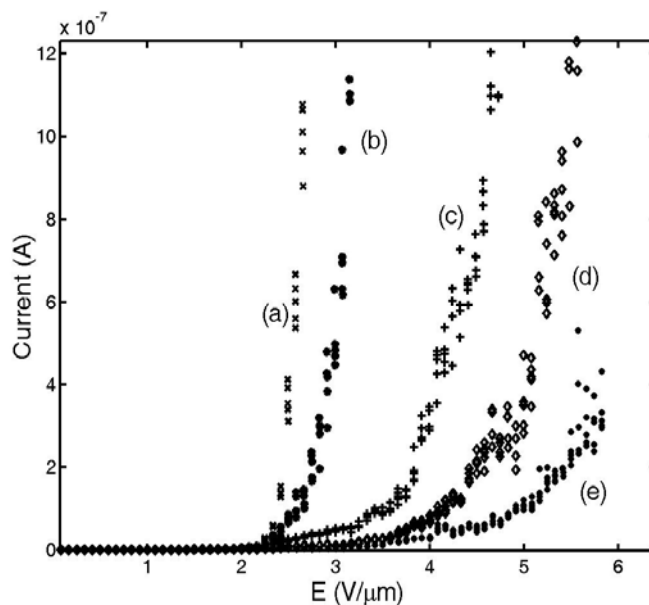


Figure 4.13 I-E curves of field emission of MWCNTs measurements at varied pressures (a) 1×10^{-6} Torr, with the cross marks (b) 0.5mTorr, with the asterisk marks (c) 3.5 mtorr, with the plus marks, (d) 30mTorr, with the diamond marks (e) 60mTorr, with the dark circles.

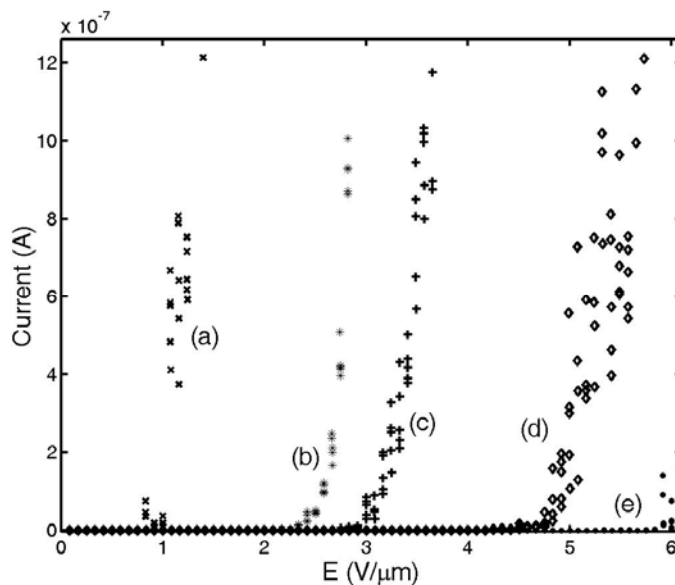


Figure 4.14 I-E curves of electron field emission of SWCNTs measured at varied pressures (a) 1×10^{-6} Torr, with the cross marks (b) 0.5mTorr, with the asterisk marks (c) 3.5 mtorr, with the plus marks, (d) 30mTorr, with the diamond marks (e) 60mTorr, with the dark circles.

4.3.3 Field emission pressure effect of ZnO nanoneedles and CNTs

In order to prove this assumption that CNTs were damaged at high pressure, the chamber was evacuated down to 1×10^{-6} Torr again for testing the FE after the FE measurements were performed at high pressures. Figure 4.15 shows the low pressure FE measurement for ZnO nanoneedles before and after testing at high pressures, showing that the FE of ZnO nanoneedles was nearly the same even after the FE tests were performed at high pressure. This demonstrates that ZnO nanoneedles were not as easy to be damaged as carbon nanotubes by subjecting to FE measurements with air leakage. Considering that the series of measurements done for varied gas pressures as shown in Figures 4.12 and 4.15 were carried out for the same sample, the ZnO nanoneedles proved to be a more robust and inert electron field emitter than carbon nanotubes under poor vacuum environments.

Shown in Figure 4.16 and 4.17 are data obtained from FE measurement carried out in vacuum without air leakage for MWCNTs and SWCNTs. It shows that after being subjected to high pressure measurement, the electron field emission current decreased with increasing turn-on voltage even after the chamber was pumped down to high vacuum. As shown in Figure 4.17, the FE measurements for SWCNTs manifested that SWCNTs suffered severe structural damages during FE measurements at high pressures. The undesirable effect of absorbed O_2 on the tips of CNTs was believed to also result in reactive etching/oxidation of CNTs [42, 43].

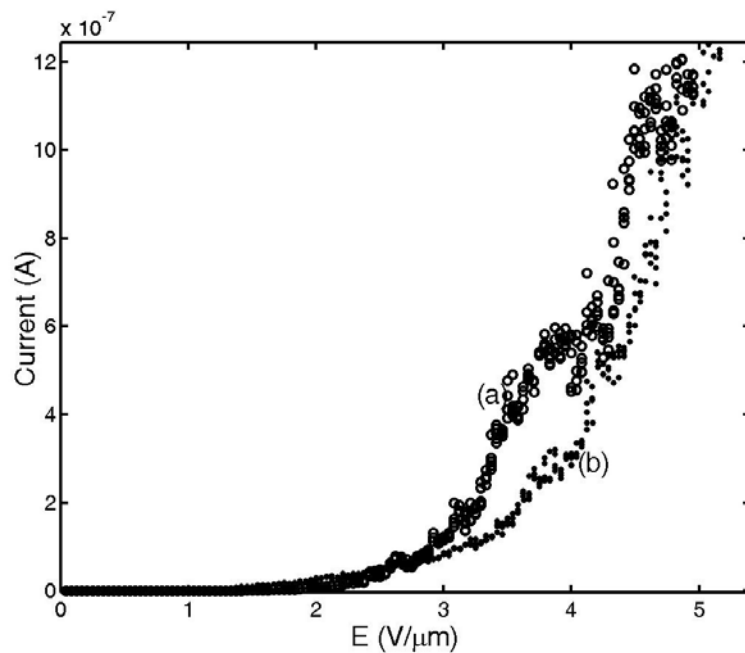


Figure 4.15: I-E curves of field emission measurements for ZnO nanoneedles at low pressure before (a) and after (b) measurements carried out at higher pressures.

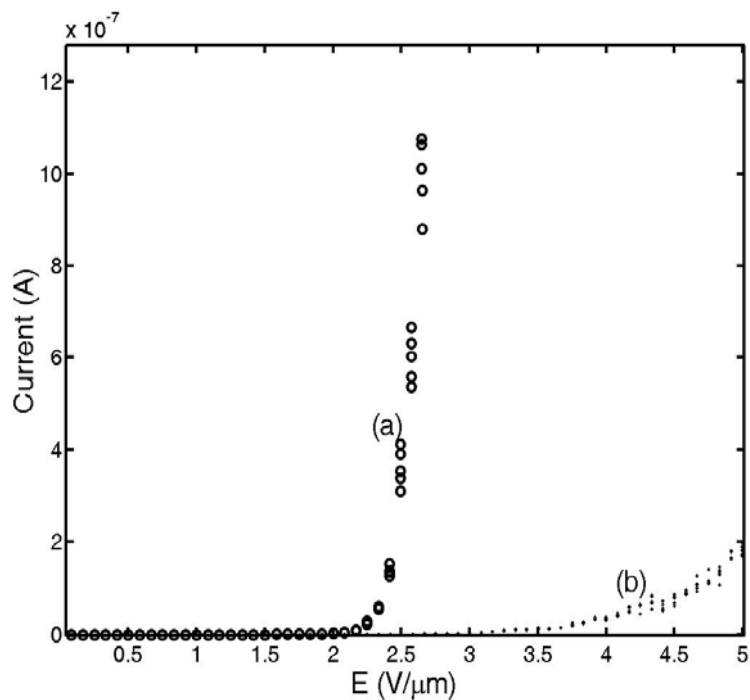


Figure 4.16: I-E curves of field emission measurements for MWCNTs at low pressure before (a) and after (b) measurements carried out at higher pressures.

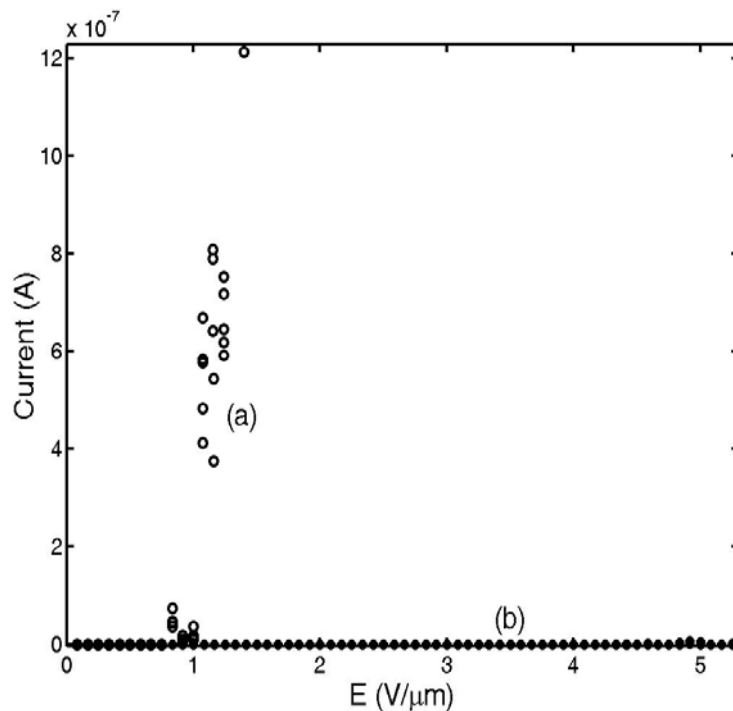


Figure 4.17: I-E curves for Field emission measurements for SWCNTs at low pressure before (a) and after (b) measurements carried out at high pressures.

4.4.4 Low and high pressure current stability of ZnO and CNTs

Shown in Figure 4.18 are data obtained from FE stability tests for both ZnO and MWCNTs in vacuum at 1×10^{-6} Torr and at 0.5 mTorr with a constant applied electric field of $4 \text{ V}/\mu\text{m}$. Curve (a) and (b) in Figure 4.18 are for MWCNTs FE stability tests at low pressure and high pressure, respectively. Curve (a) shows that the emission current for MWCNTs at low pressure was still high even the emission current became about 1/3 smaller than the initial emission current after a 5 hours stability measurement. On the other hand, the FE stability tests for MWCNTs at high pressures showed rapidly decreasing electron emission current from the initial emission current of $\sim 1 \times 10^{-5} \text{ A}$ to less than $1 \times 10^{-9} \text{ A}$ after a 5 hours testing. Comparing to curve (d) for ZnO nanoneedles, the

FE stability test shows that even at the high end of the pressure range being examined, the electron emission current decreased only by half from the initial electron field emission current. This indicates that the ZnO nanoneedles emitters are still stable even after being subjected to FE measurements at high pressure for a long period of time. Curve (c) in Figure 4.18 shows the FE stability test of ZnO nanoneedles in vacuum. A much more stable electron field emission current was recorded.

The more stable electric field emission current in high pressure was suspected that in high pressure there are more ionized gas molecules, which bombard the ZnO nanoneedles surface, cause the spiking tips to be damage. Therefore, it would generate more uniform local electric field between the ZnO nanoneedles and the anode. The one directly measured in low pressure have more spiking tips that cause a gradient of local electric field, and result in a more fluctuated emission current. This phenomenon can also be found in figure 4.15 that curve (a) is more unstable than curve (b) that underwent a high pressure field emission measured process.

FE tests for ZnO nanoneedles under air leakage and FE stability measurements demonstrated that ZnO is a better electron field emitter material than carbon nanotubes for electron field emission operation in poor vacuum or with air leakage. It also demonstrated good long-term stability even when the air pressure was at 0.5mTorr. ZnO can be a very useful cold cathode material for vacuum microelectronics and field emission displays.

In summary, both CNTs and ZnO nanoneedles serve as excellent electron field emission cold cathode with low turn-on electric fields in high vacuum. However, ZnO nanoneedles can recover their FE properties even after being subjected to FE

measurements at high pressures up to 60mTorr by introducing air into the test chamber. ZnO nanoneedles is more favorable than CNTs as cold cathode for applications in poor vacuum and in low pressure environments filled with oxidizing gases.

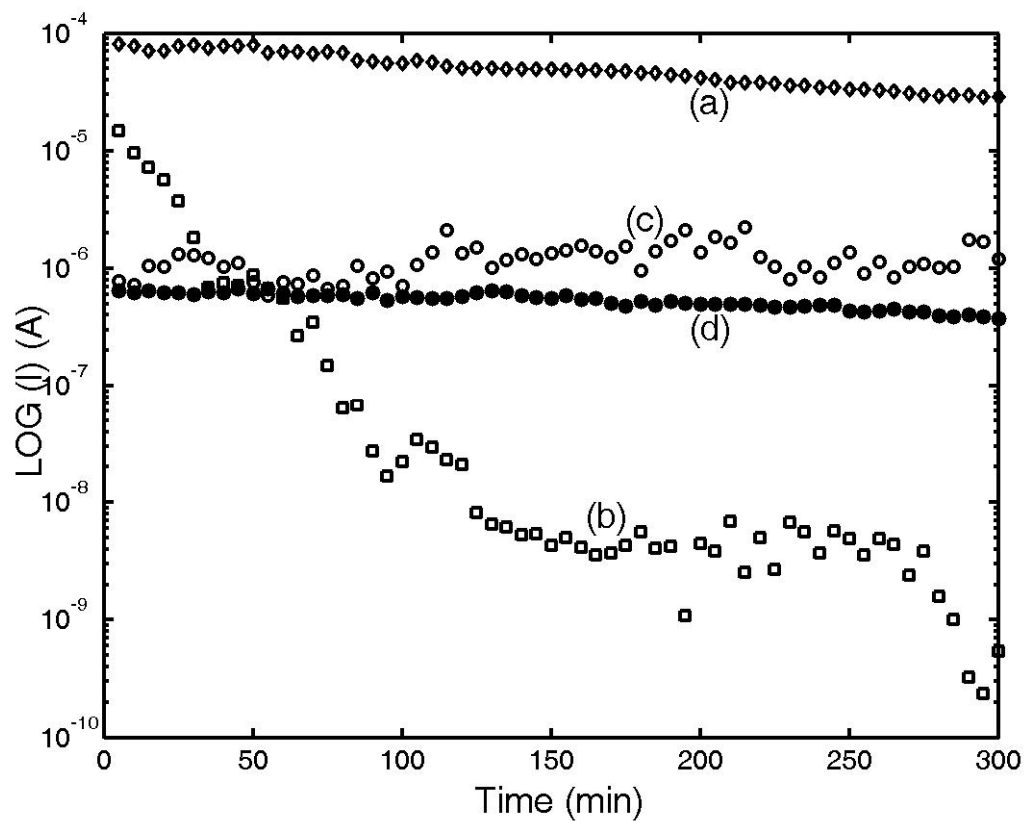


Figure 4.18 Stability measurements for both MWCNTs and ZnO nanoneedles in vacuum at 1×10^{-6} Torr and a higher pressure at 0.5 mTorr at a constant applied electric field of $4 \text{ V}/\mu\text{m}$:
 (a) MWCNTs stability test in vacuum (b) MWCNTs stability test at 0.5 mTorr (c) ZnO nanoneedles stability test in vacuum (d) ZnO nanoneedles stability test at 0.5 mTorr.

CHAPTER 5

SUMMARY AND FUTURE DIRECTIONS

Phenomenal progress has been made in the science of carbon nanotubes since the publication of Iijima's paper in 1991. Synthesis of vertically well-aligned MWCNTs and SWCNTs is under a mature stage which can be manufactured in small quantity and be purified. However, how to synthesis carbon nanotubes at desired direction, which means how to control its chirality is still blurry, and need to have future investigations. Theoreticians have predicted predominant electronic and mechanical properties, and many of these predictions have been confirmed experimentally. Carbon nanotubes is a extraordinary material for nanoelectronics application such as: nano-sized tweezer, interconnection for VLSI, single electron devices, sensor, field emission display, hydrogen storage, etc. However, how to integrate nanotubes into efficient device is still a challenge in fabrication and large scale production.

Even though ZnO thin film has been investigated in 1960 and related devices have been mass produced, ZnO nanostructured materials are only under incubating stage since the passed twenty first century. Due to the small in size ZnO nanostructured materials show greatly different in electrical, optical, and chemical behaviors. The growth mechanisms of ZnO nanostructured material are still under study. How to synthesis

vertical array ZnO nanowires is the further step for utilizing ZnO nanowires for electrical and optical applications. P-type doped ZnO is an important stage for diode applications.

Field emission electron source is one of the most advanced and broadly studied applications of CNTs and ZnO. In spite of the high work function ($\sim 5\text{eV}$), CNTs emit electron very easily, compared to other carbon based materials. This is due to their 1D structure with a high aspect ratio, and high electrical conductivity. However, the field emission degradation behavior under high pressure is an important concern of carbon nanotubes for FED applications, and needs future improvement. The establishments of inexpensive synthetic routes and preparation methods of aligned CNT films, as well as a clarification of the mechanism are strongly desired for future development.

ZnO nanoneedles is a powerful material for low and high pressure field emitters due to its inert field emission behavior under diverse pressure effects. However, synthesis high density ZnO nanoneedles array is a challenge for improving its field emission current density. ZnO can be a very potential material if we can overcome the problems such as: (1) controllable structural growth (2) large scale production (3) growth mechanism (4) p-type doping, etc. Since ZnO nanostructure surface is very sensitive, and changes with different environment; therefore, how to find a method to efficiently control its surface properties, such as surface resistance, chemical reactions, optical properties, will greatly improve its versatile applications.

In these work, MWCNTs and SWCNTs have been successfully deposited on different kinds of catalyst layers by using thermal CVD. The catalyst size and nucleation site are the critical parameters for synthesis SWCNTs, since the size of the catalyst is the base for nanotubes growth, which directly affects the circumference of the nanotubes. Another

important role is played by the growth time. Field emission results from coated carbon nanotube show clearly Fowler-Nordheim behavior. Carbon nanotube films with turn-on electric fields as low as 1.5 volt per micrometer and field enhancement factor as high as 2000 have been achieved.

Several ZnO nanostructures have been fabricated by tuning the processing parameter such as, gas flow rate, growth temperature, local (wafer) pressure, environment pressure, etc. ZnO nanoneedles have been synthesized by thermal evaporation with a certain kind of growth parameters. Field emission from coated ZnO nanoneedles showed turn-on voltage as low as 1 volt per micrometer, but with lower current density, which may be result from sparse ZnO nanoneedle sites.

Many obstacles still remain. From field electron emission application's point of view, several problems should be solved in order to obtain a better field emission performance. The alignment, length, growth direction uniformity of carbon nanotubes and ZnO need to be well controlled. The density of carbon nanotubes and ZnO should be optimized to eliminate the field screening effect. The growth and field emission mechanisms with pressure effect for carbon nanotubes and ZnO need to be deeply investigated.

BIBLIOGRAPHY

- [1] H. W. Kroto, J. R. Heath, S.C. O'Brien, R.F. Curl, and R.E. Smalley, *Nature*, 318, 162 (1985)
- [2] S. Iijima, *Nature*, 354, 56 (1991)
- [3] Thomas W. Ebbesen, editor, "Carbon nanotubes: preparation and properties", CRC Press, 1997
- [4] T.W. Ebbesen, H. Hiura, J. Fujita, Y. Ochiai, S. Matsui, and K. Tanigaki, *Chem. Phys. Lett.*, 209, 83(1993)
- [5] A. Thess, R. Lee, P. Nikolaev, H. Dai, P. Petit, J. Robert, C. Xu, Y.H. Lee, S.G. Kim, A.G. Rinzler, D.T. Colbert, G.E. Scuseria, D. Tomanek, J.E. Fischer, and R.E. Smalley, *Science*, 273, 483 (1996)
- [6] N. Hatta, and K. Murata, *Chem. Phys. Lett.*, 217, 398 (1994)
- [7] C. J. Lee and J. Park, *Appl. Phys. Lett.*, 77, 3397 (2000)
- [8] M. Meyyappan, editor, "Carbon nanotubes science and applications", CRC Press (2004)
- [9] C.M. Lieber, *Solid State Commun.* 107, 607 (1998)
- [10] H. Gleiter, *Acta Mater.*, 48, 1, (2000)
- [11] Z. L. Wang and Z. C. Kang, editors, "Functional and Smart Materials", Plenum, New York (1998)
- [12] Z.L. Wang, *J. Phys. Condensed Matter*, 16, R829, (2004)
- [13] J. Nishii, F.M. Hossain, S. Takagi, T. Aita, K. Saikusa, Y. Ohmaki, I. Ohkubo, S. Kishimoto, A. Ohtomo, T. Fukumura, F. Matsukura, Y. Ohno, H. Koinuma, H. Ohno, and M. Kawasaki, *Jpn. J. Appl. Phys.* 42, L347 (2003).
- [14] F. M. Hossain, J. Nishii, S. Takagi, T. Sugihara, A. Ohtomo, T. Fukumura, H. Koinuma, H. Ohno, M. Kawasaki, *Physica E* 21, 911 (2004)
- [15] B.J. Norris, J. Anderson, J.F. Wager, D.A. Kszler, *J. Phys. D: Appl. Phys.* 36, L105 (2003).
- [16] P. Yang, H. Yan, S. Mao, R. Russo, J. Johnson, R. Saykally, N. Morris, J. Pham, R. He, H.-J. Choi, *Adv. Mater.*, 12, 323 (2002).
- [17] N.G. Chopra, R.J. Luyken, K. Cherrey, V.H. Crespi, M.L. Cohen, S.G. Louie, A. Zettl, *Science*, 269, 966 (1995)
- [18] E. Bengu, L.D. Marks, *Phys. Rev. Lett.* 86, 2385 (2001)
- [19] A. Rothschild, J. Sloan, R. Tenne, *J. Am. Chem. Soc.*, 122, 5169 (2000)
- [20] F. Krumeich, H.J. Muhr, M. Niederberger, F. Bieri, B. Schnyder, R. Nesper, *J. Am. Chem. Soc.*, 121, 8324 (1999)
- [21] M. Remskar, A. Mrzel, Z. Skraba, A. Jesih, A. Ceh, J. Demsar, P. Stadelmann, F. Levy, D. Mihailovic, *Science*, 292, 479 (2001)
- [22] B.C. Satishkumar, A. Govindaraj, E.M. Vogl, L. Basumallick, C. N. R. Rao, *J. Mater. Res.*, 12, 604 (1997)
- [23] M. Adachi, T. Harada, M. Harada, *Langmuir*, 15, 7097 (1999)

- [24] R. Tenne, M. Homyonfer, Y. Feldman, *Chem. Mater.*, 10, 3225 (1998)
- [25] Y. Saito, T. Matsumoto, *Nature*, 392, 237 (1998)
- [26] T.J. Trentler, K.M. Hickman, S.C. Goel, A.M. Viano, P.C. Gibbons, W.E. Buhro, *Science*, 270, 1791 (1995)
- [27] A.M. Morales, C.M. Lieber, *Science*, 279, 208 (1998)
- [28] S.T. Lee, N. Wang, Y.F. Zhang, Y.H. Tang, *MRS Bull.*, 24, 36 (1999)
- [29] X.F. Duan, C.M. Lieber, *Adv. Mater.*, 12, 298 (2000)
- [30] C.C. Chen, C.C. Yeh, C.H. Chen, M.Y. Yu, H.L. Liu, J.J. Wu, K.H. Chen, L.C. Chen, J.Y. Peng, Y.F. Chen, *J. Am. Chem. Soc.*, 123, 2791 (2001)
- [31] M.H. Huang, Y.Y. Wu, H. Feick, N. Tran, E. Weber, P.D. Yang, *Adv. Mater.*, 13, 113 (2001)
- [32] M.J. Zheng, L.D. Zhang, X.Y. Zhang, J. Zhang, G.H. Li, *Chem. Phys. Lett.*, 334, 298 (2001)
- [33] Z.W. Pan, Z.R. Dai, C. Ma, Z.L. Wang, *J. Am. Chem. Soc.*, 124, 1817 (2002)
- [34] H.J. Dai, E.W. Wong, Y.Z. Lu, S.S. Fan, C.M. Lieber, *Nature*, 375, 769 (1995)
- [35] P.D. Yang, C.M. Lieber, *J. Mater. Res.*, 12, 2981 (1997)
- [36] L. Manna, E.C. Scher, A.P. Alivisatos, *J. Am. Chem. Soc.*, 122, 12 700 (2000)
- [37] Z.W. Pan, Z.R. Dai, Z.L. Wang, *Science*, 291, 1947 (2001)
- [38] W. Shi, H. Peng, N. Wang, C.P. Li, L. Xu, C.S. Lee, R. Kalish, S.T. Lee, *J. Am. Chem. Soc.*, 123, 11 095 (2001)
- [40] De Heer W A, Châtelain A, Ugarte D, *Science*, 270, 1179 (1995)
- [41] Rinzler A G, Hafner J H, Nikolaev P, Lou L, Kim S G, Tomanek D, Nordlander p, Colbert D T and Smally RE, *Science*, 269, 1550 (1995)
- [42] A. Wadhawan, R.E. Stallcup II, K. F. Stephen II, J. Perez, I. A. Akwani, *Appl. Phys. Lett.* 79, 1867, (2001)
- [43] Dean K.A., Chalamala B.R., *Appl. Phys. Lett.*, 8, 3017 (1999)
- [44] Reuss R.H., Chalamala B.R., *Inf. Disp.*, 17, 28 (2001)
- [45] R. Saito, G. Dresselhaus, and M. S. Dresselhaus, editors, "Physical Properties of Carbon Nanotubes", Imperial College Press, 1998
- [46] M.S. Dresselhaus, G. Dresselhaus, and R. Saito, *Carbon*, 33, 883 (1995)
- [47] de Wit, R., *J. Appl. Phys.*, 42, 3304, (1971)
- [48] Harris, W. F. and Scriven, L. E., *J. Appl. Phys.*, 42, 3309, (1971)
- [49] Iijima, S. Ichihashi, T., and Ando, Y., *Nature*, 356, 776, (1992)
- [50] S. Reich and C. Thomsen, *Phys. Rev. B*, v65, 155411
- [51] M. Bockrath et al. *Science*, 275, 1922 (1997)
- [52] S. J. Tans et al. *Nature*, 391, 59 (1997)
- [53] S. Flank et al. *Science*, 280, 1744 (1998)
- [54] H. T. Soh et al., *Appl. Phys. Lett.*, 75, 627 (1999)
- [55] J. F. Despres, E. Daguerre, and K. Lafdi, *Carbon*, 33, 87 (1995)
- [56] J. Lu, and J. Han, *Int. J. High Speed Elec. Sys.*, 9, 101, (1998)
- [57] J. Cao, Q. Wang, and H. Dai, *Phys. Rev. Lett.*, 90, 157601 (2003)
- [58] S. Paulson et al. *Appl. Phys. Lett.*, 75, 2936 (1999)
- [59] P. S. Davids, L. Wang, A. Saxena, A. R. Bishop, *Phys. Rev. B* 48, 17545, (1993)
- [60] G. Baumgartner et al., *Phys. Rev. B* 55, 6704 (1997)
- [61] H. Ajiki and T. Ando, *J. Phys. Soc. Jpn.*, 62, 1255, (1993)
- [62] H. Ajiki and T. Ando, *J. Phys. Soc. Jpn.*, 62, 2479, (1993)

- [63] J. P. Lu, *Phys. Rev. Lett.*, 74, 1123 (1995)
- [64] C. Schonberger et al. *Appl. Phys. A.*, 69, 283, (1999)
- [65] P. M Ajayan, T. W. Ebbesen, T. Ichihashi, , S. Iijima., K. Tanigaki, and H. Hiura, *Nature*, 362, 522, (1993)
- [66] H. Hiura, T. W. Ebbesen, K. Tanigaki, *Adv. Mater.* 7, 275 (1995)
- [67] O. Zhou, R. M. Murphy, D. W. Chen, C. H. R. C. Haddon, A. P. Ramirez, S. H. Glarum, *Science*, 263, 1744 (1994)
- [68] J. Zhao, A. Buldum, J. Han, and J. P Lu *Nanotechnology*, v 13, n 2, p 195-200 (2002)
- [69] M. Kruger et al. *N. J. of Phys.*, 5, 138 (2003)
- [70] T. W. Ebbesen, Hiura H. J. Fujita, Y. Ochiai, S. Matsui, K. Tanigaki, *Chem. Phys. Lett.*, 209, 83 (1993)
- [71] R. Bacon, *J. Appl. Phys.* 31, 283 (1960)
- [72] W. Kratschmer, L. D. Lamb, K. Fostiropoulos, D. R. Huffman, *Nature*, 37, 354 (1990)
- [73] T. W. Ebbesen, and P. M. Ajayan, *Nature*, 358, 220 (1992)
- [74] S. Seraphin, D. Zhou, J. Jiao, J. C. Withers, R. Loufty, *Carbon*, 31, 685 (1993)
- [75] S. Iijima and T. Ichihashi, *Nature*, 363, 603 (1993)
- [76] D. S. Bethune et al., *Nature*, 363, 605 (1993)
- [77] P.M. Ajayan et al., *Chem Phys. Lett.*, 215, 509 (1993)
- [78] S. Serapin et al. *Chem. Phys. Lett.*, 217, 191 (1994)
- [79] C. H. Kiang et al. *Carbon* 33, 903 (1995)
- [80] Y. Saito, K. Kawabata, and M. Okuda, *J. Phys. Chem.*, 99, 16076 (1995)
- [81] D. S. Bethune, C. H. Kiang, M. S. de Vires, G. Gorman, R. Savoy, J. Vazquez, R. Beyers, *Nature*, 363, 605 (1993)
- [82] K. Tanaka, T. Yamabe, and K. Fukui, "The Science and Technology of Carbon Nanotubes", Elsevier, 1999
- [83] M. Takizawa, et al. *Chem. Phys. Lett.*, 302, 146 (1999)
- [84] S. Bandow et al., *Phys. Rev. Lett.*, 80 3779 (1998)
- [85] T. Guo et al. *J. Phys. Chem.* 99, 10694 (1995)
- [86] Bhushan editor, "Handbook of Nanotechnology", Springer
- [87] A. Thess, R. Lee, P. Nikolaev, H. Dai, P. Petit, J. Robert, C. Xu, Y. H. Lee, S. G. Kim, A. G. Rinzler, D. T. Collert, G. E. Scuseria, D. Tomanek, J. E. Fischer, and R. E. Smalley, *Science*, 273, 483 (1996)
- [88] R.E. Smalley, *Acc. Chem. Research*, 25, 98 (1992)
- [89] O. A. Louchev, *Phys. Stat. Sol*, 193, 585 (2002)
- [90] R. T. K. Baker, and P. S. Harris, *Chemistry and Physics of Carbon*, 83 (1978)
- [91] S. J. Pearton, D. P. Norton, K. Ip, Y. W. Heo, T. Steiner, *Prog. Mater. Sci.*, 50, 293 (2005)
- [92] X. Wang, Y. Ding, C. J. Summers, Z. L. Wang, *J. Phys. Chem. B*, 108, 8772 (2004)
- [93] L. M. Kukreja, S. Barik, P. Misra, *J. Cryst. Growth*, 268, 531 (2004)
- [94] Q. H. Li, Q. Wan, Y. X. Liang, T. H. Wang, *Appl. Phys. Lett.*, 84, 4556 (2004)
- [95] Q. H. Li, Y. X. Liang, Q. Wan, T. H. Wang, *Appl. Phys. Lett.*, 85, 6389 (2004)
- [96] Y. W. Heo, L. C. Tien, D. P. Norton, B. S. Kang, F. Ren, B. P. Gila, S. J. Pearton, *Appl. Phys. Lett.*, 85, 2002 (2004)
- [97] P. Chang, Z. Fan, W. Tseng, D. Wang, W. Chiou, J. Hong, J. G. Lu, *Chem. Mater.*, 16, 5133 (2004)

- [98] W. I. Park, J. S. Kim, G.-C. Yi, M. H. Bae, H. -J. Lee, *Appl. Phys. Lett.*, 85, 5052 (2004)
- [99] Z. Fan, and J. G. Lu, *Journal of Nanoscience and Nanotechnology*, accepted (2005)
- [100] M. Joseph, H. Tabata, H. Saeki, K. Ueda, and T. Kawai, *Physica B* 302-303, 140 (2001)
- [101] D. C. Look, D. C. Reynolds, C. W. Litton, R. L. Jones, D. B. Eason, G. Cantwell, *Appl. Phys. Lett.*, 81, 1830 (2002)
- [102] C. H. Liu, W. C. Yiu, F. C. K. Au, J. X. Ding, C. S. Lee, S. T. Lee, *Appl. Phys. Lett.*, 83, 3168 (2003)
- [103] C. Klingshirn, *J. Cryst. Growth*, 117, 753 (1992)
- [104] Y. Kayamura, *Phys. Rev B*, 38, 9797 (1988)
- [105] W. Wegscheider, L. N. Pfeiffer, M. M. Dignam, A. Pinczuk, W. K. West, S. L. McCall, R. Hull, *Phys. Rev Lett.* 71, 4071 (1993)
- [106] W. I. Park, Y. H. Jun, S. W. Jung, and G. Yi, *Appl. Phys. Lett.*, 82, 964 (2003)
- [107] Y. Gu, I. L. Kuskovsky, M. Yin, S. O'Brien, and G. G. Neumark, *Appl. Phys. Lett.*, 85, 3833 (2004)
- [108] Z. Fan, P. Chang, E. C. Walter, C. Lin, H. P. Lee, R. M. Penner, and J. G. Lu, *Appl. Phys. Lett.*, 85, 6128 (2004)
- [109] I. Shalish, H. Temkin, and V. Narayanamurti, *Phys. Rev B.*, 69, 245401 (2004)
- [110] X. Wang, Y. Ding, C. J. Summers, Z. L. Wang, *J. Phys. Chem. B*, 108, 8773 (2004)
- [111] K. Keem, H. Kim, G.-T. Kim, J. S. Lee, B. Min, K. Cho, M.-Y. Sung, and S. Kim, *Appl. Phys. Lett.*, 84, 4376 (2004)
- [112] Y. Takahashi, M. Kanamori, A. Kondoh, H. Minoura, and Y. Ohya, *Jpn. J. Appl. Phys.*, Part 1 33, 6611 (1994)
- [113] P. Sharma, K. Sreenivas, and K. V. Rao, *J. Appl. Phys.*, 93, 3963 (2003)
- [114] D. H. Zhang, *J. Phys. D*, 28, 1273 (1995)
- [115] A. D. Corso, M. Posternak, R. Resta, and A. Balderschi, *Phys. Rev. B* 50, 10715 (1994)
- [116] M. H. Zhao, Z. L. Wang, and S. X. Mao, *Nano Lett.*, 4, 587 (2004)
- [117] Z. L. Wang, X. Y. Kong, Y. Ding, P. Gao, W. L. Hughes, R. Yang, and Y. Zhang, *Adv. Funct. Mater.*, 14, 943 (2004)
- [118] Y. Q. Chang, D. B. Wang, X. H. Luo, X. Y. Xu, X. H. Chen, L. Li, C. P. Chen, R. M. Wang, J. Xu, and D. P. Yu, *Appl. Phys. Lett.*, 83, 4020 (2003)
- [119] Z. Fan, D. Wang, P. Chang, W. Tseng, J. G. Lu, *Appl. Phys. Lett.*, 85, 5923 (2004)
- [120] W. I. Park, D. H. Kim, S.-W. Jung, G.-C. Yi, *Appl. Phys. Lett.*, 80, 4332 (2002)
- [121] W. Lee, M.-C. Jeong, J.-M. Myoung, *Acta Materialia*, 52, 3949 (2004)
- [122] J. Y. Park, D. J. Lee, Y. S. Yun, J. H. Moon, B.-T. Lee, S. S. Kim, *J. Cryst. Growth*, 276, 158 (2005)
- [123] M. Kawakami, A. B. Hartanto, Y. Nakata, and T. Okada. *Jpn. J. Appl. Phys.*, 42, L33 (2003)
- [124] T. Okada, B. H. Agung, and Y. Nakata, *Appl. Phys. A*, 79, 1417 (2004)
- [125] T. Okada, and K. Kawashima, *Proceedings of SPIE - The International Society for Optical Engineering*, *Fifth International Symposium on Laser Precision Microfabrication*, v 5662, 420 (2004)
- [126] R. S. Wager, W. C. Ellis, *Appl. Phys. Lett.*, 4, 89 (1964)
- [127] B. D. Yao, Y. F. Chan, and N. Wang, *Appl. Phys. Lett.*, 81, 757 (2002)

- [128] Q. Wan, K. Yu, T. H. Wang, C. L. Lin, *Appl. Phys. Lett.*, 83, 2253 (2003)
- [129] Q. H. Li, Q. Wan, Y. J. Chen, T. H. Wang, H. B. Jia and D. P. Yu, *Appl. Phys. Lett.*, 85, 636 (2004)
- [130] L. Marton, editor, “Advanced in Electronics and Electron Physics”, Vol. VIII, Academic Press INC., 1956
- [131] K. A. Dean, and B. R. Chalamala, *Appl. Phys. Lett.*, 75, 3017 (1999)
- [132] W. de Heer, A. Charelain, and D. Ugart, *Science*, 270 1179 (1995)
- [133] W. Zhu, C. Bower, O. Zhou, G. Kochanski, and S. Jin, *Appl. Phys. Lett.*, 75, 873 (1999)
- [134] J. Bonard, F. Maier, T. Stockli, A. Chatelain, W. de Heer, J. Salvetat, and L. Forro, *Ultramicroscopy*, 73, 7 (1998)
- [135] J. Bonard, J. Salvetat, T. Stockli, W. de Heer, L. Forro, and A. Chatelain, *Appl. Phys. Lett.*, 73, 918 (1998)
- [136] A. Wadhawan, R. E. Stallcup II, K. F. Stephens II, J. M. Perez, and I. A. Akwani, *Appl. Phys. Lett.*, 79, 1867 (2001)
- [137] W. B. Choi, D. S. Chung, J. H. Kang, Y. W. Jin, and I. T. Han, *Appl. Phys. Lett.*, 75, 3129 (1999)
- [138] Y. Saito, S. Uemura, and K. Hamagushi, *J. Appl. Phys.*, 37, 346 (1998)
- [139] K. L. Jensen, *Phys. Plasma*, 6, 2241 (1999)
- [140] G. Yue et al. *Appl. Phys. Lett.*, 81, 355 (2002)
- [141] W. Zhu, C. Bower, G. P. Kochanski, and S. Jin, *Solid –State Electonics*, 45, 921 (2001)
- [142] L. N. Dobretsov, and M. V. Gomoyunova, “Emission Electronics”, Israel Program for Scientific Translations, 1971
- [143] C. Liu, “Diamond and Carbon Nanotubes Coated Cold Cathodes for Vacuum Electronic Applications, dissertation, Auburn University (2004)
- [144] G. F. Zhong, T. Iwasaki, H. Kawarada, and I. Ohdomari, *thin solid films* 464, 315 (2004)
- [145] Satio Y, Hamaguchi K. Nishino T. Uuchida K. and Nishina Y., *Nature* 389, 918 (1997)
- [146] Choi W. B. *et al.*, *Appl. Phys. Lett.*, 75, 3129 (1998)
- [147] A. Wadhawan, R.E. Stallcup II, K. F. Stephen II, J. Perez, I. A. Akwani, *Appl. Phys. Lett.*, 79, 1867 (2001)
- [148] Do-Hyung Kim, Hoon-Sik Jang, Sung-Youp Lee, and Hyeong-Rag Lee, *Nanotechnology*, 15, 1433 (2004).
- [149] A. Modinos, “Field, Thermionic, and Secondary Electron Emission Spectroscopy”, Plenum Press, 1984